

**NUMERICAL STUDY OF
MAGNETOHYDRODYNAMICS AND MIXED
CONVECTION CHARACTERISTICS OF AN
ELECTRICALLY CONDUCTING FLUID**

Prithvi Ramesh

NUMERICAL STUDY OF MAGNETOHYDRODYNAMICS AND MIXED CONVECTION CHARACTERISTICS OF AN ELECTRICALLY CONDUCTING FLUID

UNDERGRADUATE THESIS

***Submitted in partial fulfilment of the requirements of
BITS F421T Thesis***

by

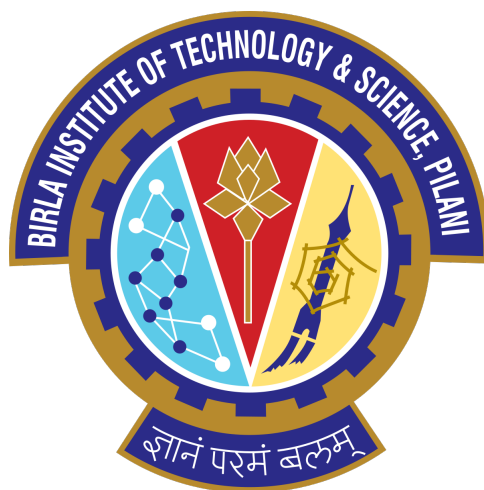
Prithvi Ramesh

ID No. 2018A4TS0502G

Under the supervision of

Dr. Manab Kumar Das

IIT Kharagpur



**Birla Institute of Technology and Science, Pilani, K.K. Birla Goa
Campus**

January 2022

January , 2022

Declaration of Authorship

I, Prithvi Ramesh, declare that this undergraduate Thesis titled "**Numerical Study of Magnetohydrodynamics and Mixed Convection Characteristics of an Electrically Conducting Fluid**" and the work presented in it are my own. I confirm that:

- This work was done wholly or mainly while in candidature for a research degree at this University.
- Where any part of this thesis has previously been submitted for a degree or any other qualification at this University or any other institution, this has been clearly stated.
- Where I have consulted the published work of others, this is always clearly attributed.
- Where I have quoted from the work of others, the source is always given. With the exception of such quotations, this thesis is entirely my own work.
- I have acknowledged all main sources of help.
- Where the thesis is based on work done by myself jointly with others, I have made clear exactly what was done by others and what I have contributed myself.

Signed:

Prithvi Ramesh

Date:12/02/2022

CERTIFICATE

This is to certify that the thesis entitled, "**Numerical Study of Magnetohydro-dynamics and Mixed Convection Characteristics of an Electrically Conducting Fluid**", submitted by **Prithvi Ramesh**, ID No. 2018A4TS0502G in partial fulfillment of the requirements of BITS F421T Thesis embodies the work done by him under my supervision.

Dr. Manab Kumar Das
Professor
Mechanical Engineering
Department
Indian Institute of Technology
Kharagpur, 721302
Signature:

Date:12/02/2022

November , 2021

ACKNOWLEDGEMENTS

I would like to thank Dr. Manab Kumar Das for his guidance, constant support and encouragement to make my thesis project a success.

Date :12/02/2022

Place : BITS-Pilani, Goa

Prithvi Ramesh

ABBREVIATIONS

- CFD : - Computational Fluid Dynamics
- OpenFOAM : - Open Source Field Operation and Manipulation
- MHD :- Magnetohydrodynamics
- PISO :- Pressure Implicit with Splitting of Operators
- RAS :- Reynolds-Averaged Navier-Stokes equation

Contents

Certificate	i
Declaration	iii
Contents	v
List of figures	viii
Nomenclature	xiii
Abstract	xiii
1 Transient Lid Driven Cavity Flow	1
1.1 Introduction	1
1.1.1 Navier-Stokes Equation	1
1.1.2 Incompressible Flow	2
1.2 Case Setup	2
1.2.1 Grid	2
1.2.2 Boundary Conditions	2
1.2.3 The PISO Algorithm	3
1.2.4 Finite Volume Method	4
1.3 Post Processing	4
1.4 Results for Two Dimensional Cavity	6
1.4.1 Reynolds Number-100	7
1.4.2 Reynolds Number-400	9
1.4.3 Reynolds Number -1000	11
1.4.4 Reynolds Number -3200	13
1.4.5 Reynolds Number-5000	15
1.4.6 Reynolds Number - 7500	17
1.4.7 Reynolds Number - 10000	19
1.5 Results for Three Dimensional Cavity	21

1.5.1	Cubic Cavity	22
1.5.1.1	Reynolds Number -400	22
1.5.1.2	Reynolds Number -1000	23
1.5.1.3	Reynolds Number -2000	24
1.5.1.4	Reynolds Number -5000	25
1.5.2	Prismatic cavity	26
1.5.2.1	Reynolds Number -100	26
1.5.2.2	Reynolds Number -400	27
1.5.2.3	Reynolds Number 1000	28
1.5.2.4	Reynolds Number -2000	29
1.5.2.5	Reynolds Number -5000	30
1.6	Total Specific Kinetic Energy	31
2	Magnetohydrodynamic effects	35
2.1	Abstract	35
2.2	Introduction	36
2.2.1	Governing Equations	36
2.2.2	Fluid Model	40
2.3	Problem Definition and Case Setup	42
2.3.1	Computational Domain and Non-dimensional Parameters .	42
2.3.2	Case Setup	43
2.4	Results and Discussion	45
2.4.1	Validation	45
2.4.2	Comparison of Newtonian and Non-Newtonian Results .	49
2.4.2.1	Streamlines	49
2.4.2.2	Velocity Plot Result	53
2.5	Conclusions	54
3	Thermal Effects	57
3.1	Introduction	57
3.1.1	Dimensionless Parameters	58
3.1.2	Governing Equations	59
3.1.2.1	Forced Convection	59
3.1.2.2	Natural Convection	59
3.2	Problem Definition and Case Setup	60
3.2.1	Forced Convection	60
3.2.1.1	Computational Domain and Boundary Conditions	60
3.2.1.2	Solver	61
3.2.2	Natural Convection	62
3.2.2.1	Computational Domain and Boundary Conditions,	62

3.2.2.2	Solver	63
3.2.3	Mixed Convection	65
3.3	Results and Discussion	66
3.3.1	Forced Convection	66
3.3.2	Natural Convection	68
3.3.3	Mixed Convection	71
4	Turbulence modelling for Magnetohydrodynamics and Mixed convection flow	77
4.1	Introduction	77
4.1.1	K-Epsilon turbulence model	77
4.1.2	Turbulent Heat Transfer	78
4.1.3	Solver	79
4.2	Case Setup	79
4.3	Validation	80
4.3.1	Fluid Flow	80
4.3.2	Turbulent Heat Transfer	82
4.3.3	Magnetohydrodynamics	85
4.4	Mathematical Formulation	86
4.4.1	Governing Equations	86
4.4.2	Boundary Conditions and Cases	87
4.5	Results	88
4.5.1	Prandtl Number = 0.71	90
4.5.1.1	Reynolds Number = 1000	90
4.5.1.2	Reynolds Number = 5000	91
4.5.1.3	Reynolds Number = 10000	92
4.5.2	Prandtl Number = 3	93
4.5.2.1	Reynolds Number = 1000	93
4.5.2.2	Reynolds Number = 5000	94
4.5.2.3	Reynolds Number = 10000	95
4.5.3	Prandtl Number = 7	96
4.5.3.1	Reynolds Number = 1000	96
4.5.3.2	Reynolds Number = 5000	97
4.5.3.3	Reynolds Number = 10000	98
4.6	Discussion	99
Bibliography		99

List of Figures

1.1	Boundary Conditions for 2D square cavity	3
1.2	Vorticity formation	4
1.3	Streamlines	8
1.4	Streamlines	10
1.5	Streamlines	12
1.6	Streamlines	14
1.7	Streamlines	16
1.8	Streamlines	18
1.9	Streamlines	20
1.10	Cube and Prism	21
1.11	Comparison of x direction velocities along centerline for Square 2D cavity and Cubic 3D cavity	22
1.12	Comparison of x direction velocities along centerline for Square 2D cavity and Cubic 3D cavity	23
1.13	Comparison of x direction velocities along centerline for Square 2D cavity and Cubic 3D cavity	24
1.14	Comparison of x direction velocities along centerline for Square 2D cavity and Cubic 3D cavity	25
1.15	Comparison of x direction velocities along centerline for Rectangular 2D cavity and Prismatic 3D cavity of aspect ratio 2 each	26
1.16	Comparison of x direction velocities along centerline for Rectangular 2D cavity and Prismatic 3D cavity of aspect ratio 2 each	27
1.17	Comparison of x direction velocities along centerline for Rectangular 2D cavity and Prismatic 3D cavity of aspect ratio 2 each	28

1.18 Comparison of x direction velocities along centerline for Rectangular 2D cavity and Prismatic 3D cavity of aspect ratio 2 each	29
1.19 Comparison of x direction velocities along centerline for Rectangular 2D cavity and Prismatic 3D cavity of aspect ratio 2 each	30
1.20 Reynolds Number=100	31
1.21 Reynolds Number=1000	32
1.22 Reynolds Number=10000	33
2.1	40
2.2 Boundary Conditions	42
2.3 Computational domain	42
2.4 Computational Grid	43
2.5 Fluid Properties	44
2.6 Values of Magnetic Field	44
2.7 Stuart Number=0	45
2.8 Stuart Number=1	45
2.9 Stuart Number =10	46
2.10 Stuart Number=50	46
2.11 Stuart Number=0	47
2.12 Stuart Number=1	47
2.13 Stuart Number =10	48
2.14 Stuart Number=50	48
2.15 Stuart number=0	49
2.16 Stuart number=1	50
2.17 Stuart number=10	51
2.18 Stuart number=50	52
2.19 Stuart Number=0	53
2.20 Stuart Number=1	53
2.21 Stuart Number=10	54
2.22 Stuart Number=50	54
3.1 Domain	60
3.2 Computational Grid	61
3.3 Boundary Conditions	61
3.4 Energy Equation	62
3.5 Domain	62
3.6 Computational Grid	63
3.7 Boundary Conditions	63
3.8 Solver Code	64
3.9 Boundary Conditions	65

3.10 Temperature Contour	66
3.11 Comparison with Santos et al(2013)	67
3.12 Rayleigh number=1e4	69
3.13 Rayleigh number=1e5	69
3.14 Rayleigh number=1e6	70
3.15 Richardson Number=0.1	72
3.16 Richardson Number=1	73
3.17 Richardson Number=5	74
3.18 Reynolds Number =100	75
3.19 Reynolds Number =400	75
3.20 Reynolds Number =1000	76
3.21 Reynolds Number =3000	76
4.1 Turbulence model constants	78
4.2 Reynolds Number =3200	81
4.3 Reynolds Number =10000	82
4.4 Comparison of U-Velocity along the vertical mid-line of the cavity .	83
4.5 Comparison of V-Velocity along the horizontal mid-line of the cavity	84
4.6 Comparison with Markatos(1984)	84
4.7 Comparison of Nusselt Number with Markatos(1984)	85
4.8 Reynolds Number=100, Hartmann Number =10	85
4.9 Reynolds Number=1000, Hartmann Number =100	86
4.10 Boundary Conditions for Velocity , Temperature and Magnetic Field	87
4.11 Variation of average Nusselt Number for Prandtl Number of 0.71 . .	88
4.12 Variation of average Nusselt Number for Prandtl Number of 3	88
4.13 Variation of average Nusselt Number for Prandtl Number of 7	89
4.14 Increment in Nusselt number with increasing Reynolds number . .	89
4.15 Decrement in Nusselt number with increasing Hartmann number .	89
4.16 Streamlines	90
4.17 U-Velocity along cavity height	90
4.18 Streamlines	91
4.19 U-Velocity along cavity height	91
4.20 Streamlines	92
4.21 U-Velocity along cavity height	92
4.22 Streamlines	93
4.23 U-Velocity along cavity height	93
4.24 Streamlines	94
4.25 U-Velocity along cavity height	94
4.26 Streamlines	95

4.27 U-Velocity along cavity height	95
4.28 Streamlines	96
4.29 U-Velocity along cavity height	96
4.30 Streamlines	97
4.31 U-Velocity along cavity height	97
4.32 Streamlines	98
4.33 U-Velocity along cavity height	98

ABSTRACT

Magnetohydrodynamics(MHD) is the study of the motion of electrically conducting fluids in the presence of an external homogeneous magnetic field. These fluids experience a force called the Lorentz force which significantly alters the velocity field. Four variations are considered with the Stuart numbers of 0,1,10 and 50. The analysis is extended to a shear-thinning and shear-thickening non-Newtonian fluids. The analysis revealed that the central core vortex is split into multiple vortices upon the application of the external magnetic field which also weakens the strength of the core vortex. The influence of the magnetic field was found to be more profound for the shear-thinning fluid and less for the shear-thickening. Three types of convective heat transfer were also investigated - forced convection , natural convection and mixed convection and the solvers created to analyse them were validated using published data. The study was extended to include turbulence for high Reynolds numbers and a steady state solver was created which combines both MHD and Mixed convection with turbulence, a validation study has been presented for the solver along with the results of the analysis for human blood. The CFD software used was Open-Source Field Operation And Manipulation (OpenFOAM).

CHAPTER 1

Transient Lid Driven Cavity Flow

1.1 Introduction

The aim of this study is to capture fluid flow phenomenon in a shear driven cavity or a lid driven cavity. Lid driven cavity is a well-known benchmark problem for viscous incompressible fluid flow. Due to its inherent simplicity in terms of geometry and boundary conditions and the availability of experimental data, the lid driven cavity has become a platform used by CFD code developers to test and validate new models as well as comparing its performance to that of existing models. The study presented in this paper focuses on the laminar, incompressible flow in a lid driven cavity using standard incompressible solvers in the OpenFOAM toolbox.

1.1.1 Navier-Stokes Equation

The Navier-Stokes equations are a set of partial differential equations developed by the Swiss Mathematician Leonhard Euler in the 18th century and further improved by the British physicist Sir George Gabriel Stokes. The first part of these equations is the mass conservation equation

Continuity equation is ,

$$\partial\rho/\partial t + \nabla\cdot(\rho V) = 0 \quad (1.1)$$

Momentum equation :

$$\rho D U_i / D t = -\partial p / \partial x_i + \partial(\mu(\partial U_i / \partial x_j)) / \partial x_j + \partial / \partial x_i [(\lambda + \mu) \partial U_k / \partial x_k] + \rho B_i \quad (1.2)$$

Total acceleration = Pressure force + Viscous force + Force due to volumetric dilation + Body Force

1.1.2 Incompressible Flow

In continuum mechanics , incompressible flow or isochoric flow is the fluid flow in which the density is held constant or varies very slightly so that it is safe to assume it to be constant. Various flow phenomenon especially those involving a dense liquid can be modeled as incompressible which simplifies the setup and decreases computational time . Another way of representing incompressible flow is by putting the divergence of the flow velocity as zero. This result is obtained from the continuity equation.

$$\nabla\cdot u = 0 \quad (1.3)$$

1.2 Case Setup

1.2.1 Grid

The Grid was generated using the blockmeshDict files due to the simplicity of the geometry . Grading factors were used to increase cell concentration near the walls where the gradients are steeper. Due to the flow being globally laminar , the $y+$ values were not a consideration in determining grid size. The 2D grid used had a 120x120 cell count

1.2.2 Boundary Conditions

The top wall in all the geometries is given a tangential velocity of 1m/s and the other walls are given no-slip condition for velocity and symmetric (Gradient zero) for pressure.

The velocity and pressure were initialized with the zero components and magnitude respectively over the grid.

Given below is an illustration of the boundary conditions used.

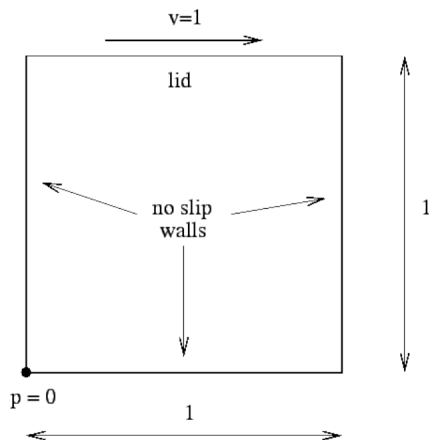


Figure 1.1: Boundary Conditions for 2D square cavity

1.2.3 The PISO Algorithm

The Pressure Implicit with Spilitting of Operators algorithm is a pressure-velocity coupled algorithm used for solving the Navier-Stokes set of equations when overall velocity and pressure profiles are unknown .The algorithm is a FVM based scheme that uses a staggered grid arrangement to avoid the formation of a 'checkerboard pressure field' which is a zigzag pressure filed , interpreted by the algorithm a uniform pressure field.

1. An initial pressure field initialised by the user is taken as the guessed pressure field (p^*) .
2. The momentum equation is then solved using this pressure field and the guessed velocities(U^*) at the cell faces (centre points of staggered grid) are obtained.
3. The corrected velocities designated as $U=U^*+U'$ are substituted into the continuity equations and a set of algebraic equations involving the velocity corrections are modified to include the pressure corrections (each velocity correction U' is expressed as a linear combination of the two adjutant cell centre's pressure corrections - p')
4. A corrected pressure field $p^{**} = p^* + p'$ is used to obtain a corrected velocity field as U^{**} through the momentum equations , these are then the new guessed velocity an pressure fields and the next set of corrections (U'' and p'') are obtained from the continuity equation . The sequence is looped till the corrections diminish below a threshold.

4 Post Processing

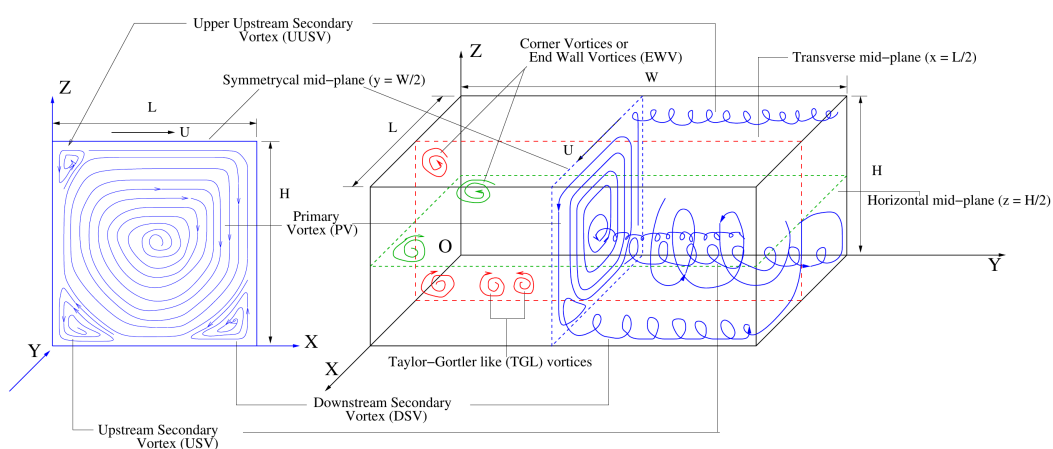
The PISO algorithm has an internal loop (unlike SIMPLE algorithm that uses an external loop) and due the fact that both the momentum and continuity equations are involved in every iteration , the velocity and pressure fields obtained at the end of each external loop are genuine . Due to this feature the PISO algorithm is highly suited for Transient flows.

1.2.4 Finite Volume Method

The domain is divided into a number of non-overlapping control volumes such that there is one control volume surrounding each grid point. The differential equations are integrated over each control volume . Piece-wise linear profiles for the dependent variables within a control volume are used to evaluate the required integrals. The advantage of the control volume formulation is that the resulting solution assures integral conservation of quantities such as mass, momentum and energy over the entire domain. The method can also easily be formulated for unstructured meshes since no assumption regarding the shapes of control volumes is made .OpenFOAM uses a cell-centroid approach for the solution like many other commercial CFD packages. The finite volume method is contrasted with finite difference method which only works for a grid with all nodes lying on two or three perpendicular axis like the 'x,y,z' coordinate system and extensive conversions are required for grids points that deviate from these axis , the finite volume method on the other hand does not require any conversions as such and can easily be applied for complex geometries .

1.3 Post Processing

Figure 1.2: Vorticity formation



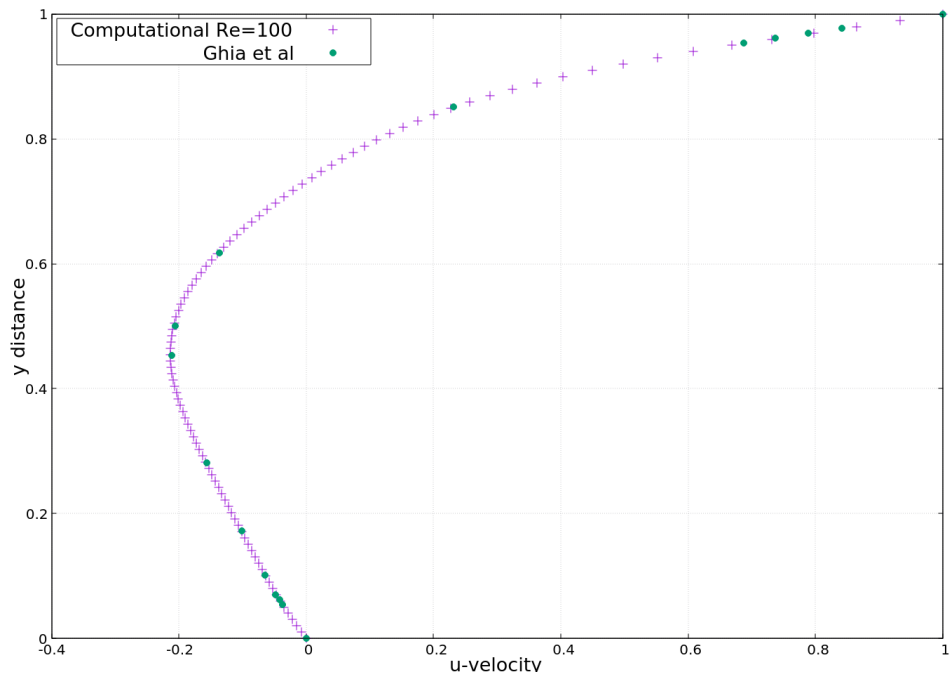
The results obtained are displayed in the form of streamlines, contours, and plots. The data was compared with the . The standard post-processing tool available with OpenFOAM - the paraView was used to obtain the streamlines and contours . To obtain the plots the foamGet command was used in conjunction with the singleGraph . Two separate start and end points were given , the first one was the horizontal line stretching through the geometric center , and the second was a vertical case again passing through the geometric center. For the vertical line y-component or 'v' of the velocity was used , and for the horizontal line the x-component or the 'u' velocity was used. Based on the results obtained in the singleGraph.

1.4 Results for Two Dimensional Cavity

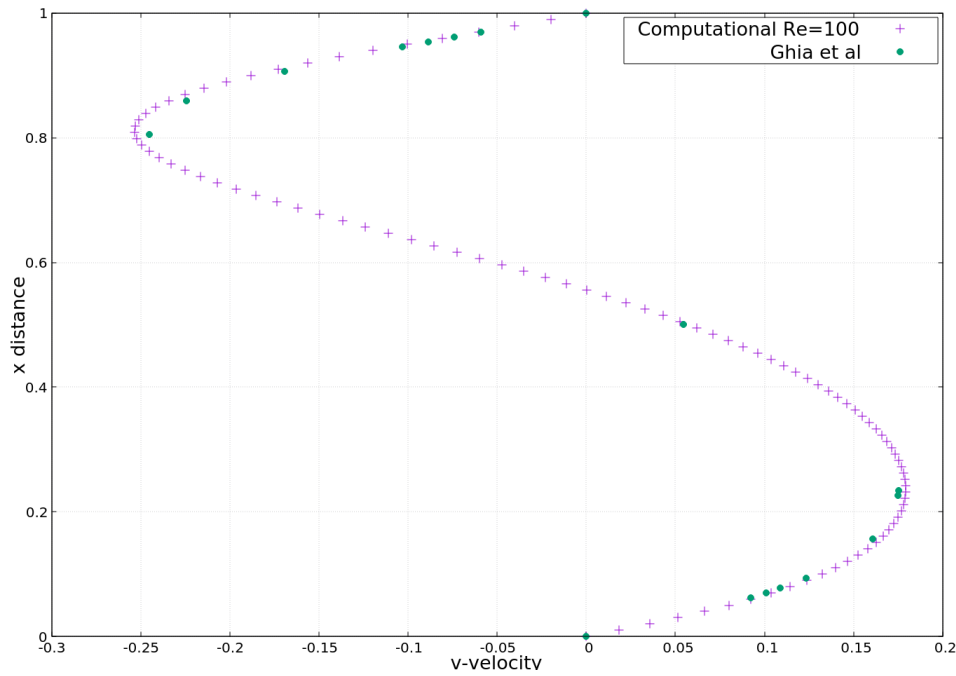
The results of the simulations which were run with a time step of 0.005 seconds are compared with the published data of Ghia et al(1982)[8] . The first three cases had a end time of 270 seconds to reach reach convergence. The Reynolds numbers of 3200 up to 7500 were run for 500 seconds and for Reynolds number of 10000- convergence was observed after 4000 seconds

1.4.1 Reynolds Number-100

Being a lower Reynolds number case very little or no formation of eddies was observed. Due to relatively higher viscosity the momentum diffusivity of the flow is larger and the lid velocity (of magnitude 1) is seen to be penetrating deeper into the domain . This penetration reduces for high Reynolds number cases.



(a) Comparison of u-velocity along cavity height



(b) Comparison of v-velocity along cavity length

8 Results for Two Dimensional Cavity

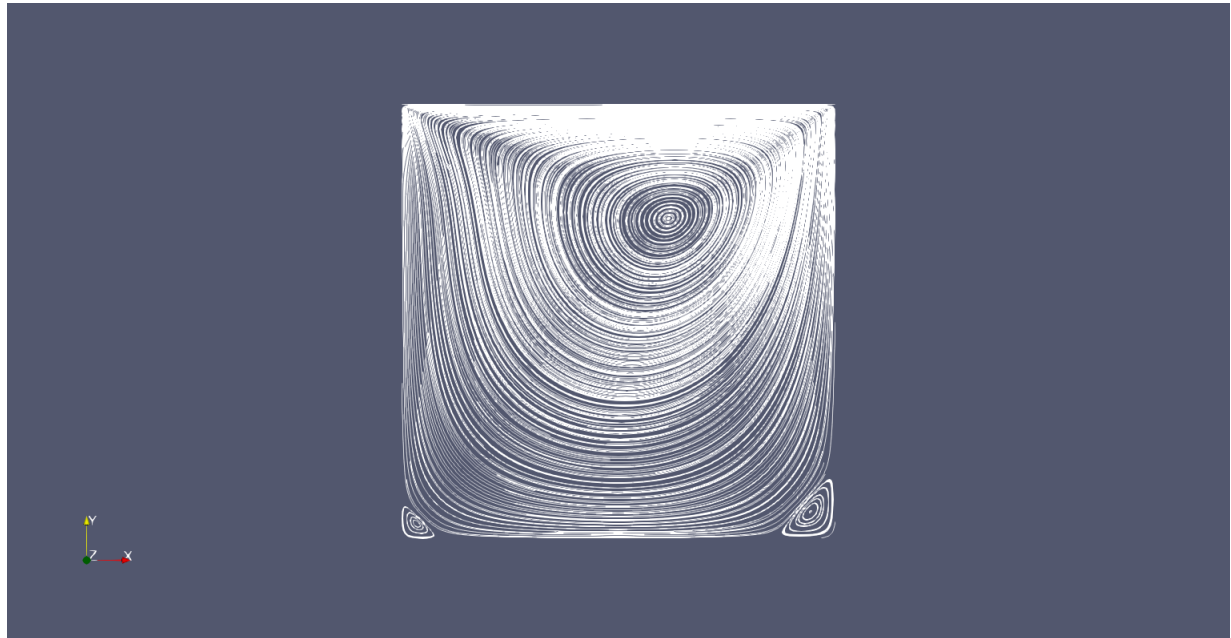
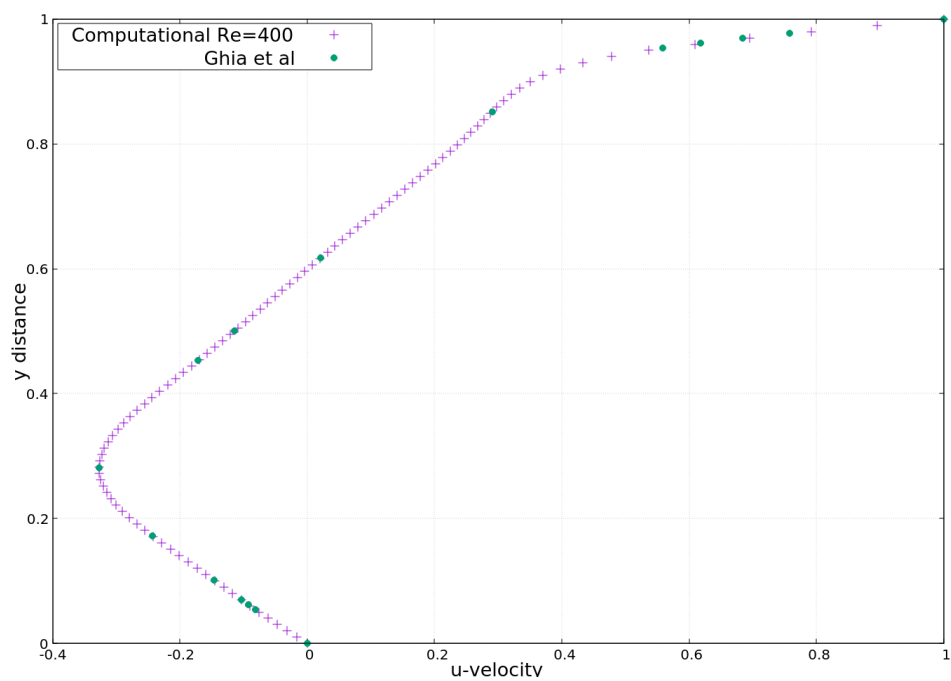


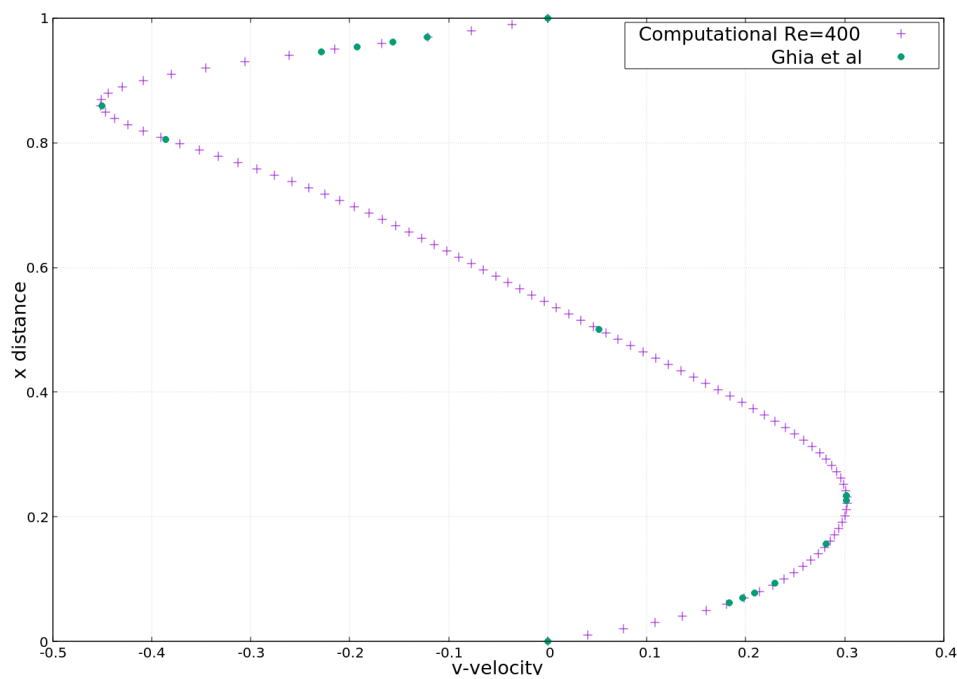
Figure 1.3: Streamlines

1.4.2 Reynolds Number-400

No eddy formation was observed . Larger velocities were observed near the center of the geometry.



(a) Comparison of u-velocity along cavity height



(b) Comparison of v-velocity along cavity length

10 Results for Two Dimensional Cavity

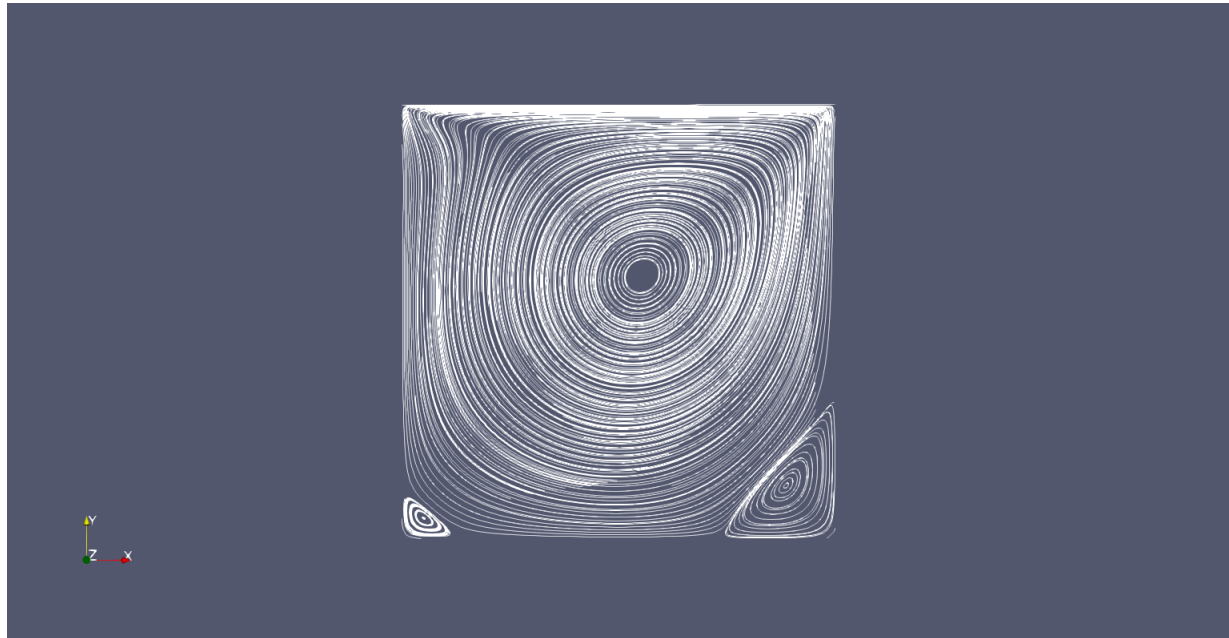
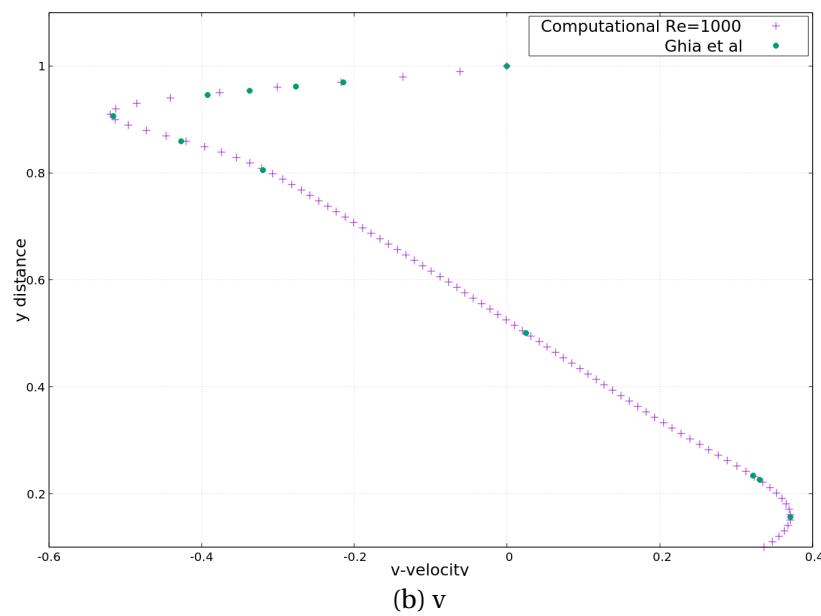
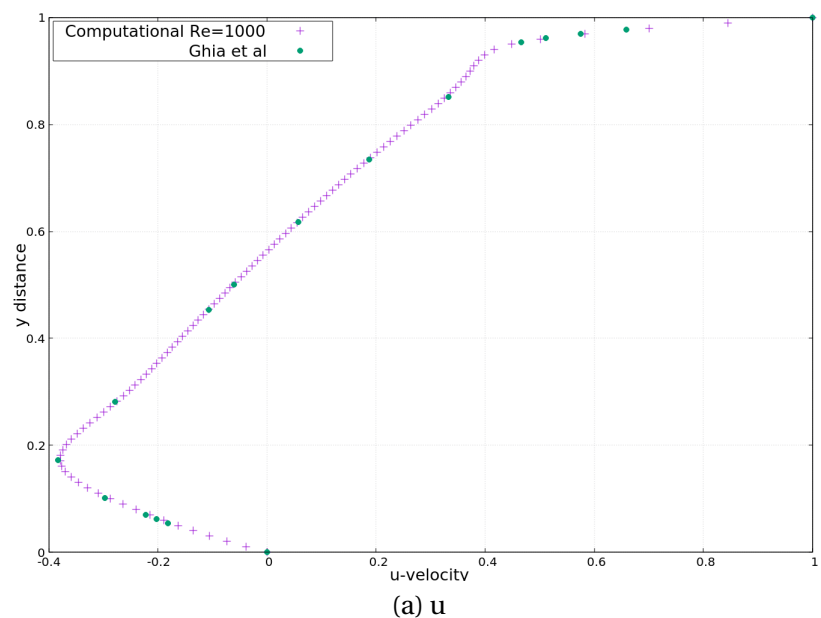


Figure 1.4: Streamlines

1.4.3 Reynolds Number -1000

Eddy formation was observed at the lower left and right corners.



12 Results for Two Dimensional Cavity

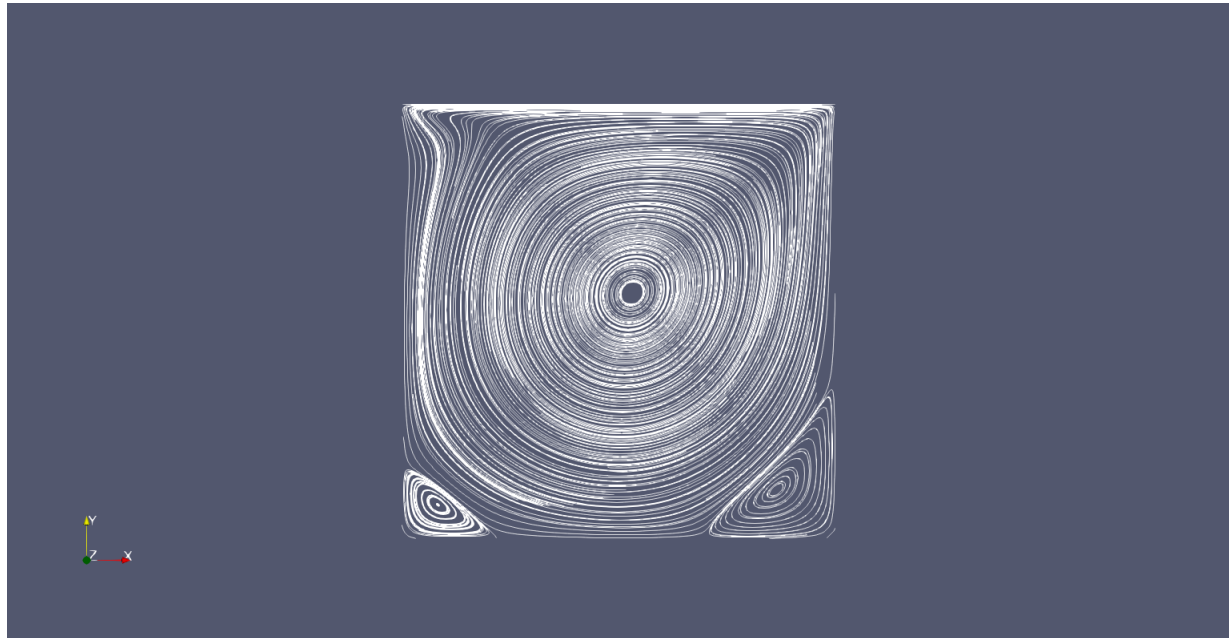
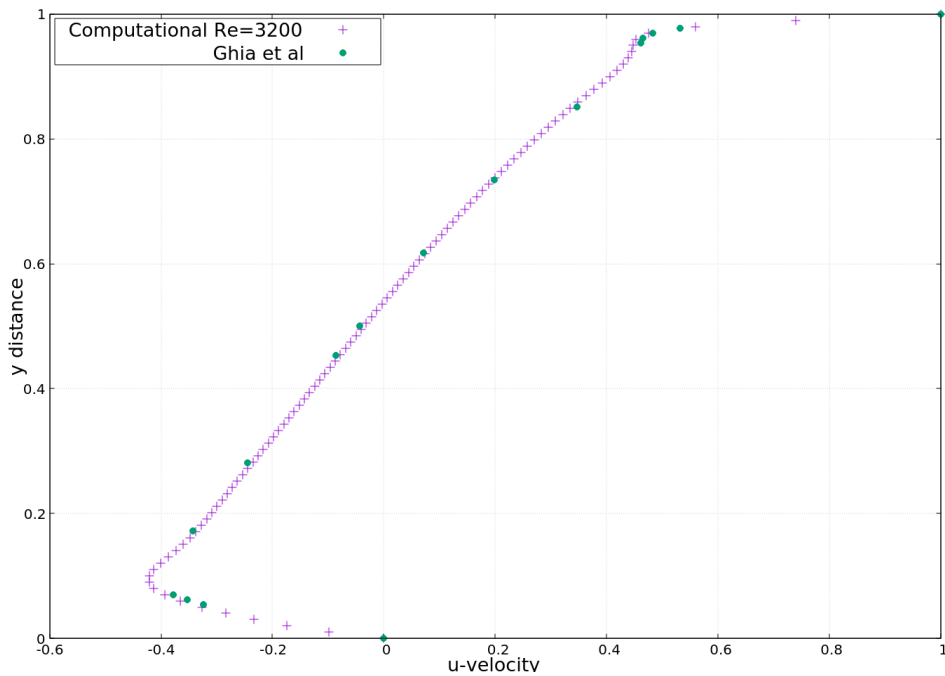


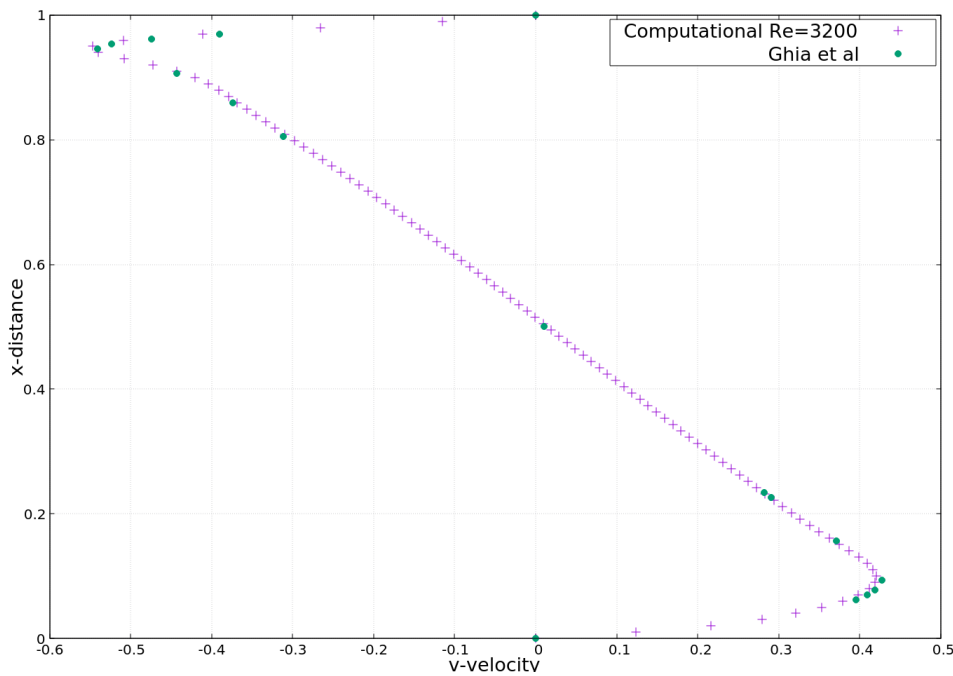
Figure 1.5: Streamlines

1.4.4 Reynolds Number -3200

Due to the increase in Reynolds number and the subsequent reduction in the dynamic viscosity the contribution of the convective term is more than the diffusion term in the Navier-Stokes equation . This results in longer time needed for the boundary information to reach the center of the domain. Significant eddy formation was observed on the lower left and right corners and the top left corner of the domain.



(a) Comparison of u-velocity along cavity height



(b) Comparison of v-velocity along cavity length

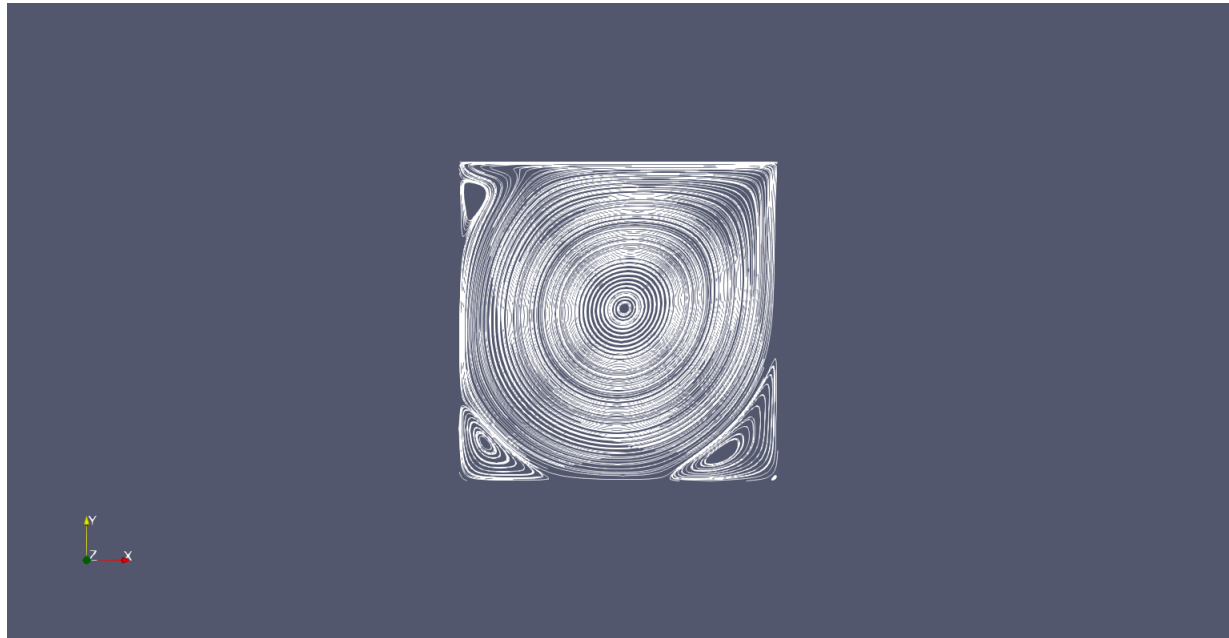
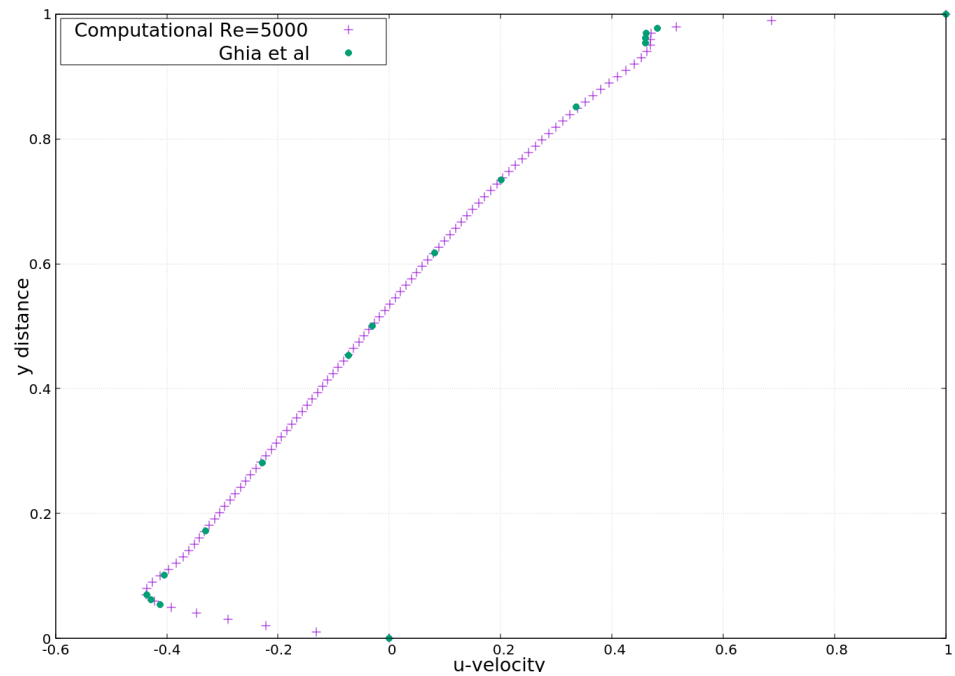


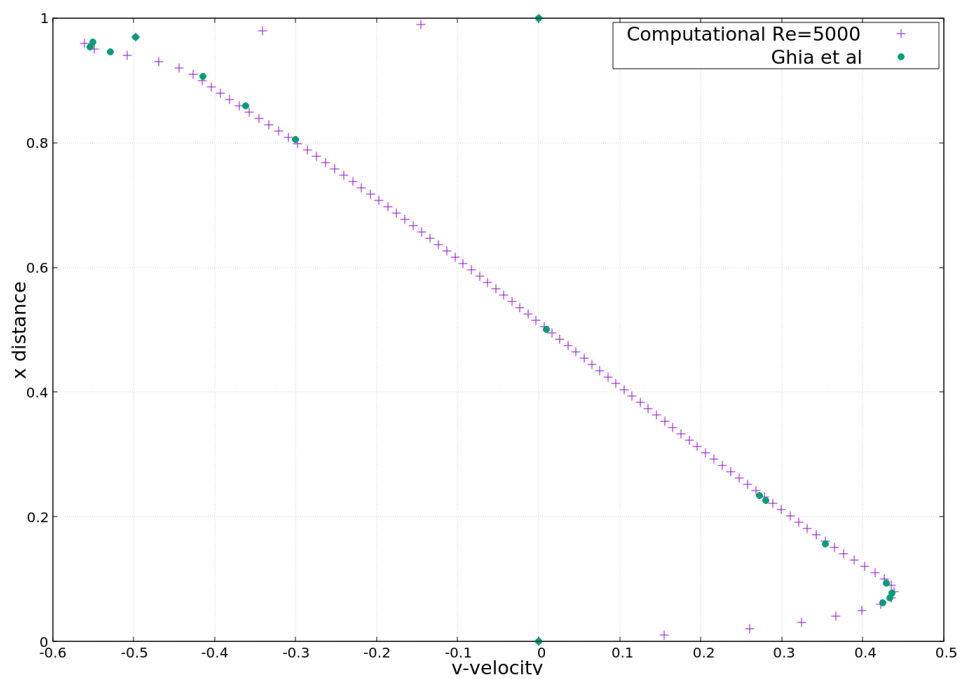
Figure 1.6: Streamlines

1.4.5 Reynolds Number-5000

Eddy formation was observed on the top , left and right corners of the domain. Results obtained are in close agreement with Ghia et al(1982) [8], however deviation are being observed close to the upper shearing lid , due to the steep velocity gradients.



(a) Comparison of u-velocity along cavity height



(b) Comparison of v-velocity along cavity length

16 Results for Two Dimensional Cavity

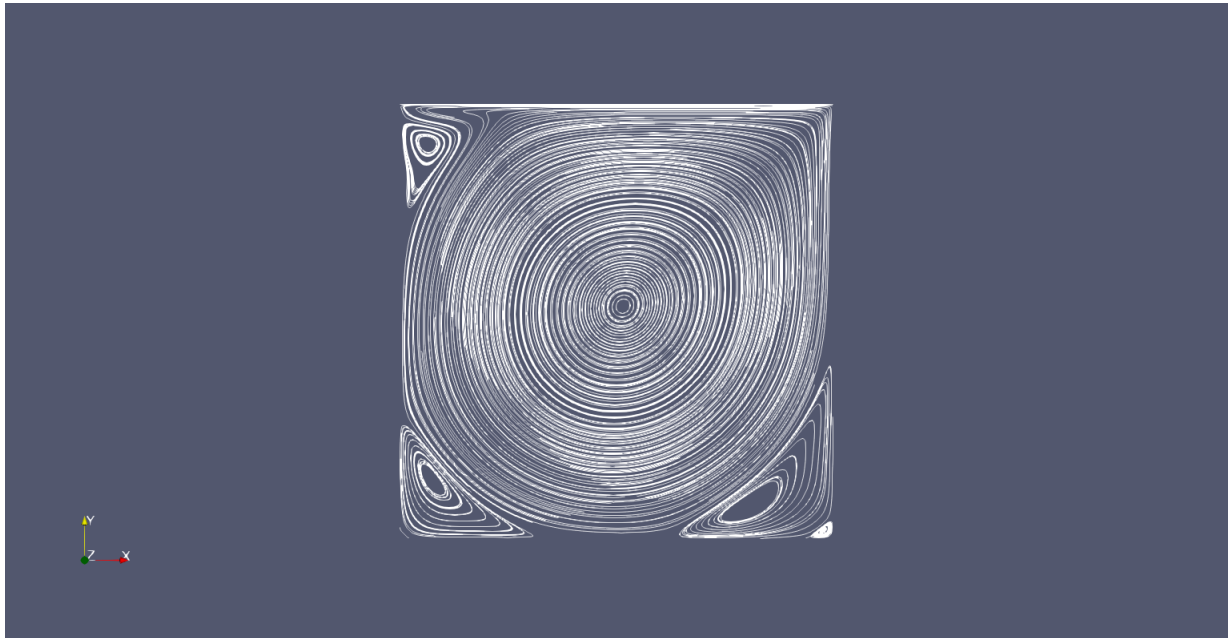
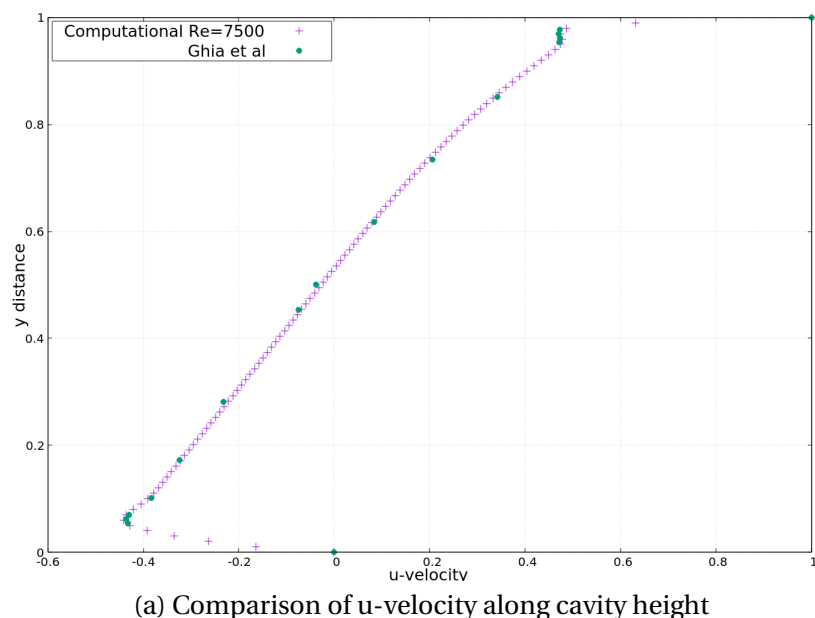


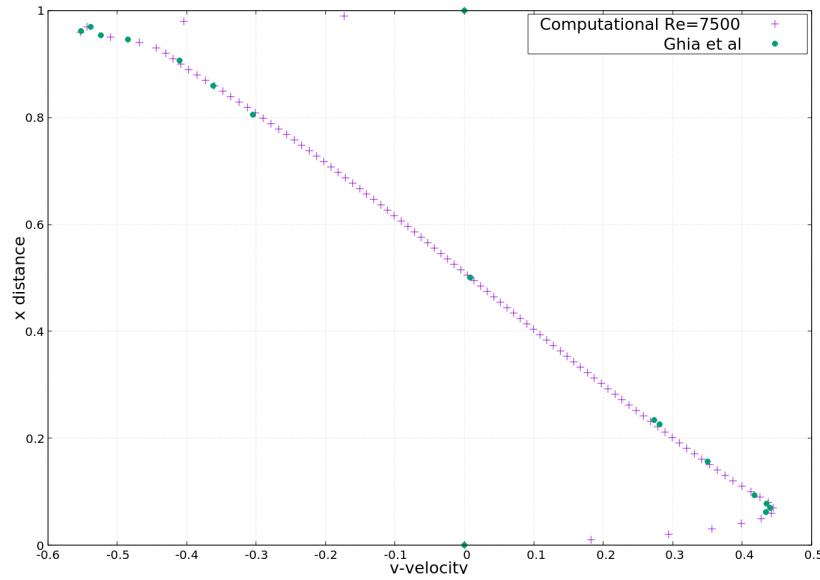
Figure 1.7: Streamlines

1.4.6 Reynolds Number - 7500

Eddy formation was observed in the top , left and right corners. The results are in close agreement with Ghia et al(1982) [8],however slight deviations are being observed near the top moving wall.



(a) Comparison of u-velocity along cavity height



(b) Comparison of v-velocity along cavity length

18 Results for Two Dimensional Cavity

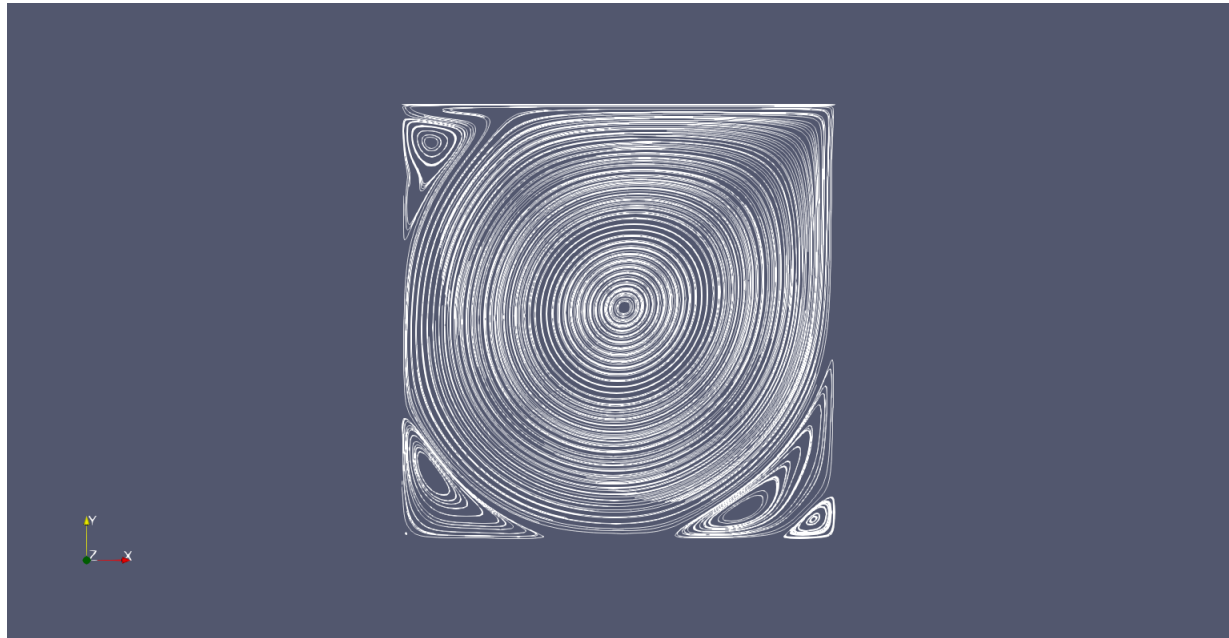
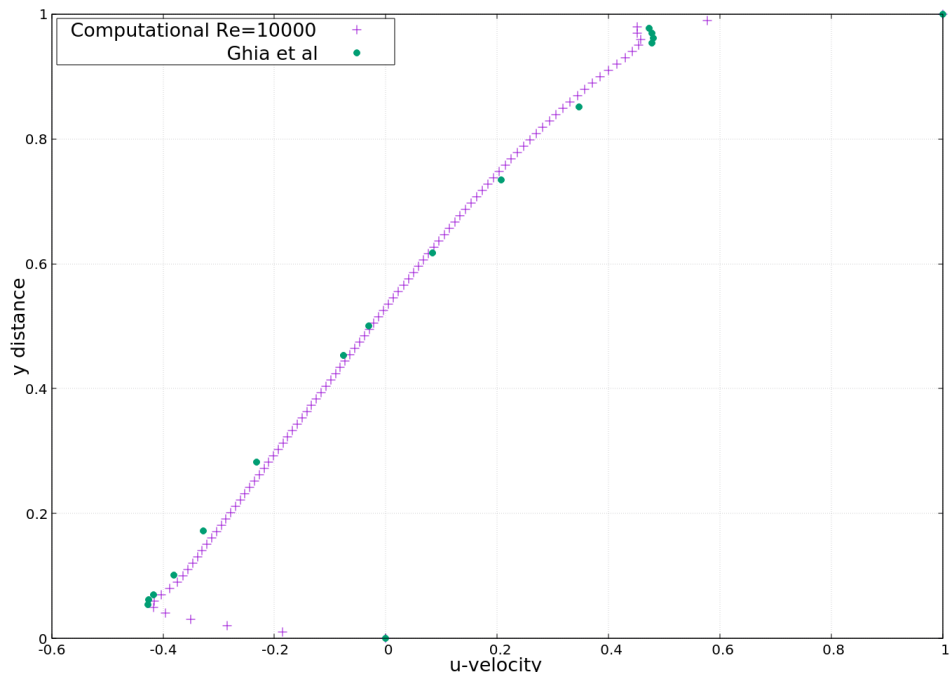


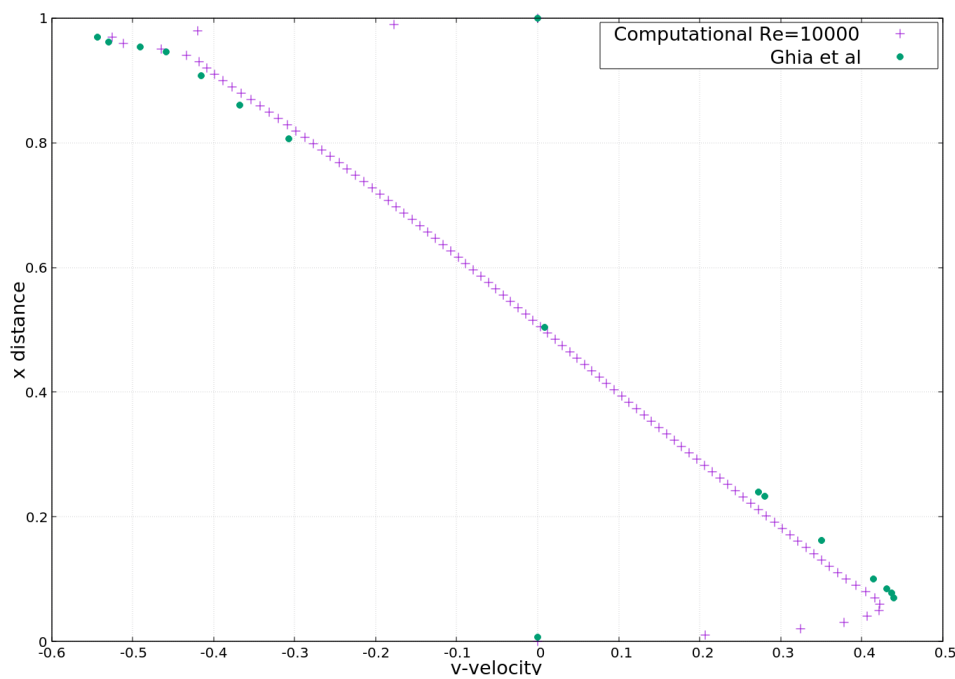
Figure 1.8: Streamlines

1.4.7 Reynolds Number - 10000

The reduced viscosity resulted in significantly longer time taken for the boundary information to reach the center. Due to this reason , the final result displays higher deviation from the published results than the lower Reynolds number cases .



(a) Comparison of u-velocity along cavity height



(b) Comparison of v-velocity along cavity length

20 Results for Two Dimensional Cavity



Figure 1.9: Streamlines

1.5 Results for Three Dimensional Cavity

The cubic cavity is a 3-Dimensional analogue of the square problem . The solution for the 3D cubic and prismatic cavities are computationally expensive and therefore a $20 \times 20 \times 20$ grid is used . A mesh dependence test was preformed and the grid was found to be satisfactory .The grid is also stretched to allow for higher resolution near the walls(Faces) where the velocity gradients are large .Steady state condition was obtained till a a Reynolds number of 2000. The boundary conditions are similar to the square cavity . Three components of the velocity are set zero on all faces with the exception of the top face where the x-component was set to 1. The graphs generated are compared with Cortes and Miler (1994) [3]

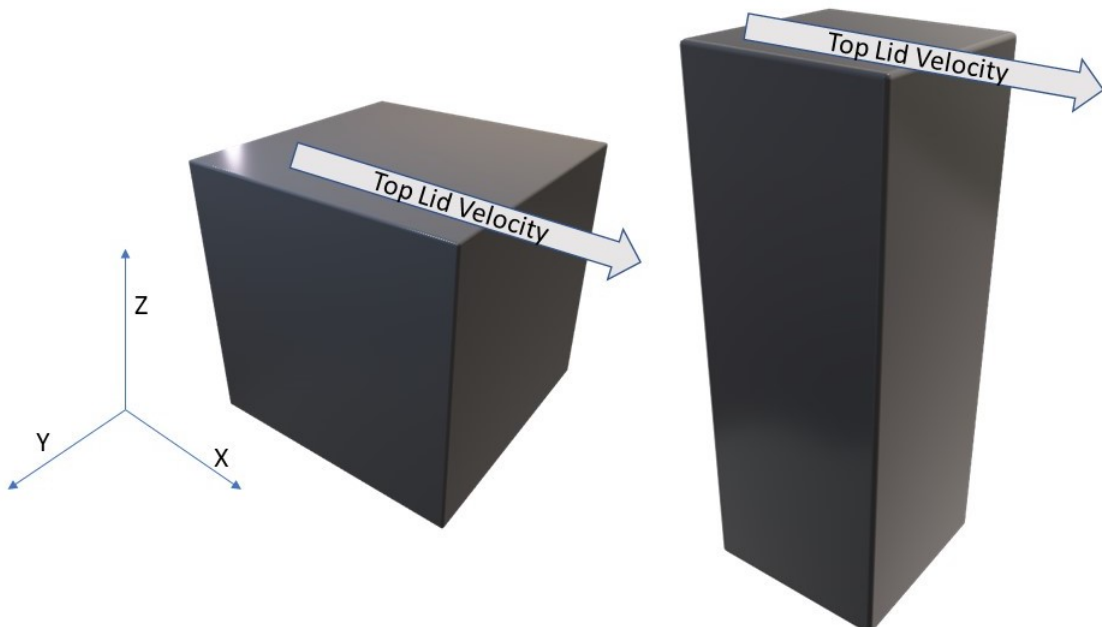


Figure 1.10: Cube and Prism

A comparison of the results for similar Reynolds numbers has been drawn between the 2d and 3D results using the centreline velocities.

1.5.1 Cubic Cavity

1.5.1.1 Reynolds Number -400

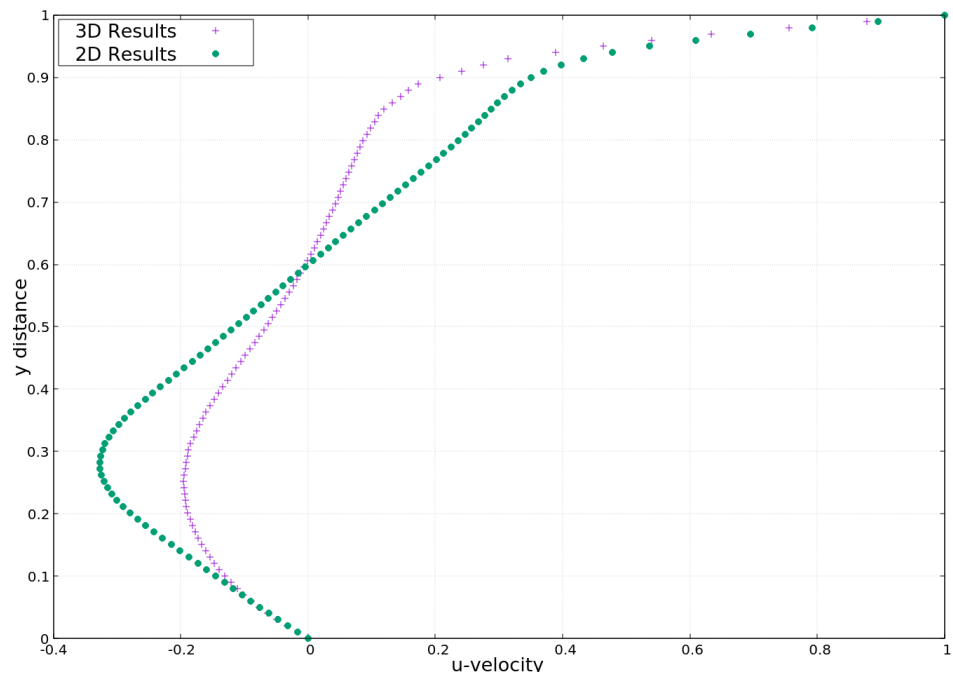


Figure 1.11: Comparison of x direction velocities along centerline for Square 2D cavity and Cubic 3D cavity

1.5.1.2 Reynolds Number -1000

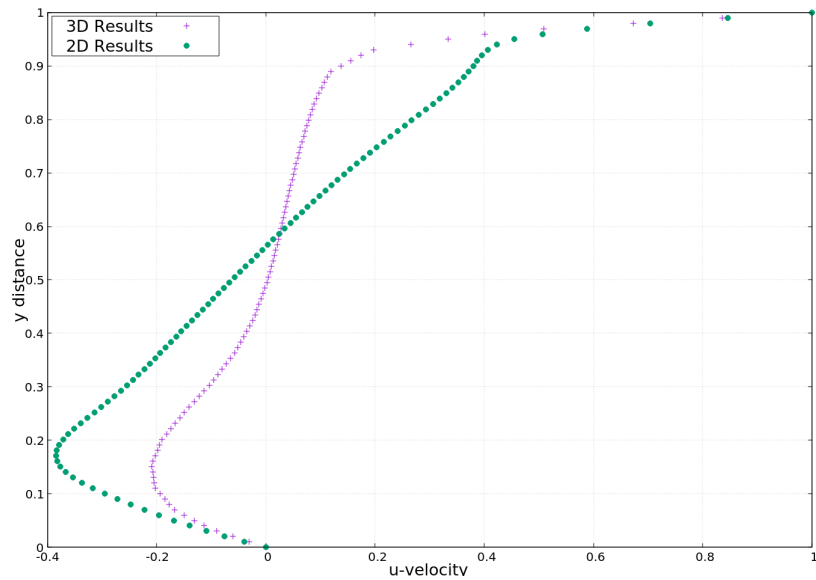


Figure 1.12: Comparison of x direction velocities along centerline for Square 2D cavity and Cubic 3D cavity

1.5.1.3 Reynolds Number -2000

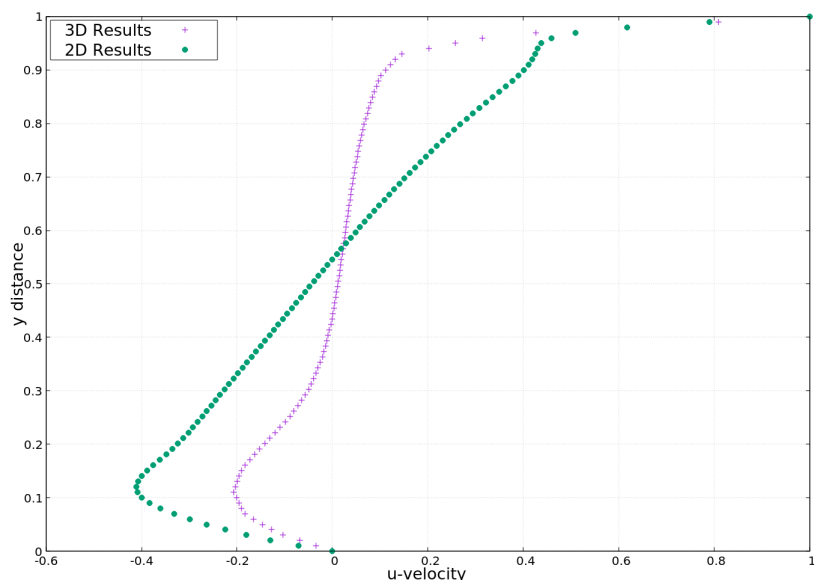


Figure 1.13: Comparison of x direction velocities along centerline for Square 2D cavity and Cubic 3D cavity

1.5.1.4 Reynolds Number -5000

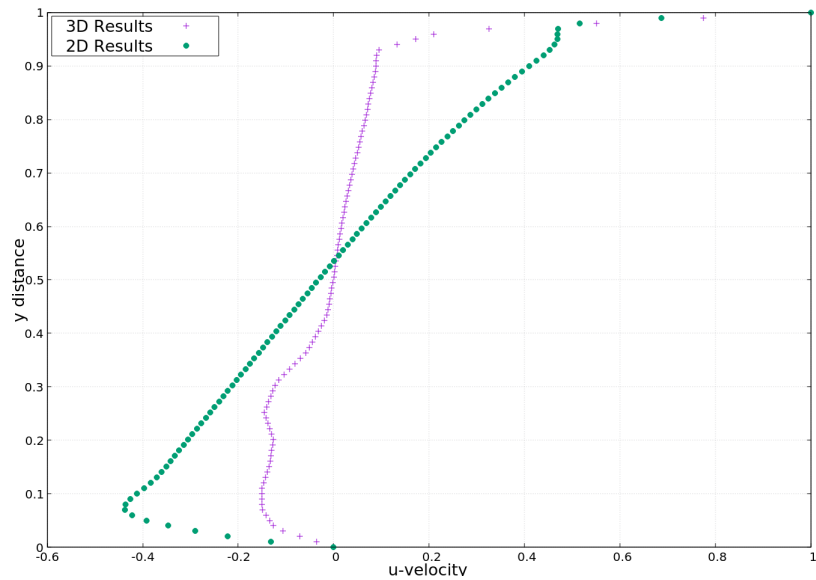


Figure 1.14: Comparison of x direction velocities along centerline for Square 2D cavity and Cubic 3D cavity

1.5.2 Prismatic cavity

1.5.2.1 Reynolds Number -100

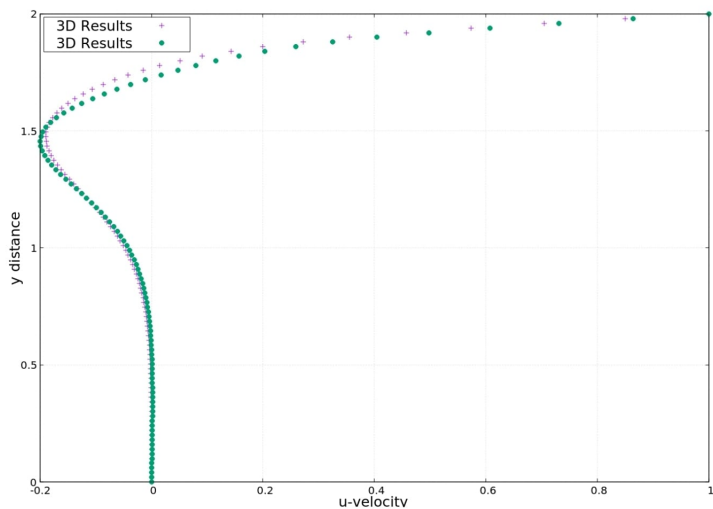


Figure 1.15: Comparison of x direction velocities along centerline for Rectangular 2D cavity and Prismatic 3D cavity of aspect ratio 2 each

1.5.2.2 Reynolds Number -400

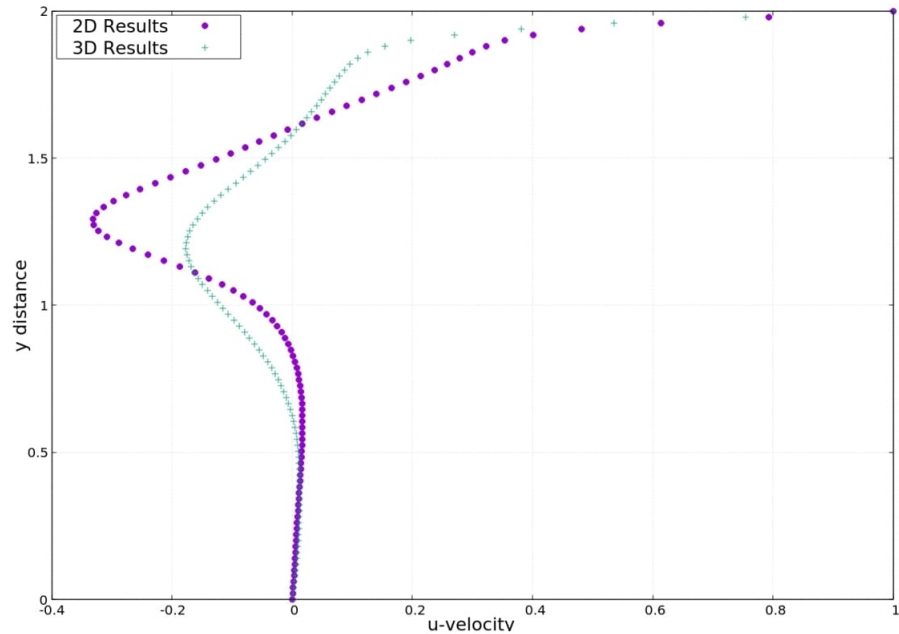


Figure 1.16: Comparison of x direction velocities along centerline for Rectangular 2D cavity and Prismatic 3D cavity of aspect ratio 2 each

1.5.2.3 Reynolds Number 1000

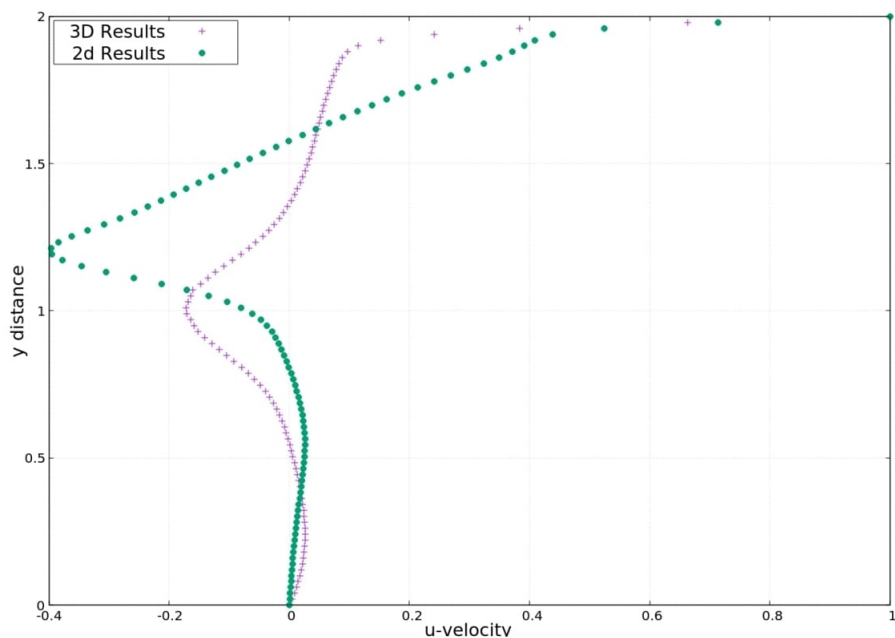


Figure 1.17: Comparison of x direction velocities along centerline for Rectangular 2D cavity and Prismatic 3D cavity of aspect ratio 2 each

1.5.2.4 Reynolds Number -2000

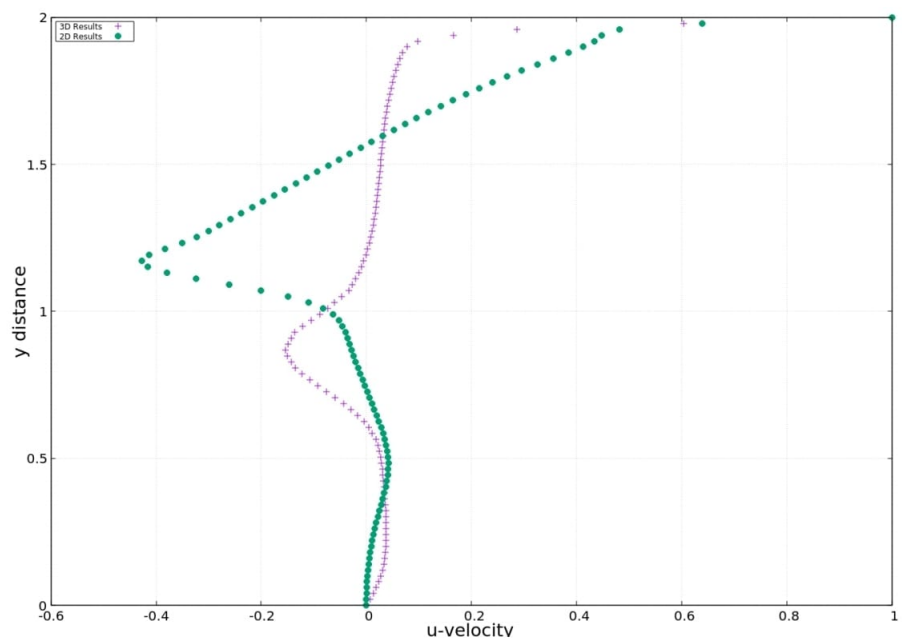


Figure 1.18: Comparison of x direction velocities along centerline for Rectangular 2D cavity and Prismatic 3D cavity of aspect ratio 2 each

1.5.2.5 Reynolds Number -5000

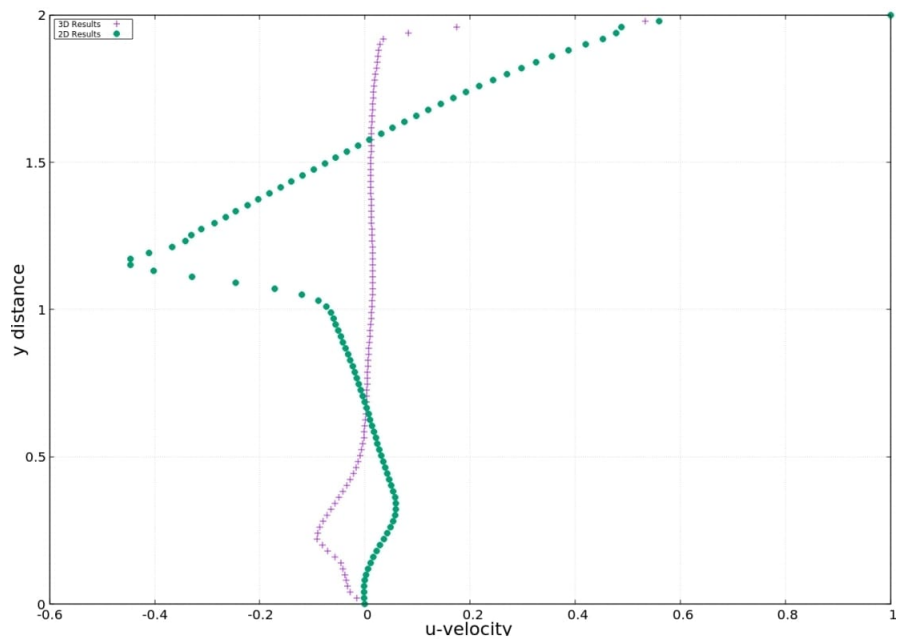


Figure 1.19: Comparison of x direction velocities along centerline for Rectangular 2D cavity and Prismatic 3D cavity of aspect ratio 2 each

1.6 Total Specific Kinetic Energy

The quality is obtained as the summation of the square of the velocity magnitude multiplied half and summed over all the cells included in the computational domain. The simulations are done for a 2-D rectangular cavity with aspect ratio as 2.

$$TKE = 0.5 * |U| * |U|$$

The values obtain are only taken for a relativistic comparison of the velocity patterns and the effect of viscosity on them and are not reflective of the true kinetic energy possessed by the fluids since the mass term is excluded.

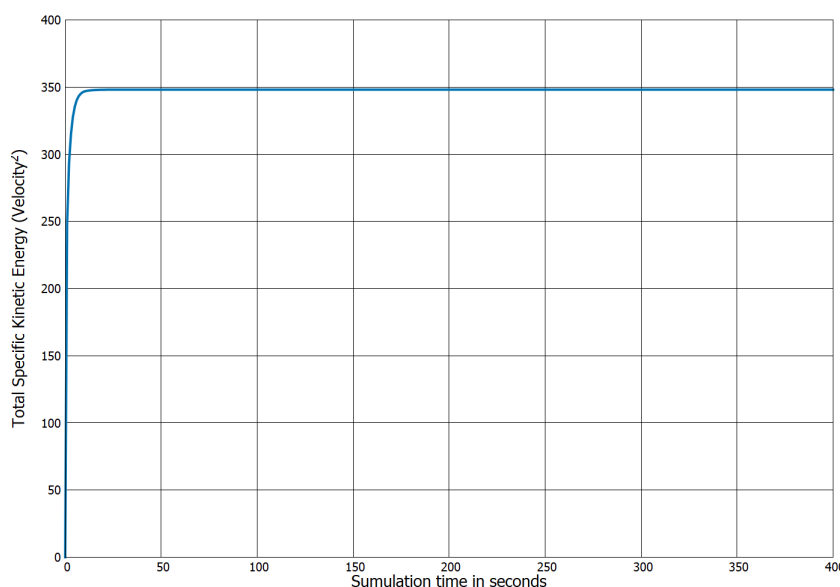


Figure 1.20: Reynolds Number=100

32 Total Specific Kinetic Energy

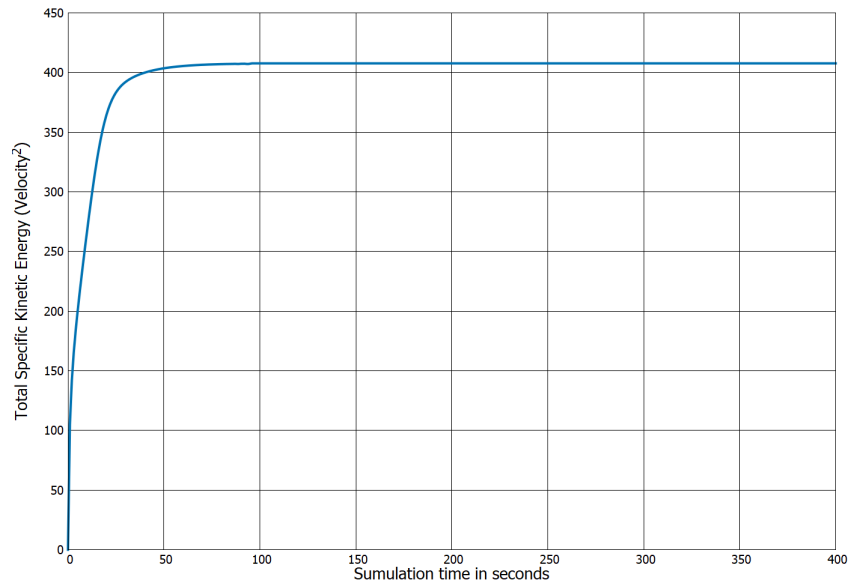


Figure 1.21: Reynolds Number=1000

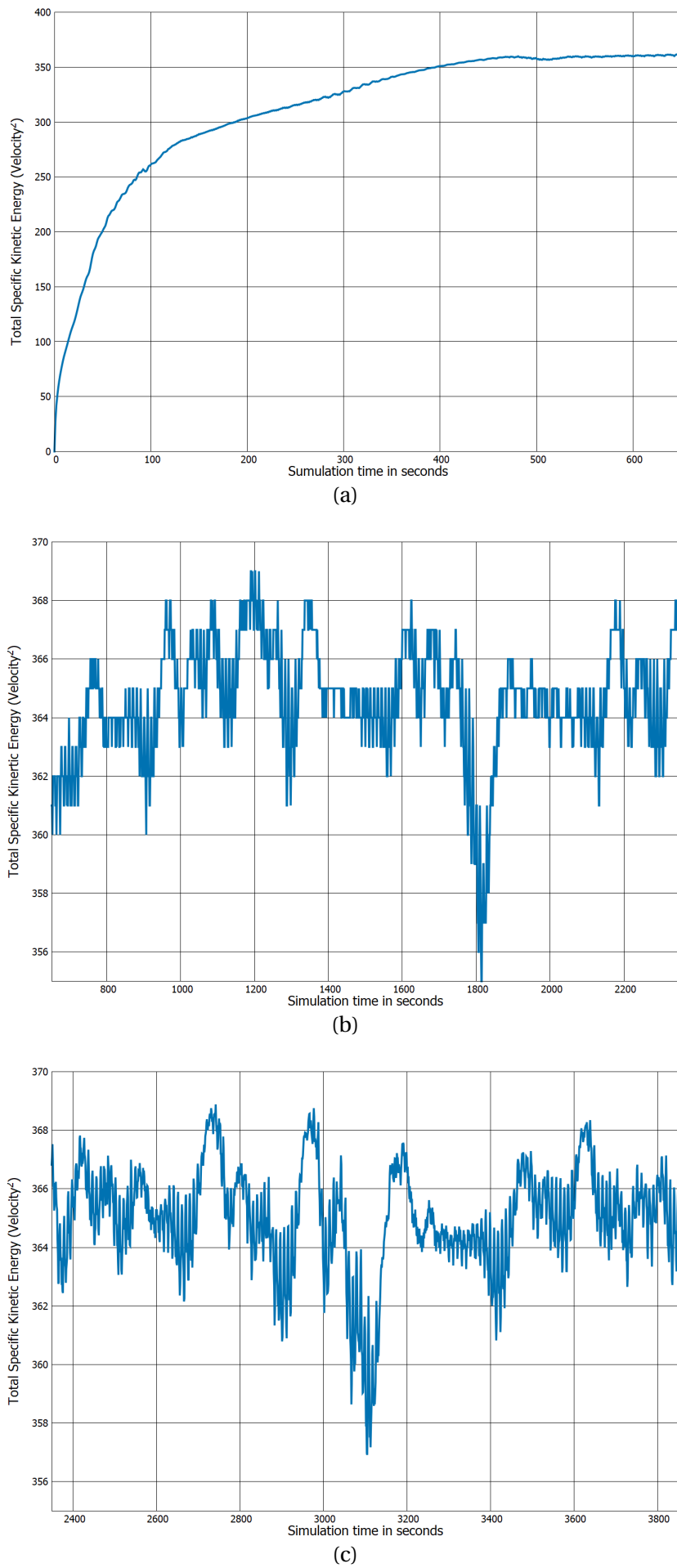


Figure 1.22: Reynolds Number=10000

The analysis of the Total Specific Kinetic Energy indicates that the velocity values stabilize relatively early for lower Reynolds number. For higher Reynolds number, the velocity values stabilization takes longer since the boundary information takes longer to reach the cavity center due to the reduced viscosity, further the high Reynolds number case has the velocity values fluctuating continuously.

CHAPTER 2

Magnetohydrodynamic effects

2.1 Abstract

Electrically conducting fluids experience a force when an external magnetic field is applied on them. This external force is modeled using Maxwell's equations of electrostatics and is included as a body force in the Naiver-Stokes equations. The effect of the force on fluids is investigated for four different Stuart's numbers namely -0, 5, 10, 50 with the Reynolds number kept constant at 100. Non-Newtonian fluids do not follow the Newton's law of linear variance of stress to the rate of shear strain, the viscosity of these fluids depends on the force applied, while for Newtonian fluids the viscosity remains constant. The Power-law scheme is used to model the Non-Newtonian behavior with the power-law coefficient taken as 0.6 , 1.2(for non-newtonian) and 1(for Newtonian). The case is setup for a lid-driven cavity, in which the flow is driven by the upper wall. The walls are assumed to be perfectly non-conducting. The standard OpenFOAM solver- mhdfoam is modified to model the viscosity with the power-law scheme. This study finds applications in healthcare and metallurgical industries. Since blood flow in an Magnetic Resonance Imaging(MRI) instrument is modeled as a Non-Newtonian MHD fluid under the influence of an external magnetic field. The validation is done using the results published in Kefayati (2014). It has been inferred that the deviation of Non-Newtonian from Newtonian behavior is increased with increase in Stuart Number. Furthermore the external magnetic field lines split the fluid flow into two or more vortices as the Stuart Number increases.

2.2 Introduction

2.2.1 Governing Equations

A moving stream of an electrically under the influence of an externally imposed magnetic field experiences Lorentz force. These Lorentz forces oppose the motion of the fluid in a direction perpendicular to the field lines. The currents themselves induced a secondary field which according to Faraday's law oppose the external field. Therefore the sum of the external field (B_o) and the induced field (b) is the total magnetic field.

$$B_o = B + b \quad (2.1)$$

The four Maxwell's equations used in conjunction with Naiver-Stokes equations are:

1. Gauss's law of Electrostatics

The divergence of the electric field developed depends on the charge density ρ_c and the permittivity of free space ϵ_0

$$\nabla \cdot E = \frac{\rho_c}{\epsilon_0} \quad (2.2)$$

2. Gauss's law of Magnetism

Gauss's law of magnetism dictates that magnetic field lines behave like streamlines of incompressible fluids- there cannot be an isolated North or South poles. B - magnetic field

$$\nabla \cdot B = 0 \quad (2.3)$$

3. Faraday's Law

Time change in mangetic fields can create electric fields.

$$\nabla \times E = -\frac{\partial B}{\partial t} \quad (2.4)$$

4. Amphere-Maxwell's Law

Time change in electric fields can create an induced magnetic field. μ_0 - magnetic permitivity of free space , c - speed of light

$$\nabla \times B = \mu_0 J + \frac{1}{c^2} \frac{\partial E}{\partial t} \quad (2.5)$$

The Lorentz force which combines the effect of electric and magnetic fields for a fluid particle is given as:

$$F = q \vec{E} + q(\vec{V} \times \vec{B}) \quad (2.6)$$

The same equation is expressed in the volumetric form based on the continuum hypothesis (dividing by a infinitesimal volume)

$$f = \rho_c \vec{E} + \rho_c (\vec{V} \times \vec{B})$$

The velocity component in the above equation is combined with charge density to form the current density- \vec{J}

$$f = \rho_c \vec{E} + (\vec{J} \times \vec{B}) \quad (2.7)$$

The following assumptions are involved in the Ideal MHD formulation-

1. The effect of the electric fields are negligible
2. The induced magnetic field has a negligible effect
3. The fluid velocity and the charge velocity are the same- allowing for the coupling of the Naiver-Stokes and Maxwell's equations

By neglecting electric field, (Eq. 2.6) becomes,

$$f = J \times B \quad (2.8)$$

The coupled Naiver-Stokes (Eq.1.2) and Maxwell's equations(Eq. 2.2) with the Lorentz force added as a body force is given as:

$$\rho(D\vec{V}/Dt) = -\nabla p + \mu\nabla^2\vec{V} + \vec{J} \times \vec{B} \quad (2.9)$$

since, the magnetic field lines \vec{B} can be written as (Ampere-Maxwell Law (Eq.2.5))
:

$$\nabla \times \vec{B} = \mu_o \vec{J} \quad (2.10)$$

Using vector identity,

$$\nabla \times F \times G = F(\nabla.G) - G(\nabla.F) + (G.\nabla)F - (F.\nabla)G \quad (2.11)$$

The coupled Naiver-Stokes and Maxwell's equation is :

$$\rho(D\vec{V}/Dt) = -\nabla p + \mu\nabla^2\vec{V} + ((\vec{B}.\nabla)\vec{B}/\mu_o) - (\nabla B^2/(2 * \mu_o)) \quad (2.12)$$

where,

$((\vec{B}.\nabla)\vec{B}/\mu_o)$ -Magnetic pressure (scalar)

$\nabla B^2/(2 * \mu_o)$ -Magnetic Tension (in the fluid flow direction)

The magnetic field lines - \vec{B} can be visualized as the velocity field \vec{V} , therefore the \vec{B} can be treated as an additional variable like the velocity to be solved for. Further a transport equation called the induction equation and a corrector equation are required to close the set of equations.

The current density is given as (By Ohm's Law):

$$j = \sigma E^* \quad (2.13)$$

where E^* is the electric field in a frame of reference fixed to the material. If the conductor moves with a velocity v ,

$$E^* = E + v \times B \quad (2.14)$$

The current density in a moving conductor is given by Ohm's law

$$j = \sigma E^* = \sigma (E + v \times B) \quad (2.15)$$

- Apply curl operator on Ohm's law for moving fluids (Eq. 2.20)
- Substitute the electric field (Eq.) and the current density (Eq. 2.5)
- B is solenoidal i.e. $\nabla \cdot B = 0$ (Eq. 2.3)
- Flow is incompressible i.e. $\nabla \cdot V = 0$ (Eq. 1.3)
- Vector analytical rearrangement

Magnetic Transport Equation-

$$\partial \vec{B} / \partial t = \eta \nabla^2 \vec{B} + \nabla \times (\vec{V} \times \vec{B}) \quad (2.16)$$

Magnetic Continuity Equation-

$$\nabla \cdot \vec{B} = 0 \quad (2.17)$$

The velocity needs to be known for these equations to be solved, therefore a second algorithm called the 'BPISO' algorithm is used to solve for B after the velocity is known from the PISO algorithm

The four governing equations are:

$$\rho(D\vec{V}/Dt) = -\nabla p + \mu \nabla^2 \vec{V} + ((\vec{B} \cdot \nabla) \vec{B} / \mu_o) - (\nabla B^2 / (2 * \mu_o)) \quad (2.18)$$

$$\nabla \cdot \vec{V} = 0 \quad (2.19)$$

$$\partial \vec{B} / \partial t = \eta \nabla^2 \vec{B} + \nabla \times (\vec{V} \times \vec{B}) \quad (2.20)$$

$$\nabla \cdot \vec{B} = 0 \quad (2.21)$$

The OpenFOAM solver utilizes a second PISO loop for calculating the magnetic field - BPISO. The pressure analog of BPSIO is the scalar fictitious magnetic field- pB which is used to initiate the loop. Figure(1) shows the governing equations and the scalar values used in the solver.

$$\frac{\partial \mathbf{B}}{\partial t} + \nabla \bullet (\mathbf{V}\mathbf{B}) - \nabla \bullet (\mathbf{B}\mathbf{V}) - \Delta \left(\frac{1}{\mu_0\sigma} \mathbf{B} \right) = 0$$

(a) Governing Equations in the OpenFOAM Solver

```
#include "CourantNo.H"

{
fvVectorMatrix UEqn
(
fvm::ddt(U)
+ fvm::div(phi, U)
- fvc::div(phiB, 2.0*DBU*B)
- fvm::laplacian(nu, U)
+ fvc::grad(DBU*magSqr(B))
);

if (piso.momentumPredictor())
{
solve(UEqn == -fvc::grad(p));
}
```

(b) Momentum Transport Equation

```
dimensionedScalar DB = 1.0/(mu*sigma);
DB.name() = "DB";

dimensionedScalar DBU = 1.0/(2.0*mu*rho);
DBU.name() = "DBU";
```

(c) Dimensionless Scalars

Figure 2.1:

2.2.2 Fluid Model

The Non-Newtonian Power Law scheme is used to define the viscosity of the fluid with the strain rate as follows:

$$\vartheta = K\gamma^{n-1} \quad (2.22)$$

where,

K - Consistency Coefficient

γ - Intensity of Strain Rate

n - Power-law index

The values of n used in this study is 1 (Newtonian) and 0.6, 1.2 (Non-Newtonian). The value of $n < 1$ defines a shear-thinning fluid in which the fluid's viscosity decreases as it is subjected to shearing force.

2.3 Problem Definition and Case Setup

2.3.1 Computational Domain and Non-dimensional Parameters

The computational domain consists of a square cavity with the upper wall given a shearing motion. The dimensions of the computational domain are 0.1 m by 0.1 m by 0.01m.

	Pressure	Velocity	Magnetic Field(Tesla)	pB
Top Wall	zeroGradient	(V,0,0)	zeroGradient	0
Bottom Wall	ZeroGradient	(-V,0,0)	zeroGradient	0
Fixed (side) Walls	zeroGradient	noSlip	zeroGradient	0

Figure 2.2: Boundary Conditions

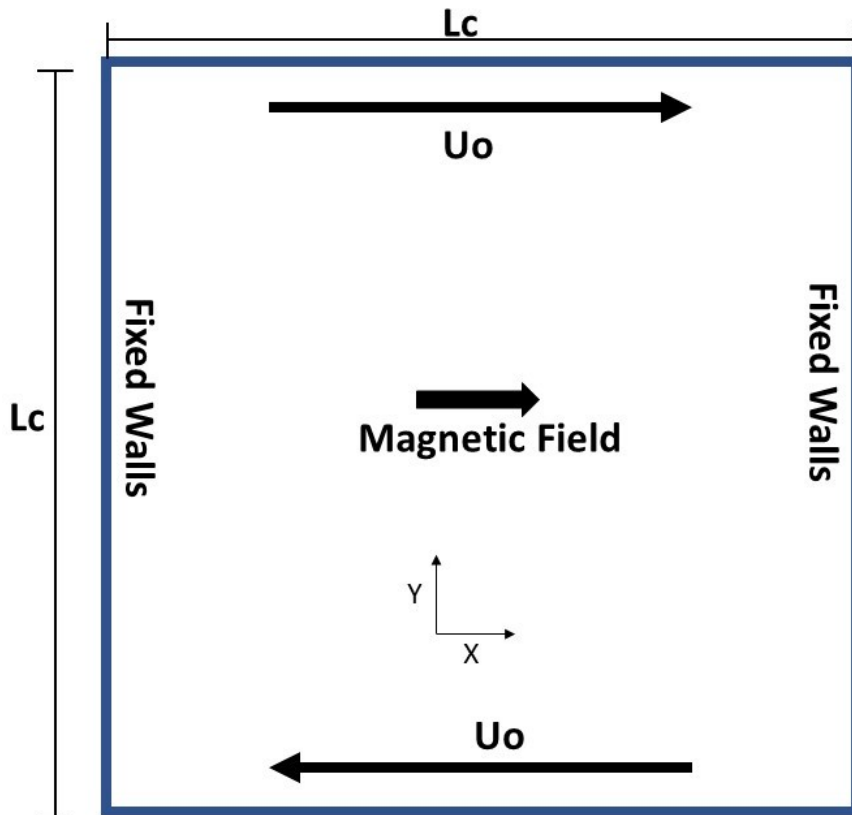


Figure 2.3: Computational domain

Uniform homogeneous external magnetic field is applied in the domain in the positive 'x' direction. The walls are assumed to be perfectly conducting and the flow is assumed to be incompressible and induction-less.

The following dimensionless parameters are used in the study:

1. Hartmann Number (Ha) which is expressed as a ratio of the electromagnetic force and the viscous forces.

$$B \left(\frac{L_c^{n+1} \sigma}{V_c^{n-1} K} \right)^{1/2} \quad (2.23)$$

2. Reynolds Number (Re) which is expressed as the ratio of inertial force to the viscous force

$$\left(\frac{\rho V_c^{2-n} L_c^n}{K} \right) \quad (2.24)$$

3. Stuart Number which is expressed as the ratio of electromagnetic force to the inertia force

$$\left(\frac{Ha^2}{Re} \right) \quad (2.25)$$

where σ is the conductivity of the fluid, L_c is the characteristic length of the cavity, V_c the velocity of the upper wall K consistency coefficient

2.3.2 Case Setup

The computational grid consists of a 200x200 number of cells with the size of the grid cells reduced near the walls to capture the near-wall gradients.

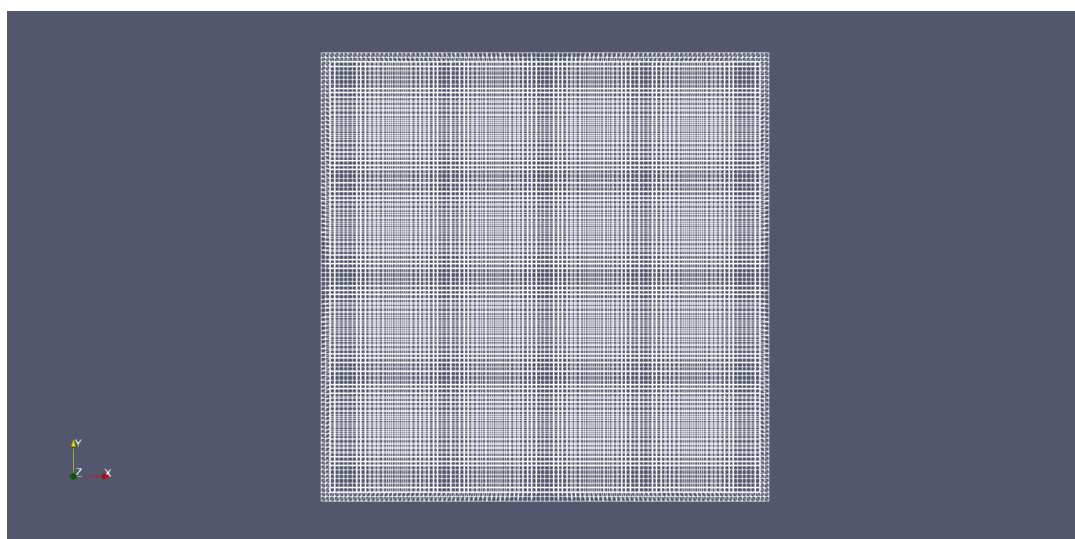


Figure 2.4: Computational Grid

The fluid properties are given below in the table:

Property	Property Value	SI units
Density	1060	kg/m^3
Consistency Coefficient	0.004	kg/ms
Maximum Dynamic Viscosity	0.01	kg/ms
Minimum Dynamic Viscosity	0.001	kg/ms
Power Law Index	1-Newtonian , 0.6-Non-Newtonian	
Electrical Conductivity	0.625	S/m
Magnetic Constant	1.257E-06	H/m

Figure 2.5: Fluid Properties

The values of the uniform magnetic field is calculated for each of the eight cases based on the Stuart number and the values of the characteristic length and the fluid properties.

Stuart Number	Newtonian(n=1)	Non-Newtonian(n=0.6)
0	(0,0,0)	(0,0,0)
5	(8 0 0)	(12.77647 0 0)
10	(25.29822 0 0)	(40.40274 0 0)
50	(56.56854 0 0)	(90.34328 0 0)

Figure 2.6: Values of Magnetic Field

Reynolds number has been kept constant at 100 . The time step is taken as 0.005s and all cases are run to 350 seconds.

2.4 Results and Discussion

2.4.1 Validation

The data published in Kefayati(2014)[10] is compared for the four Stuart numbers with the fluid taken as Newtonian($n=1$) and Reynolds number of 100. The graphs plotted are along the cavity height (y-axis) and the values of the x-component of velocity divided by the magnitude (0.003773585 m/s for Newtonian).

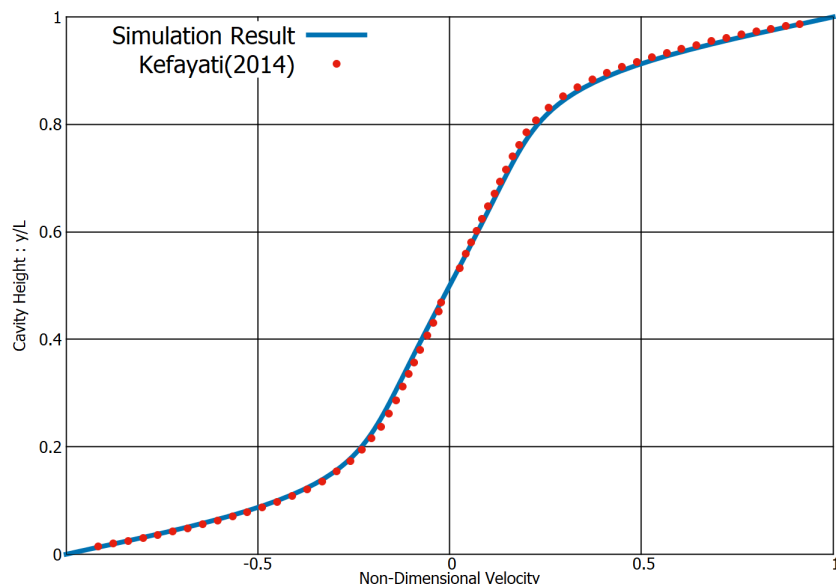


Figure 2.7: Stuart Number=0

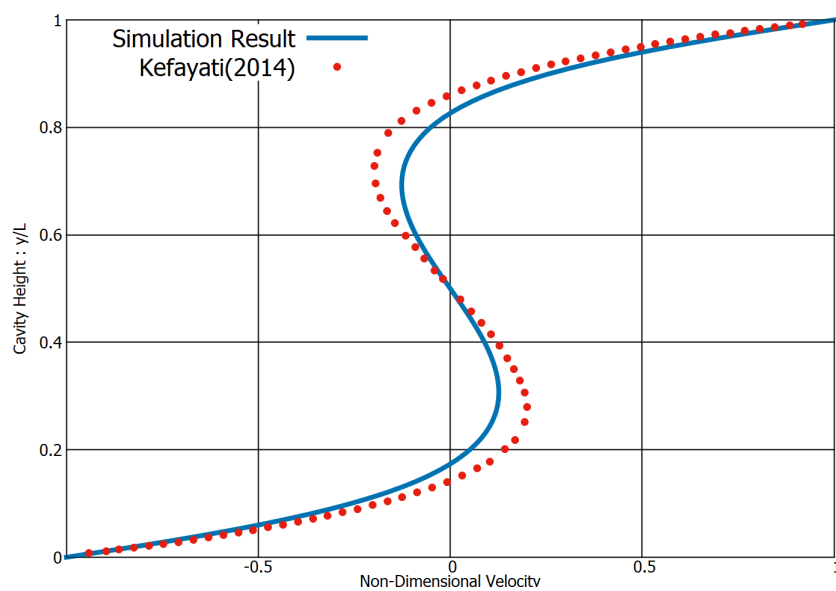


Figure 2.8: Stuart Number=1

46 Results and Discussion

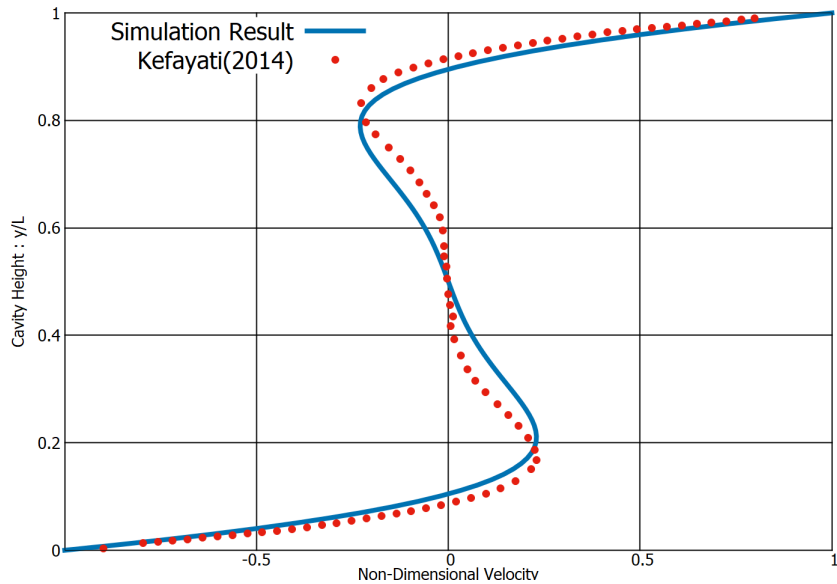


Figure 2.9: Stuart Number =10

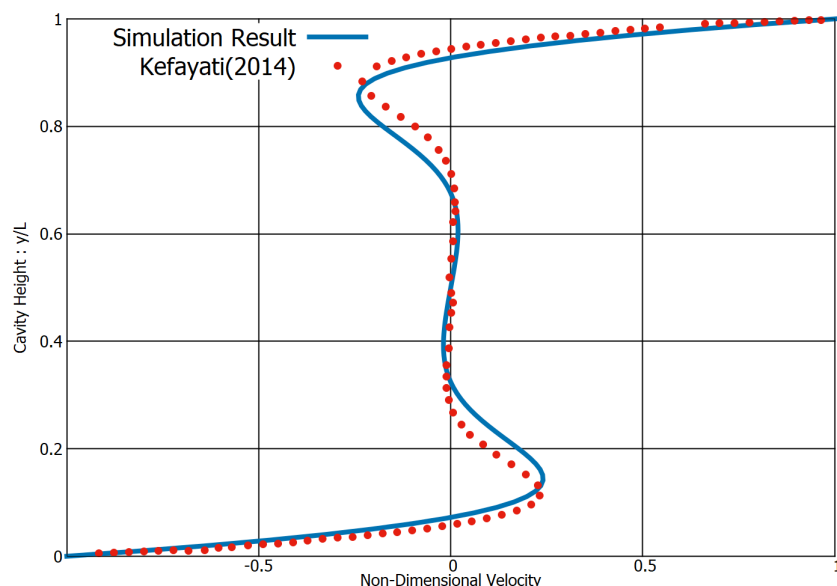


Figure 2.10: Stuart Number=50

The validation is carried on for non-newtonain fluid with a power-law index of 0.6 and Reynolds number of 100.

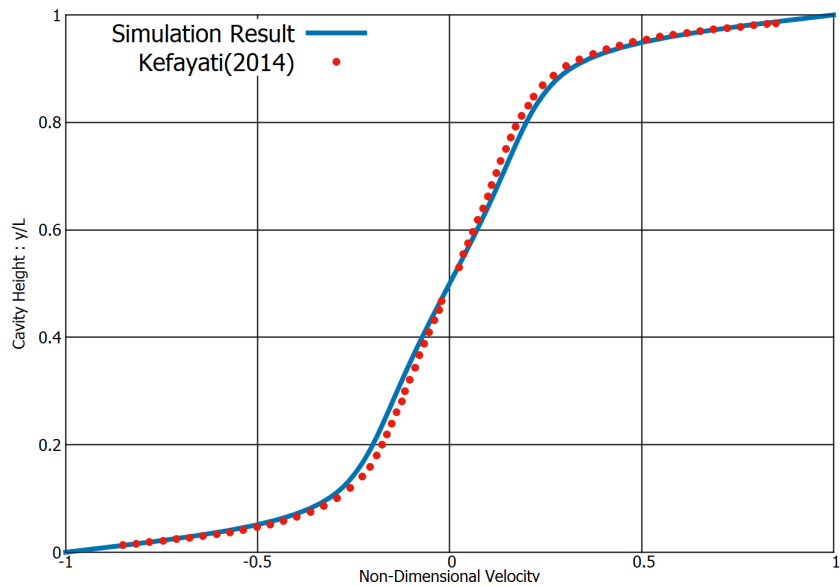


Figure 2.11: Stuart Number=0

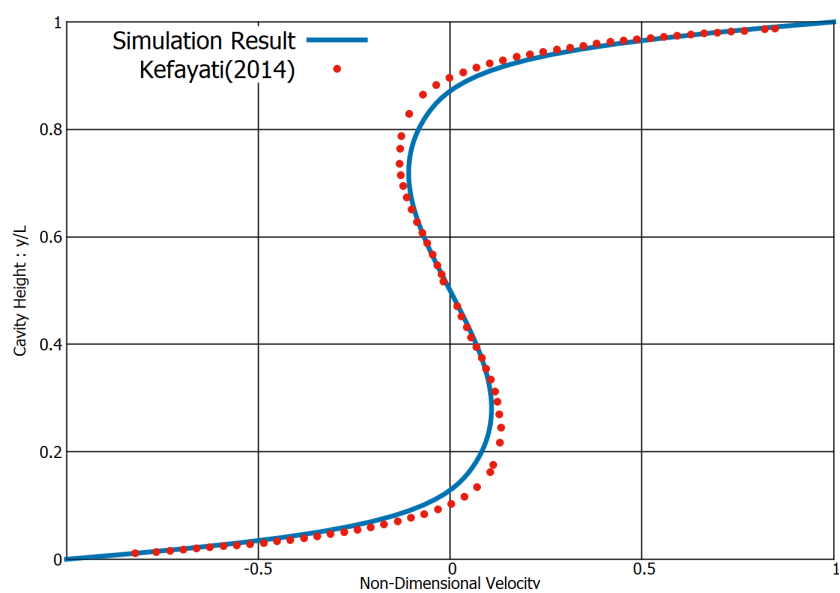


Figure 2.12: Stuart Number=1

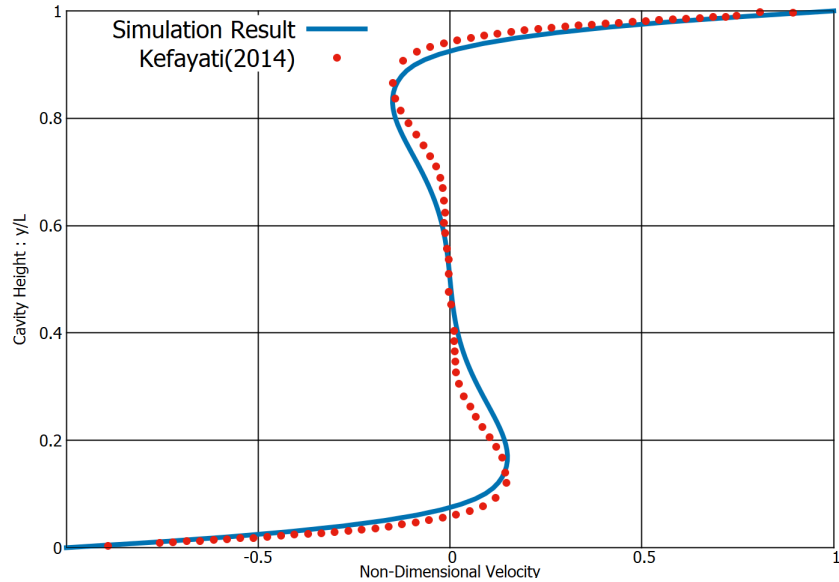


Figure 2.13: Stuart Number =10

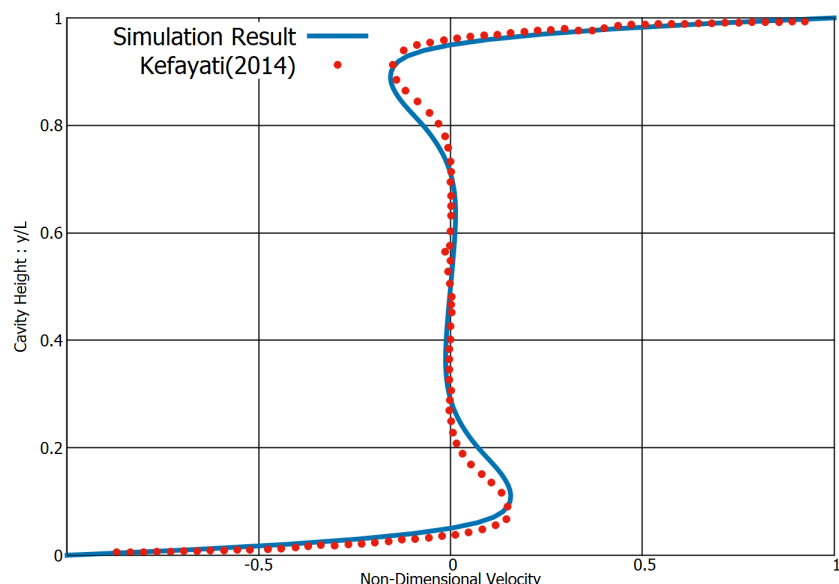
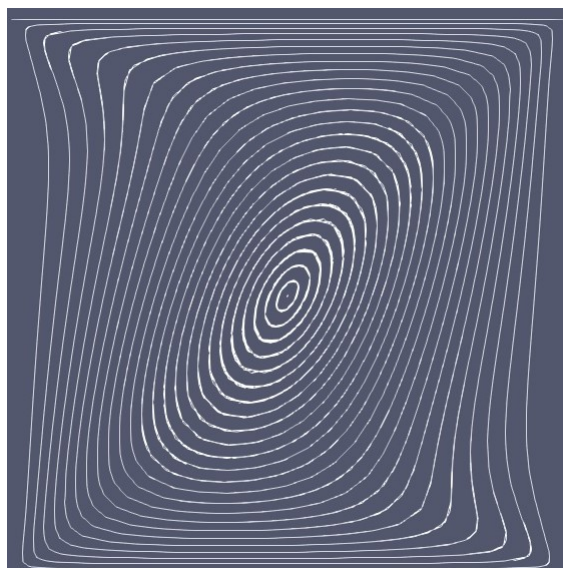


Figure 2.14: Stuart Number=50

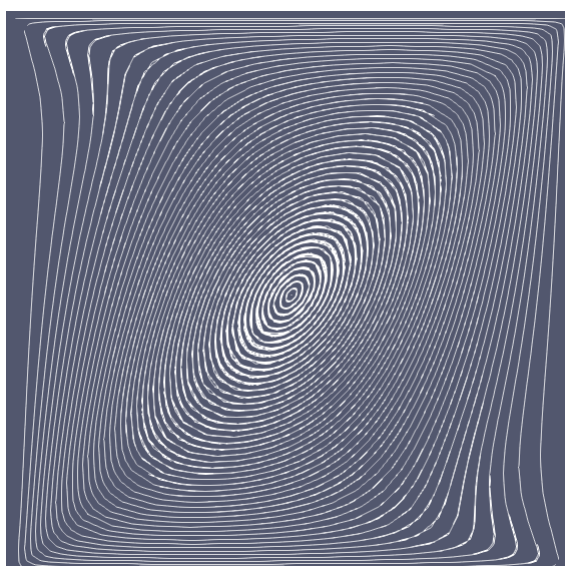
The validation study shows that simulation data to be in close agreement with the experimental data published by Kefayati(2014)[10]

2.4.2 Comparison of Newtonian and Non-Newtonian Results

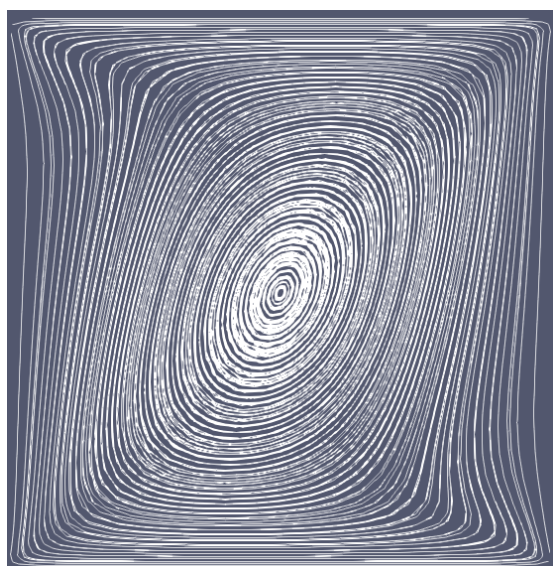
2.4.2.1 Streamlines



(a) Newtonian

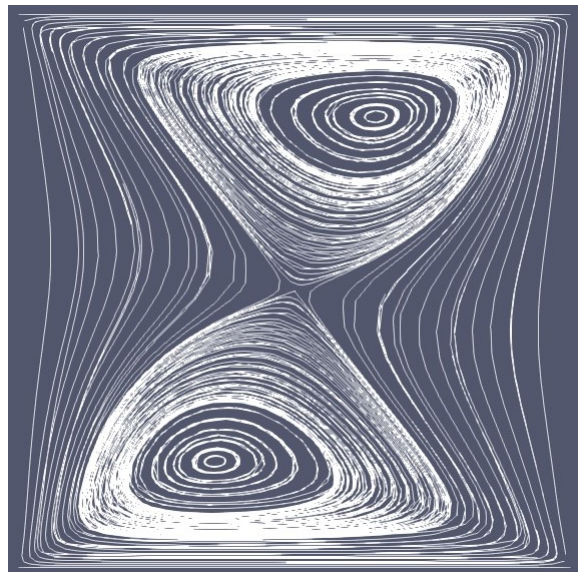


(b) Shear-Thinning

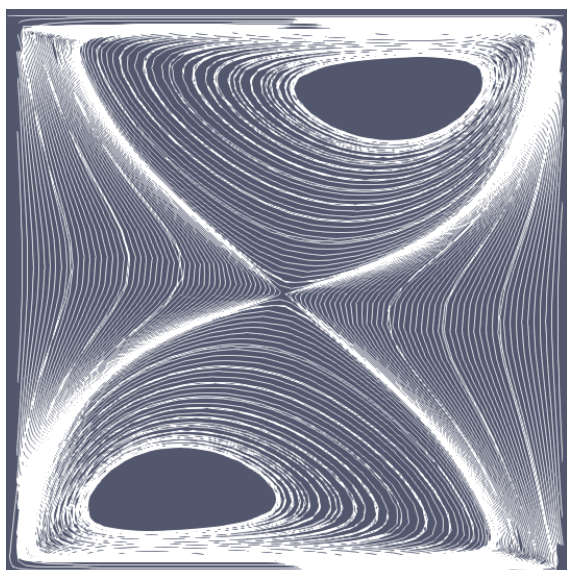


(c) Shear-Thickening

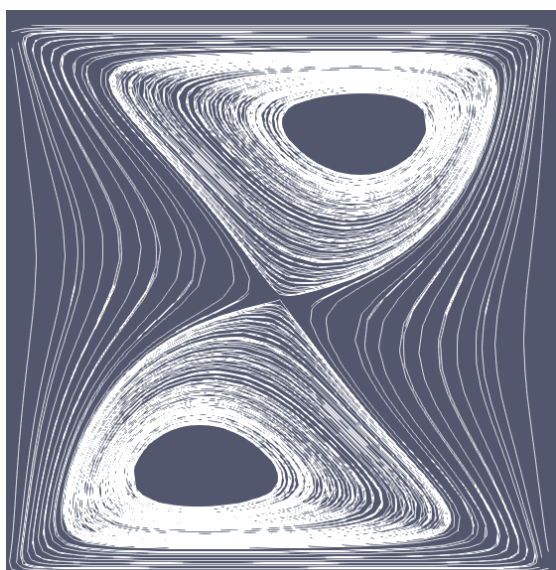
Figure 2.15: Stuart number=0



(a) Newtonian

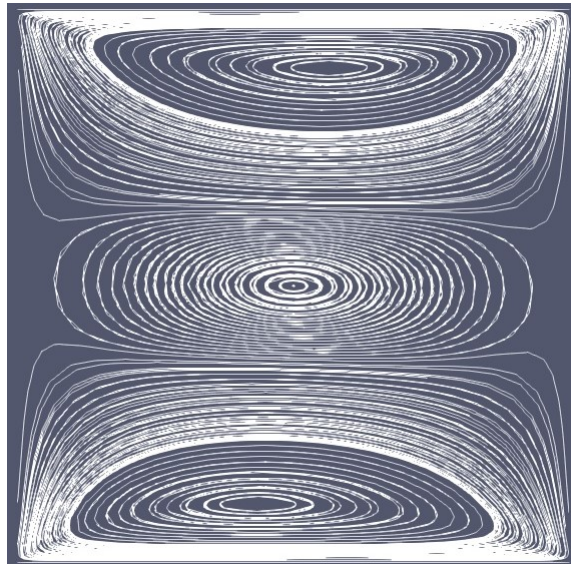


(b) Shear-Thinning

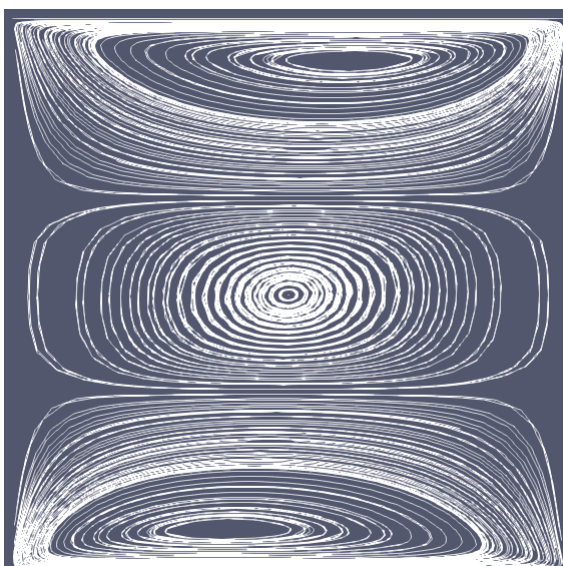


(c) Shear-Thickening

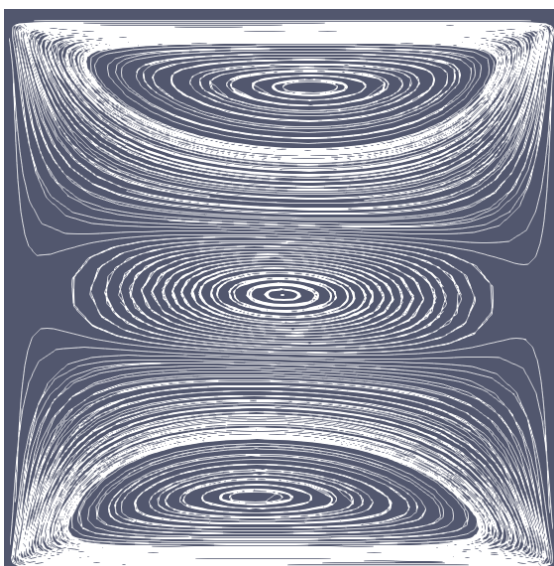
Figure 2.16: Stuart number=1



(a) Newtonian

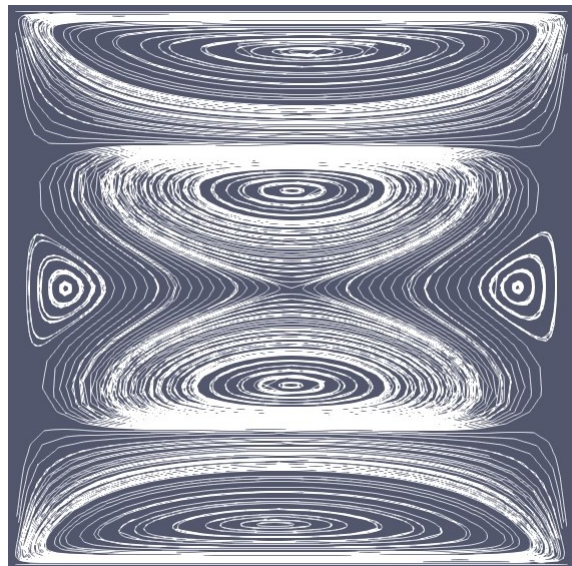


(b) Shear-Thinning

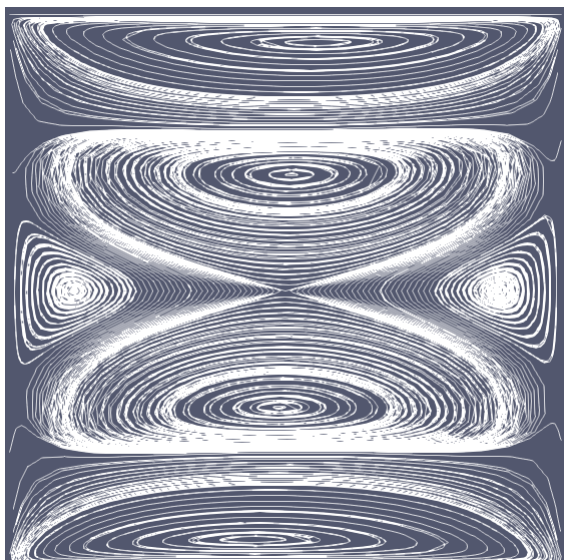


(c) Shear-Thickening

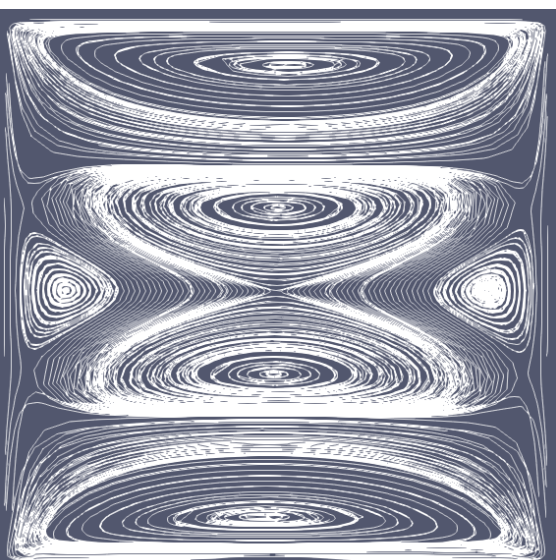
Figure 2.17: Stuart number=10



(a) Newtonian



(b) Shear-Thinning



(c) Shear-Thickening

Figure 2.18: Stuart number=50

2.4.2.2 Velocity Plot Result

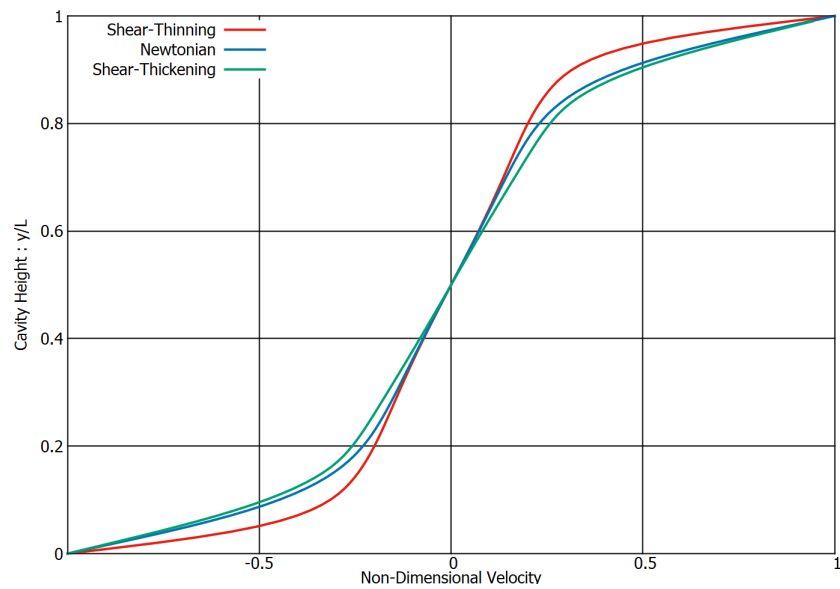


Figure 2.19: Stuart Number=0

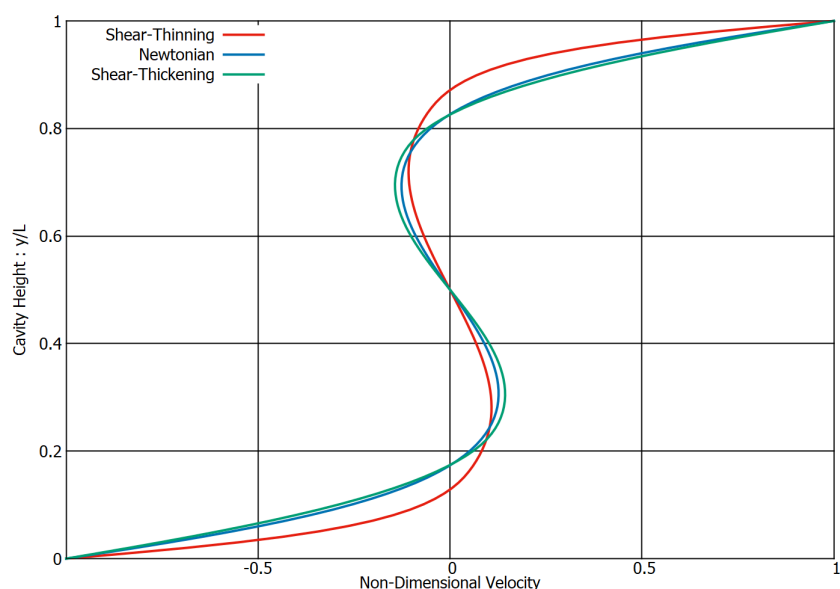


Figure 2.20: Stuart Number=1

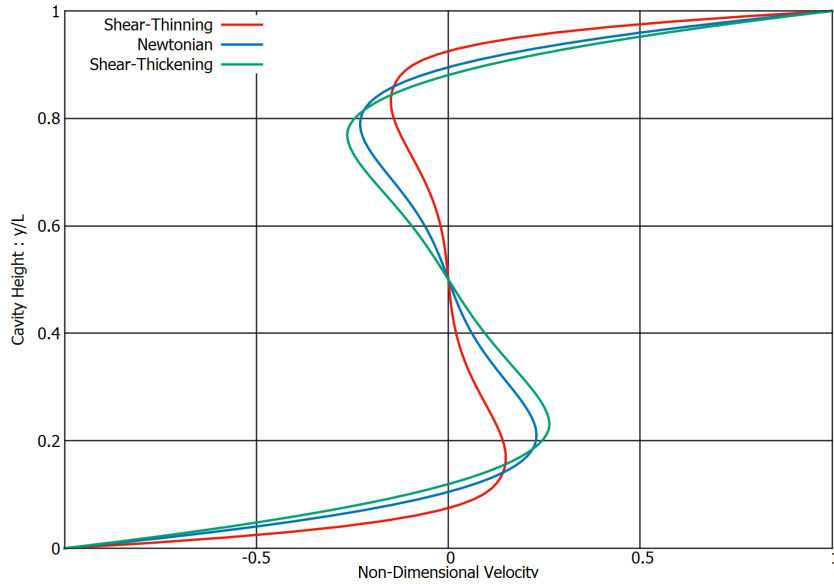


Figure 2.21: Stuart Number=10

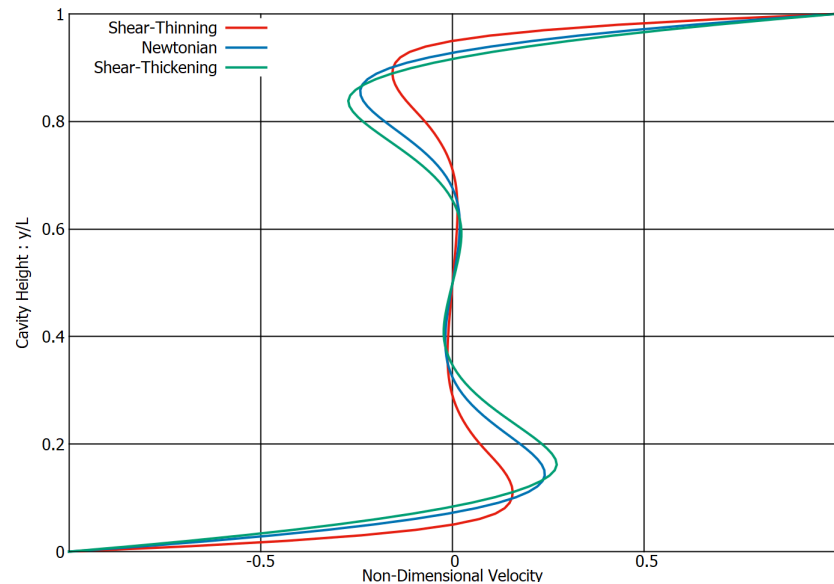


Figure 2.22: Stuart Number=50

2.5 Conclusions

The streamlines presented in Figures[2.15,2.16,2.17,2.18] show that the effect of the external magnetic field is to split the core vortex into multiple smaller vortices. The core vortex consists of a single clockwise vortex when no magnetic field is applied. For a Stuart number of 12.16, the flow splits into two clockwise vortices. The flow is split into three vortices for Stuart number=10 which consists of a central anti-clockwise vortex and two clockwise vortices at the top and bottom. The central antitwistwise vortex is further split into two anti-clockwise vortices for the Stuart number=50 , in addition, two clockwise vortices appear

in the left and the right. The velocity plot in Figures[2.7,2.8,2.9,2.10] indicate that the simulation results are in close agreement with the published data. In Figure[2.7] the velocity profile is symmetric and is positive in the top half and negative in the bottom half: further due to the symmetric nature the velocity become zero for the center of the domain. Since the core vortex is split into two for Stuart Number=1 the Figure[2.8] depicts an "S" shaped profile. The profile in Figures[2.9,2.10] has a decreased peak value of velocity magnitude(maximum distance from the zero-velocity line) due to the formation of an anti-clockwise vortex in the center. It therefore can be inferred though that the total magnitude of the velocity decreases for increased Stuart numbers since the profile is closer to the zero-velocity vertical line: this suggest that the magnetic field weakens the strength of the core vortex. A comparison of the Newtonian and non-Newtonian fluid profiles is presented in Figure[2.19,2.20,2.21,2.22] which illustrate that the decrease in the magnitude of absolute velocity for a given Stuart number is more for the shear-thinning fluid, followed by the Newtonian fluid and by shear-thickening. The deviation for shear-thickening is lesser than the shear-thinning since 1.2 power-law was closer to Newtonian fluid than 0.6 power-law. Therefore it can be concluded that the influence of the magnetic filed is higher for a shear-thinning fluid compared to a shear-thickening fluid.

CHAPTER 3

Thermal Effects

3.1 Introduction

Convection is a form of heat transfer which is facilitated through the motion of fluid. In case of "Forced Convection" the fluid motion is due to an external force such as an upper shearing wall used in this study. When the fluid is set into motion due to body forces arising from density difference due to different temperature- the convection currents are induced- this form of convection is termed- "Natural Convection". In this study both natural and forced convection phenomena are studied in-depth through CFD simulation of a single phase fluid in a lid-driven cavity. The reference papers used for the study are "Santos et al(2013)" for forced convection and "Wan et al (2001)"

The energy equation is a P.D.E which included thermal energy in the form of absolute temperature as a transport equation. This transport equation is solved in the study to determine the distribution of temperature throughout the fluid domain. The temperature is modeled as a scalar. The first form of temperature transport is through diffusion which is represented as the laplacian in the right hand side. The convection transport is the has the velocity vector attached with the temperature gradient as a dot product. Therefore the PISO algorithm is implemented to determine the velocity distribution in the domain before the temperature distribution is plotted. The time dependence time makes the equation a transient equation. Since the equation is perfectly linear, a pseudo temperature value is not required for making the equation linear. (unlike the non-linear Navier Stokes equation which uses "phiU").

$$\frac{\partial T}{\partial t} + V \cdot \nabla T = \nabla^2 T \quad (3.1)$$

3.1.1 Dimensionless Parameters

The thermal diffusivity which is indicated by the symbol α is the ability of a material to transfer heat compared to its heat capacity and density. It is represented by the thermal conductivity(k) of the material divided by the product of the density(ρ)and the heat storage capacity (specific heat capacity) - C_p .

$$\alpha = \frac{k}{\rho C_p} \quad (3.2)$$

The other non-dimensional number used for forced convection study is the Prandtl's number which is the ratio of the kinematic diffusivity to the thermal diffusivity.

$$Pr = \frac{\nu}{\alpha} \quad (3.3)$$

The non-dimensional parameters used in the natural convection portion of the study are given here:

$$x = \frac{\bar{x}}{L_c}, y = \frac{\bar{y}}{L_c} \quad (3.4)$$

$$u = \frac{\bar{u}L_c}{\alpha}, v = \frac{\bar{v}L_c}{\alpha} \quad (3.5)$$

$$t = \frac{\alpha \bar{t}}{L_c^2} \quad (3.6)$$

$$p = \frac{\bar{p}L_c^2}{\rho \alpha^2} \quad (3.7)$$

$$Pr = \frac{\nu}{\alpha} \quad (3.8)$$

where, L_c is the cavity length, α is the thermal diffusivity, \bar{x}, \bar{y} are dimensional coordinates, \bar{T} is the dimensional temperature (in kelvin) , T_c, T_H are the dimensional extreme temperatures.

The Grashof Number is the ratio of the buoyancy forces to the viscous forces- this parameter is significant in controlling convection flow, , it is given as:

$$Gr = \frac{g\beta TL_c^3}{\vartheta^2} \quad (3.9)$$

The parameter of interest in this study is the Rayleigh number which is the product of Grashof's number and the Prandtl's number, which is given as:

$$Ra = Pr * Gr = \frac{g\beta TL_c^3}{\vartheta\alpha} \quad (3.10)$$

where ,

g is the acceleration due to gravity

β is coefficient of thermal expansion

ϑ is the kinematic viscosity

L_c is the characteristic length of the cavity

α is the thermal diffusivity

3.1.2 Governing Equations

3.1.2.1 Forced Convection

In addition to the standard Navier-Stokes equations of continuity and momentum- the energy equation is also solved for the temperature distribution.

The governing equations used for forced convection are:

$$\nabla \cdot V = 0 \quad (3.11)$$

$$\frac{\partial u}{\partial t} + V \cdot \nabla u = -\nabla p + Pr \nabla^2 u \quad (3.12)$$

$$\frac{\partial v}{\partial t} + V \cdot \nabla v = -\nabla p + Pr \nabla^2 v \quad (3.13)$$

$$\frac{\partial T}{\partial t} + V \cdot \nabla T = \nabla^2 T \quad (3.14)$$

3.1.2.2 Natural Convection

The buoyancy effect due to density differences are included in the momentum equation for the vertical component of fluid velocity as a body force. The body force is given as the product of the Rayleigh number and the Prandtl's number.

The governing equations used for natural convection are:

$$\nabla \cdot V = 0 \quad (3.15)$$

$$\frac{\partial u}{\partial t} + V \cdot \nabla u = -\nabla p + Pr \nabla^2 u \quad (3.16)$$

$$\frac{\partial v}{\partial t} + V \cdot \nabla v = -\nabla p + Pr \nabla^2 v + Ra Pr T \quad (3.17)$$

$$\frac{\partial T}{\partial t} + V \cdot \nabla T = \nabla^2 T \quad (3.18)$$

3.2 Problem Definition and Case Setup

3.2.1 Forced Convection

3.2.1.1 Computational Domain and Boundary Conditions

A 2-D square cavity of 60x60 mesh is used as the computational grid.

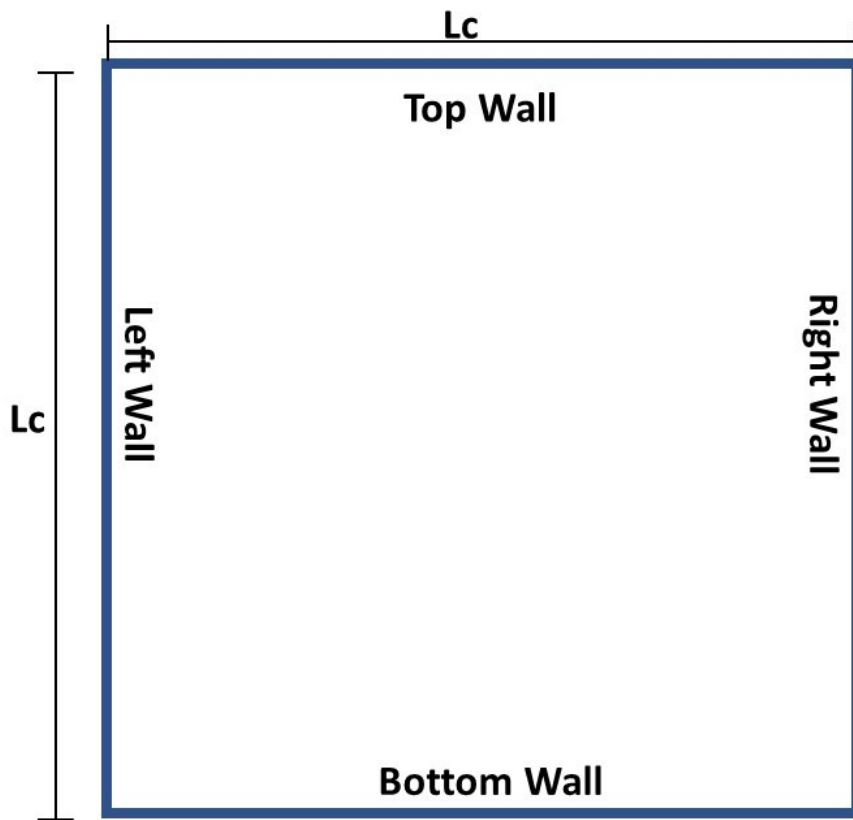


Figure 3.1: Domain

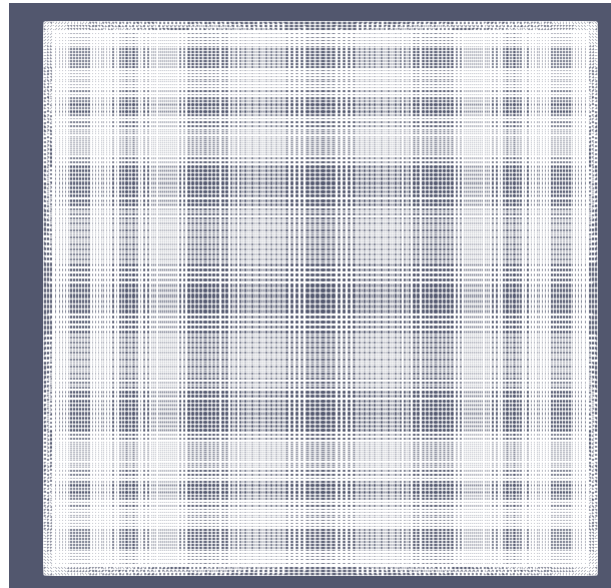


Figure 3.2: Computational Grid

The two cases considered in the study for forced convection are Reynolds numbers of 100 and 1000. The velocity of the top moving wall is given as 1 m/s , the corresponding kinematic viscosity for both cases are 0.001 and 0.0001 respectively. The remaining sides are given a “noSlip” condition. The thermal diffusivity has been taken equal to the kinematic viscosity so that the Prandtl’s number is equal to 1 ($\alpha = \eta$). The top wall was given a uniform temperature of 350 kelvin and the remaining walls were given 300 kelvin.

	Velocity	Pressure	Temperature(non-dimensional)
Top-Wall	(1,0,0)	zeroGradient	350
Left-Wall	noSlip	zeroGradient	300
Right-Wall	noSlip	zeroGradient	300
Bottom-Wall	noSlip	zeroGradient	zeroGradient

Figure 3.3: Boundary Conditions

3.2.1.2 Solver

The incompressible laminar solver- “icoFoam” has been modified to include the energy equation- an extra field termed ”T” has been added for representing the temperature. The figure below show the energy equation added to the icoFoam solver.

```
fvScalarMatrix TEqn
(
    fvm::ddt(T)
    + fvm::div(phi, T)
    - fvm::laplacian(DT, T)
);
```

Figure 3.4: Energy Equation

3.2.2 Natural Convection

3.2.2.1 Computational Domain and Boundary Conditions,

The computational domain is taken as the standard square 2-D cavity. The grid consists of a 140x140 mesh.

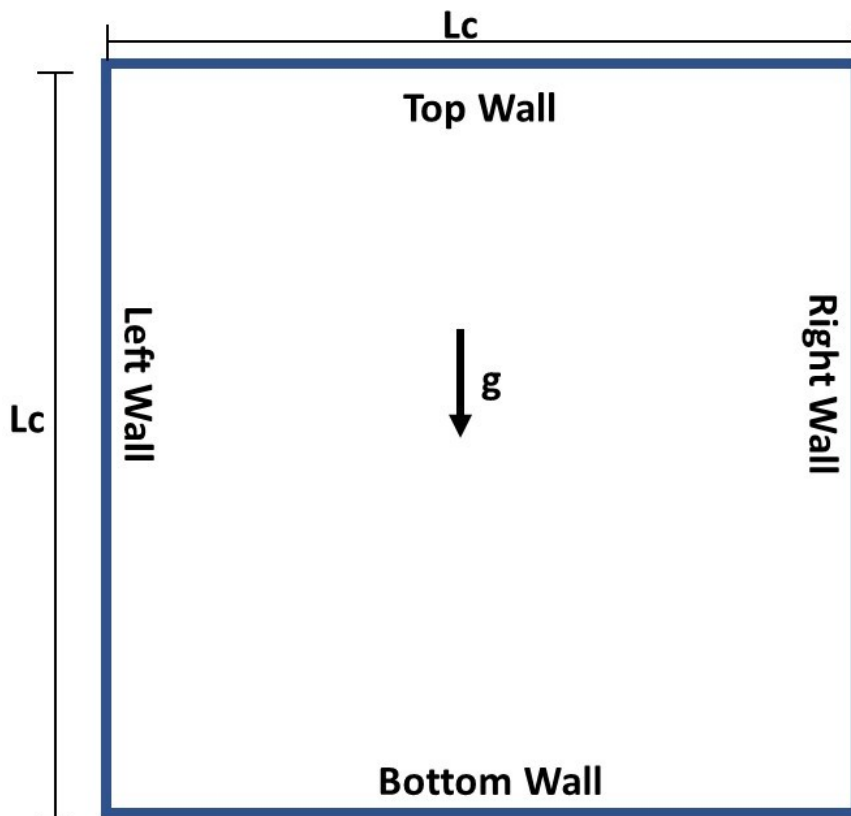


Figure 3.5: Domain

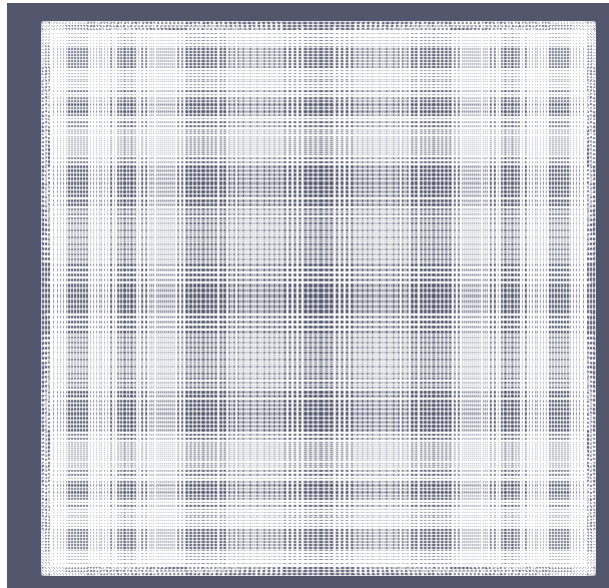


Figure 3.6: Computational Grid

The boundary conditions are given below:

	Velocity	Pressure	Temperature(non-dimensional)
Top-Wall	(0,0,0)	zeroGradient	zeroGradient
Left-Wall	noSlip	zeroGradient	1.0(scalar)
Right-Wall	noSlip	zeroGradient	0.0(scalar)
Bottom-Wall	noSlip	zeroGradient	zeroGradient

Figure 3.7: Boundary Conditions

The Rayleigh numbers considered in this study are - 10000 (1e4) , 100000 (1e5), 1000000 (1e6)

3.2.2.2 Solver

The incompressible laminar solver -ícoFoam'is modified to include natural convection. The momentum equation is modified to include the Rayleigh number and the Prandlt number, however the symbols- β (beta) is used to account for Rayleigh Number and the symbol- g is used to account for the Prandtl number-

further the g is given as a vector- (0,Pr,0) since the buoyancy force is in the vertical direction.

The symbol DT is used for thermal diffusivity (α) , since the DT is taken as equal to unity, $\eta = Pr$

```
// Momentum predictor  
  
fvVectorMatrix UEqn  
(  
    fvm::ddt(U)  
    + fvm::div(phi, U)  
    - fvm::laplacian(nu, U)  
    -beta*g*T  
)
```

(a) Momentum Equation

```
fvScalarMatrix TEqn  
(  
    fvm::ddt(T)  
    + fvm::div(phi, T)  
    - fvm::laplacian(DT, T)  
)
```

(b) Energy Equation

```
dimensionedScalar nu  
(  
    "nu",  
    dimViscosity,  
    transportProperties.lookup("nu")  
);  
  
dimensionedScalar DT  
(  
    "DT",  
    // dimViscosity,  
    transportProperties.lookup("DT")  
);  
  
dimensionedScalar beta  
(  
    "beta",  
    // dimViscosity,  
    transportProperties.lookup("beta")  
);  
  
dimensionedVector g  
(  
    "g",  
    // dimViscosity,  
    transportProperties.lookup("g")  
);
```

(c) Dimensionless Numbers used in the solver

Figure 3.8: Solver Code

3.2.3 Mixed Convection

Convection heat transfer in real life applications like car radiators are driven by a combination of forced and natural convection. The solver and grid are identical to the natural convection case however, the top moving wall is given an imposed velocity resulting in slave-driven and buoyancy-driven flow. Furthermore the top wall is given a dimensionless temperature of 1.0 and bottom wall is given that of 0.0.

	Velocity	Pressure	Temperature(non-dimensional)
Top-Wall	(Uo,0,0)	zeroGradient	1.0(scalar)
Left-Wall	noSlip	zeroGradient	zeroGradient
Right-Wall	noSlip	zeroGradient	zeroGradient
Bottom-Wall	noSlip	zeroGradient	0.0(scalar)

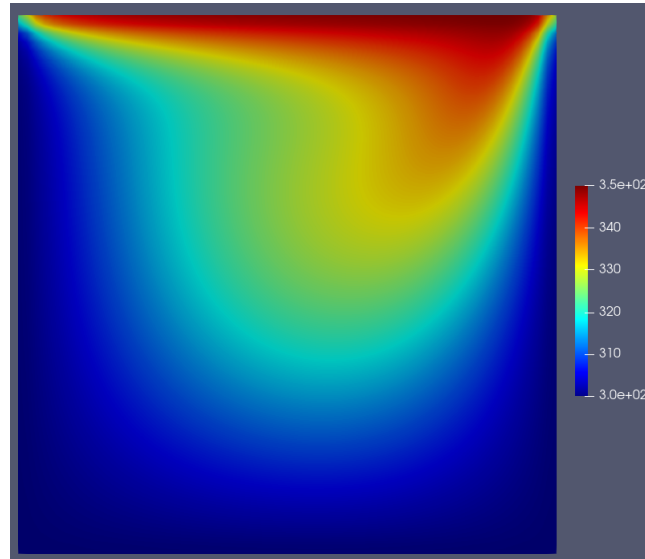
Figure 3.9: Boundary Conditions

3.3 Results and Discussion

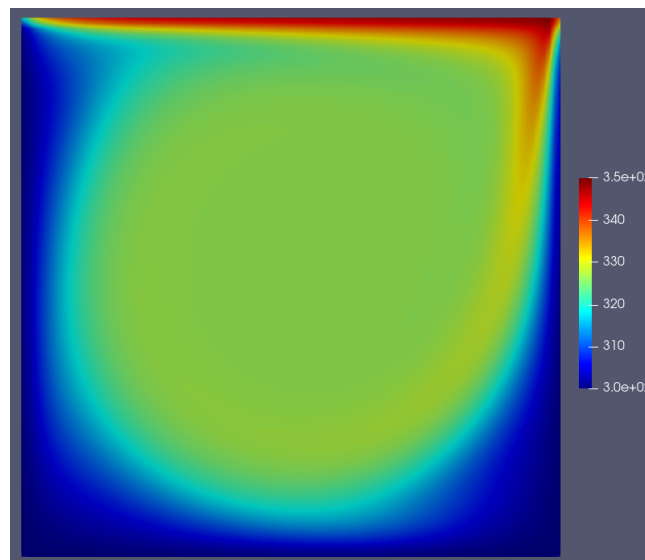
3.3.1 Forced Convection

The Reynolds numbers included in this study are 100 and 1000. For Reynolds number equal 100, the case was run for 50 seconds at a time step of 0.0005 seconds, for the Reynolds number of 1000. the case was run for 300 seconds at the same time step. The simulation data was compared to the data published in Santos et al(2013)[5] for both cases.

The temperature along a vertical line through the middle of the cavity has been plotted as the non-dimensional quantity: $T^* = \frac{(T-300)}{(350-300)}$ along with the cavity height.



(a) Reynolds number=100



(b) Reynolds number=1000

Figure 3.10: Temperature Contour

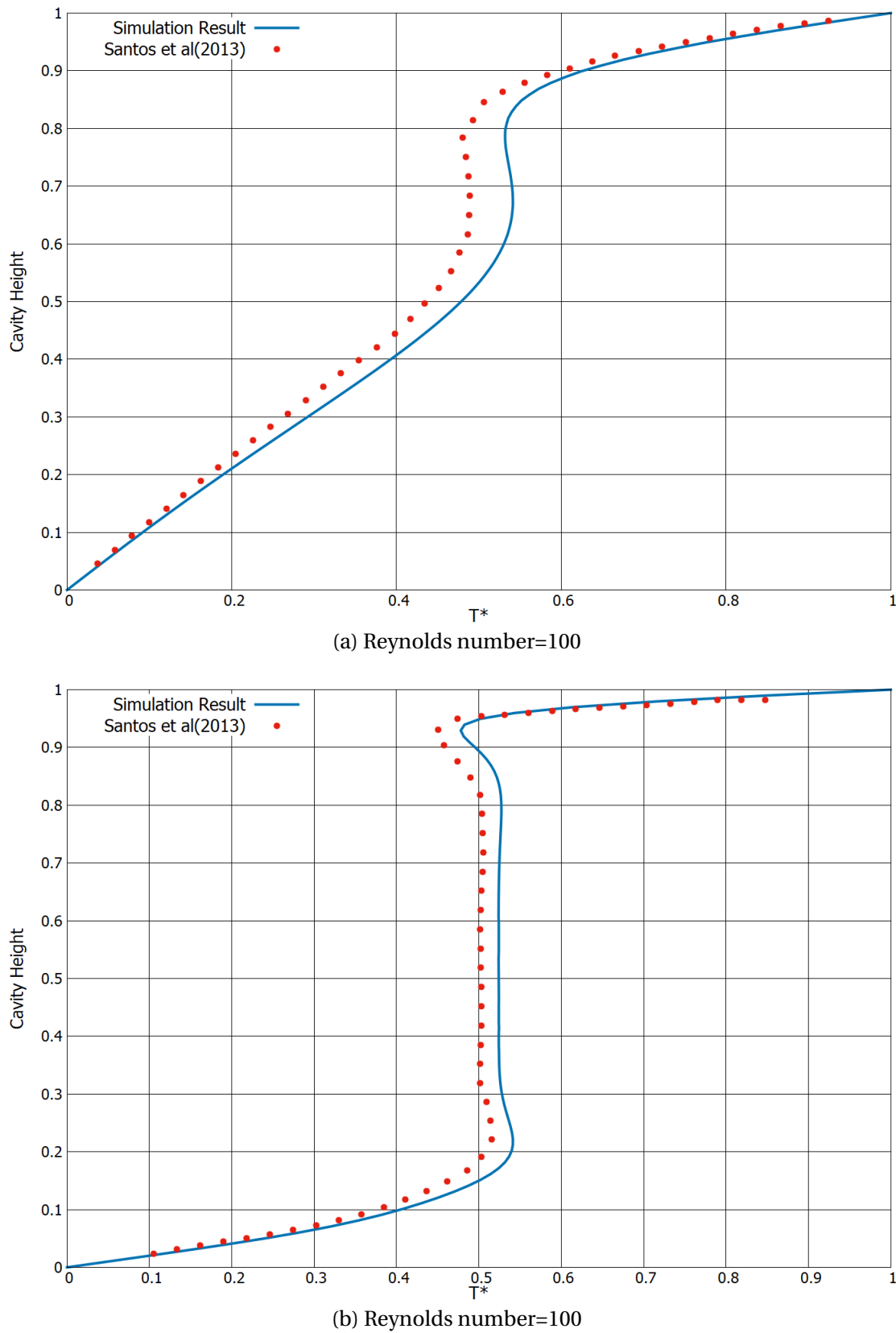


Figure 3.11: Comparison with Santos et al(2013)

3.3.2 Natural Convection

The four different Rayleigh numbers considered in the study- 1e4, 1e5, 1e6, the cases correspond to changes in the β (beta) in the 'transportProperties' file. After the simulation completed 120 seconds at a time step of 0.0005 seconds, the results were compared with the published data of Wan et al (2010)[21].

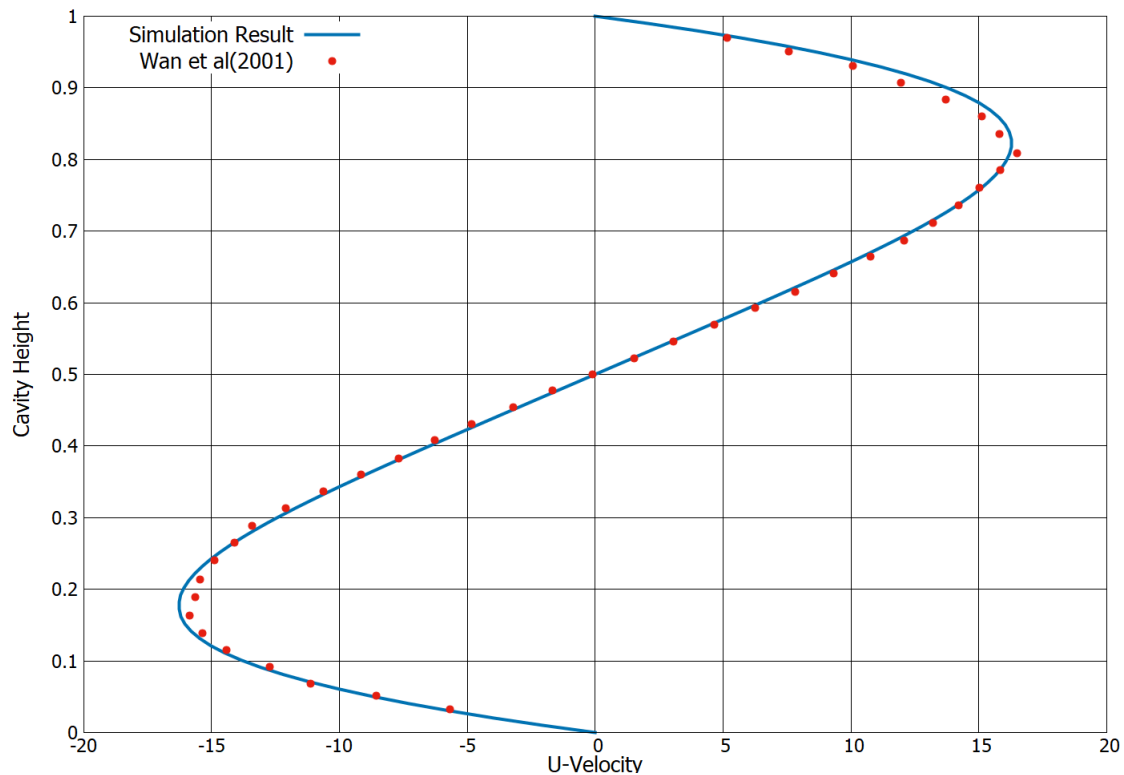


Figure 3.12: Rayleigh number=1e4

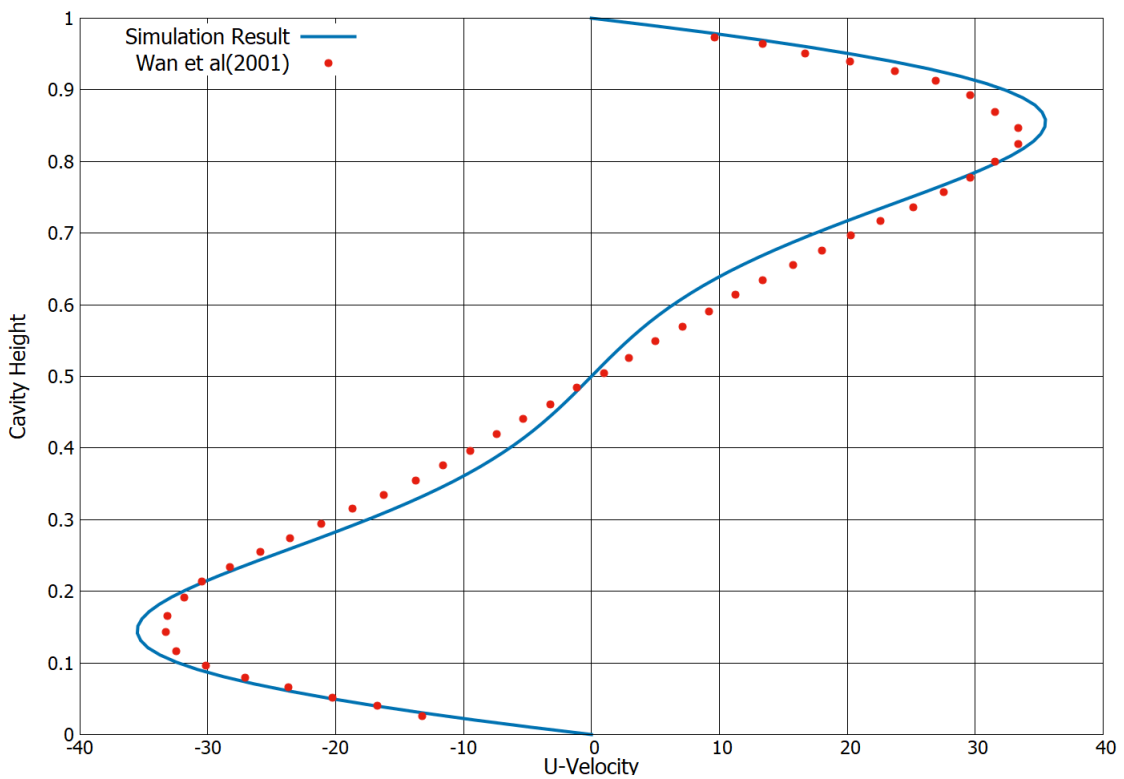


Figure 3.13: Rayleigh number=1e5

70 Results and Discussion

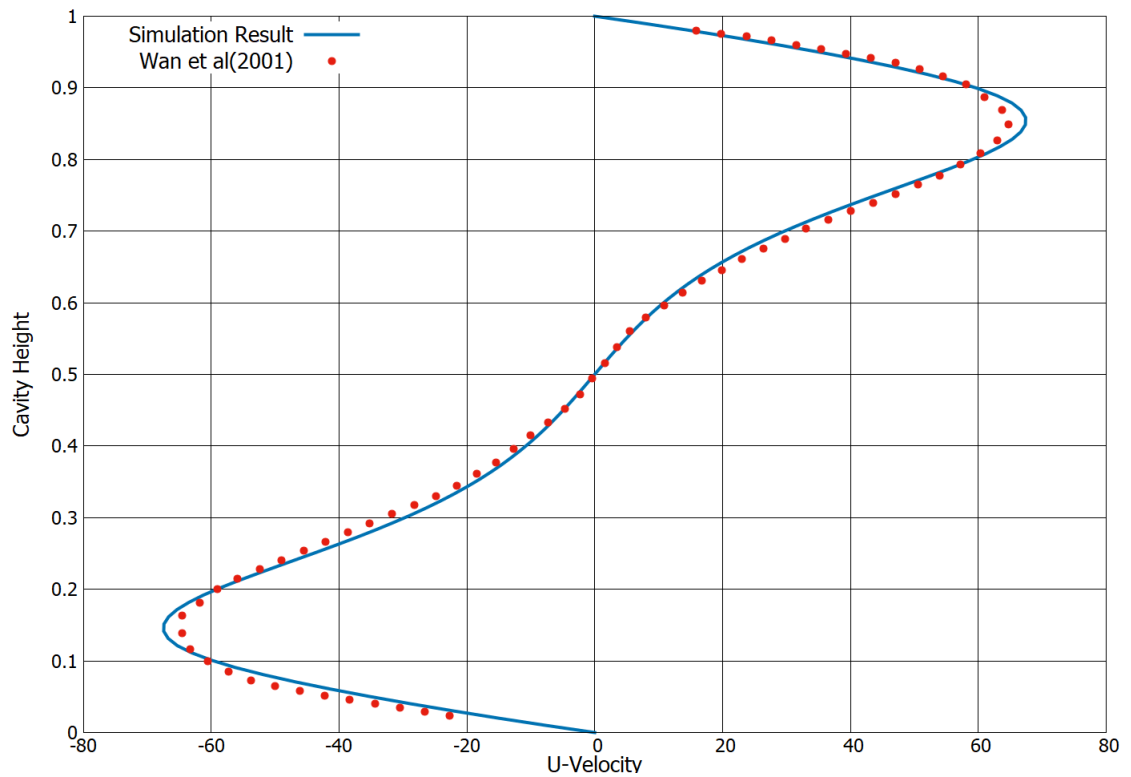


Figure 3.14: Rayleigh number=1e6

3.3.3 Mixed Convection

The cases of Richardson numbers of 0.1, 1.0 and 5.0. Results are compared to Thohura et al (2021)[20].

72 Results and Discussion

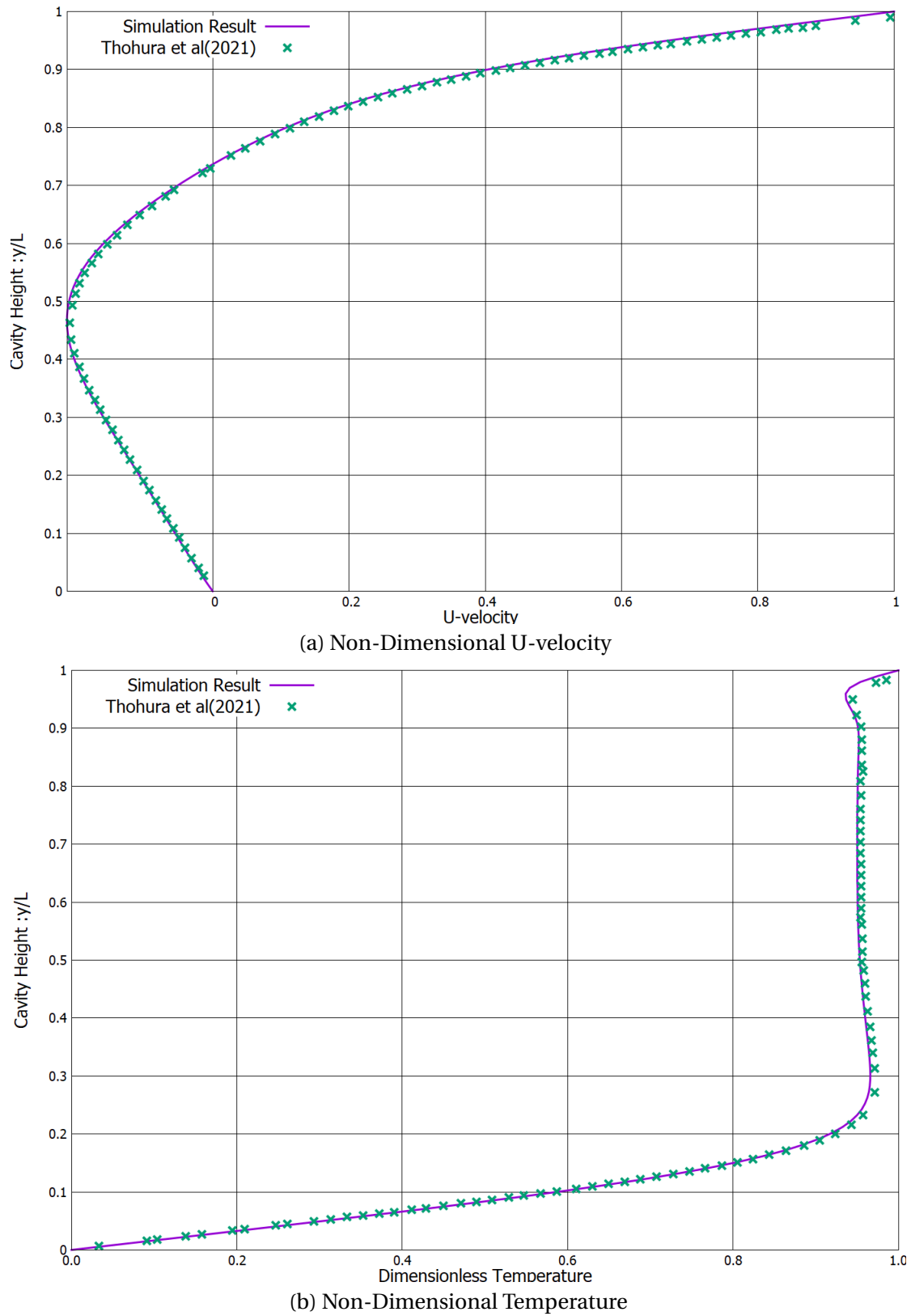


Figure 3.15: Richardson Number=0.1

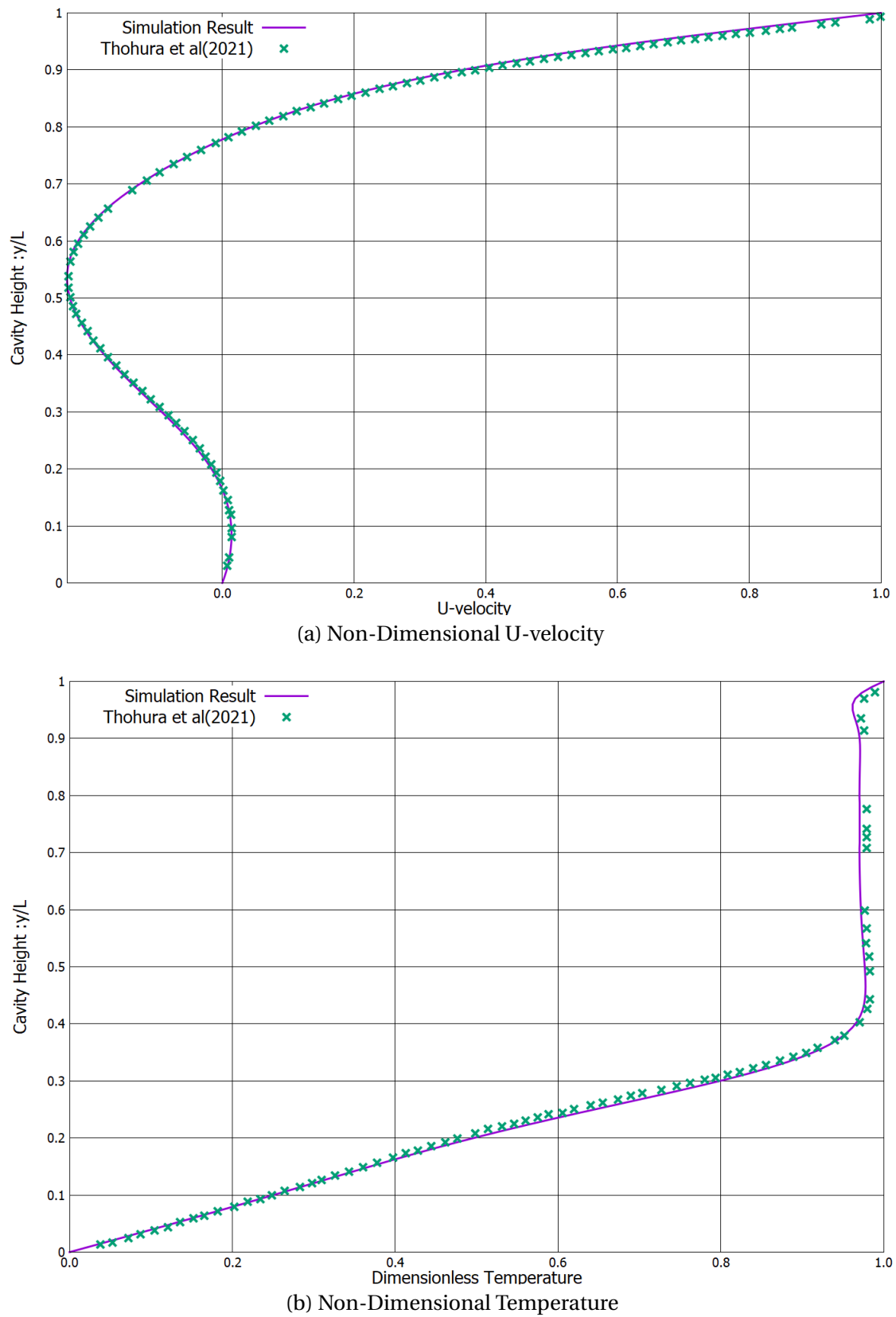


Figure 3.16: Richardson Number=1

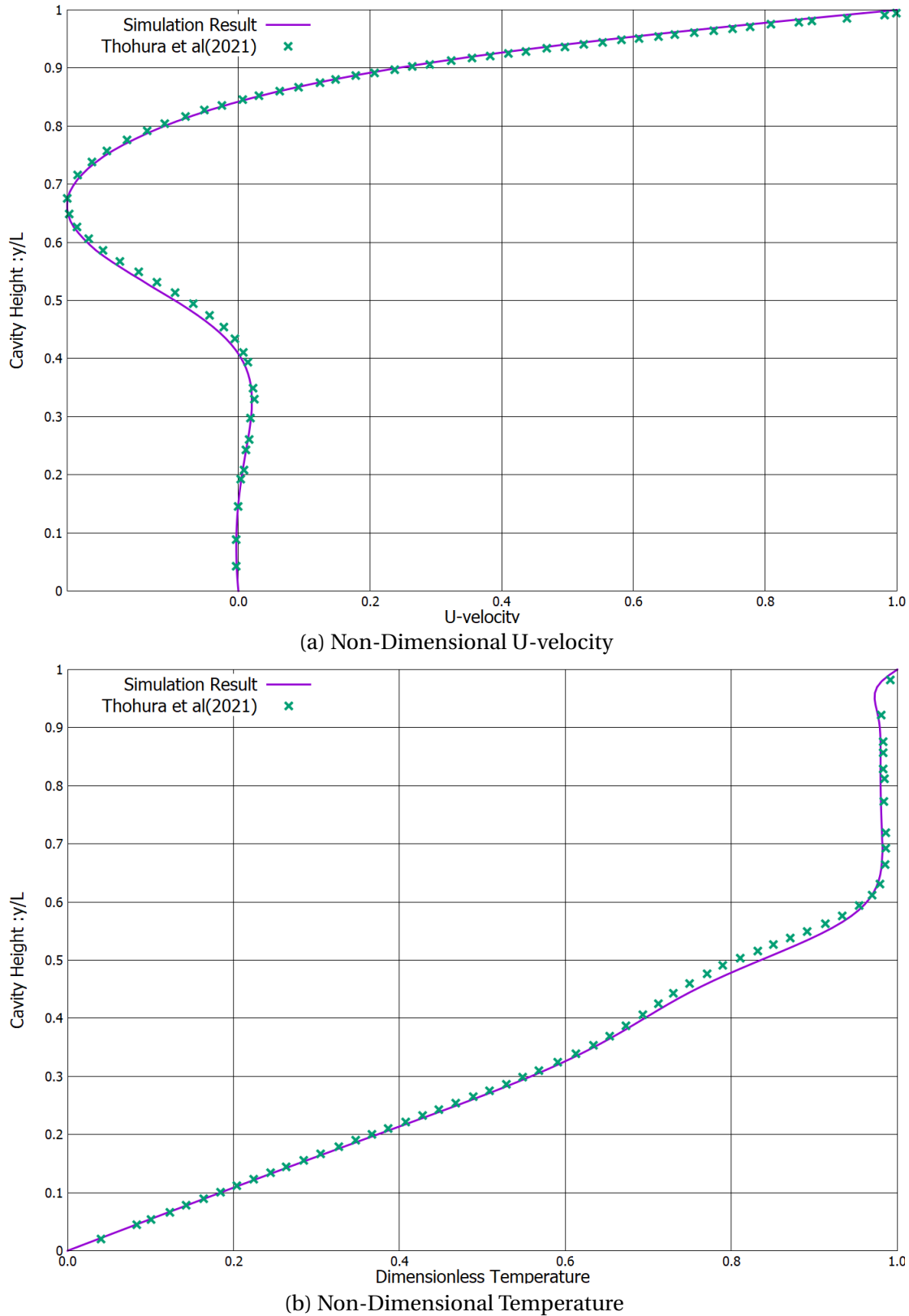


Figure 3.17: Richardson Number=5

The validation study is further extended for Iwatsu(1993) [9]. The results are presented for Grashof number of 1e6 and Reynolds numbers of 100, 400, 1000 and 3000 with the Prandtl number as 0.71.

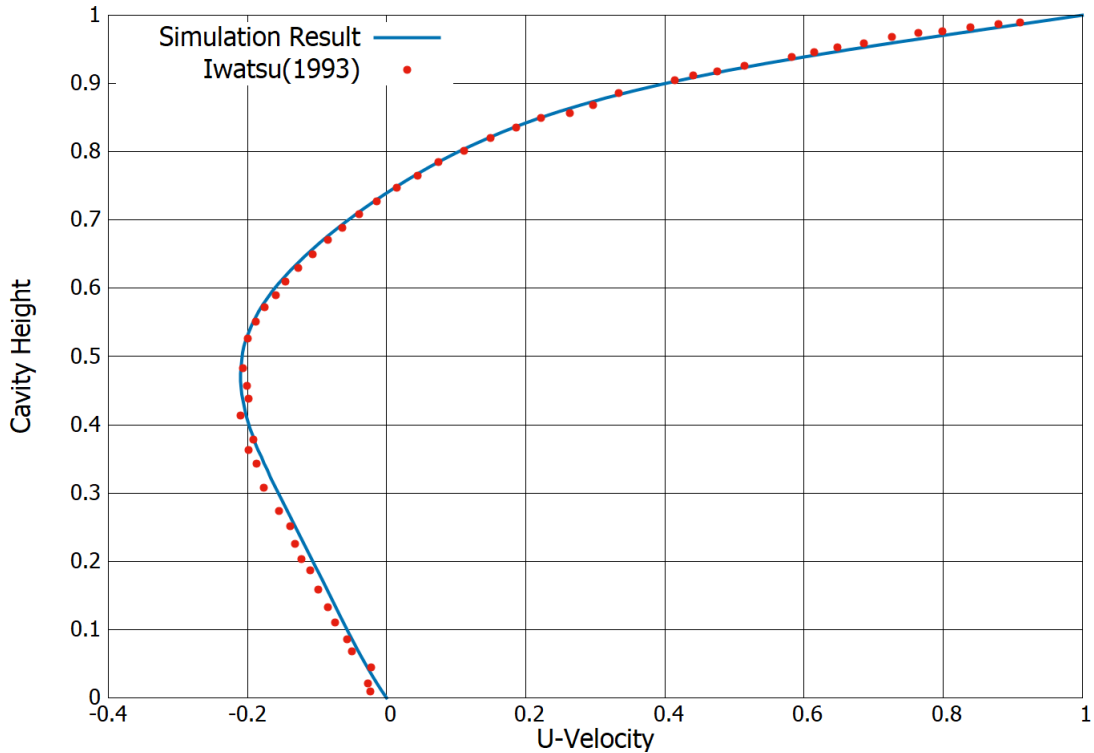


Figure 3.18: Reynolds Number =100

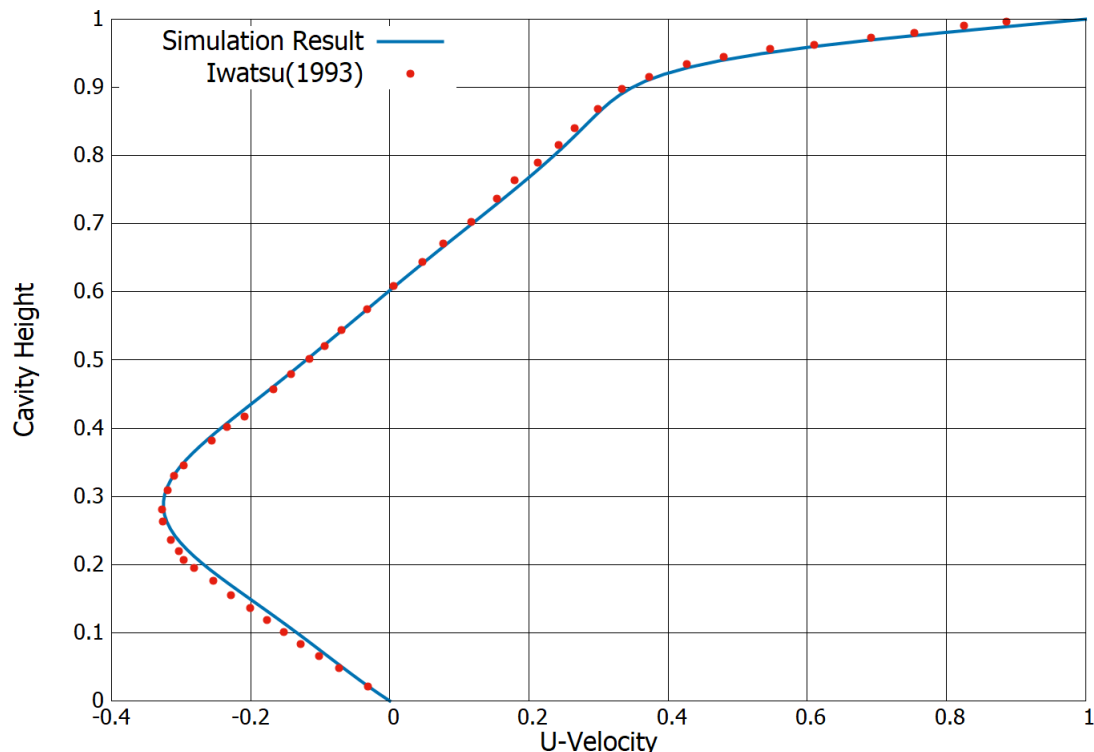


Figure 3.19: Reynolds Number =400

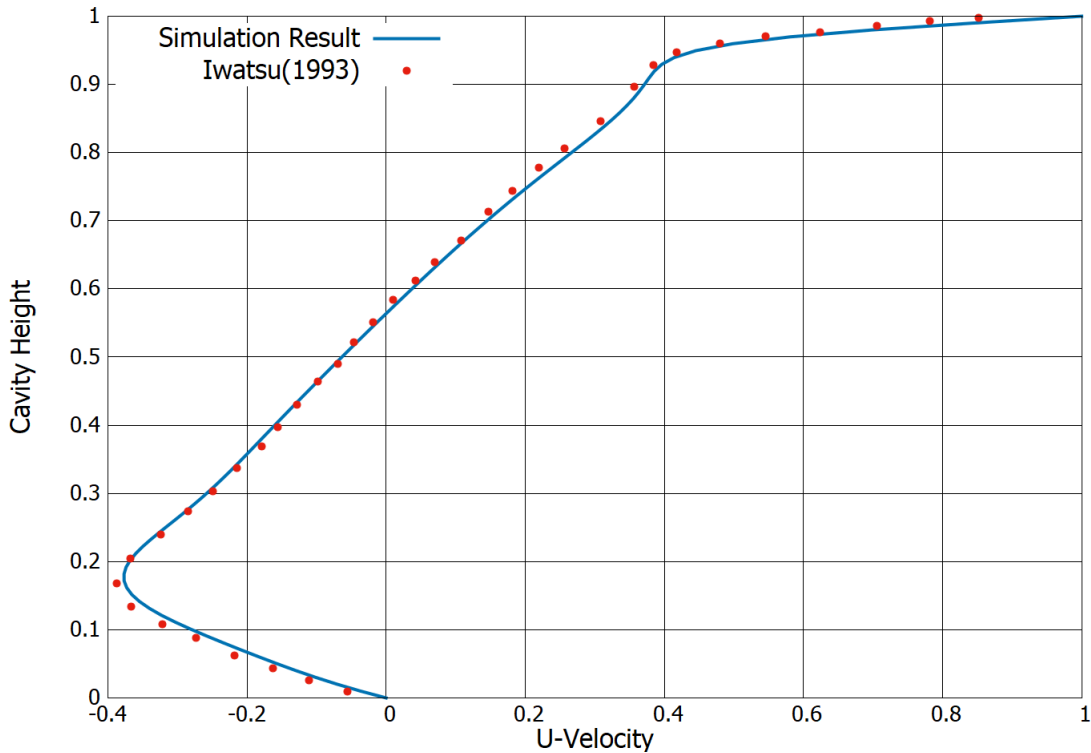


Figure 3.20: Reynolds Number =1000

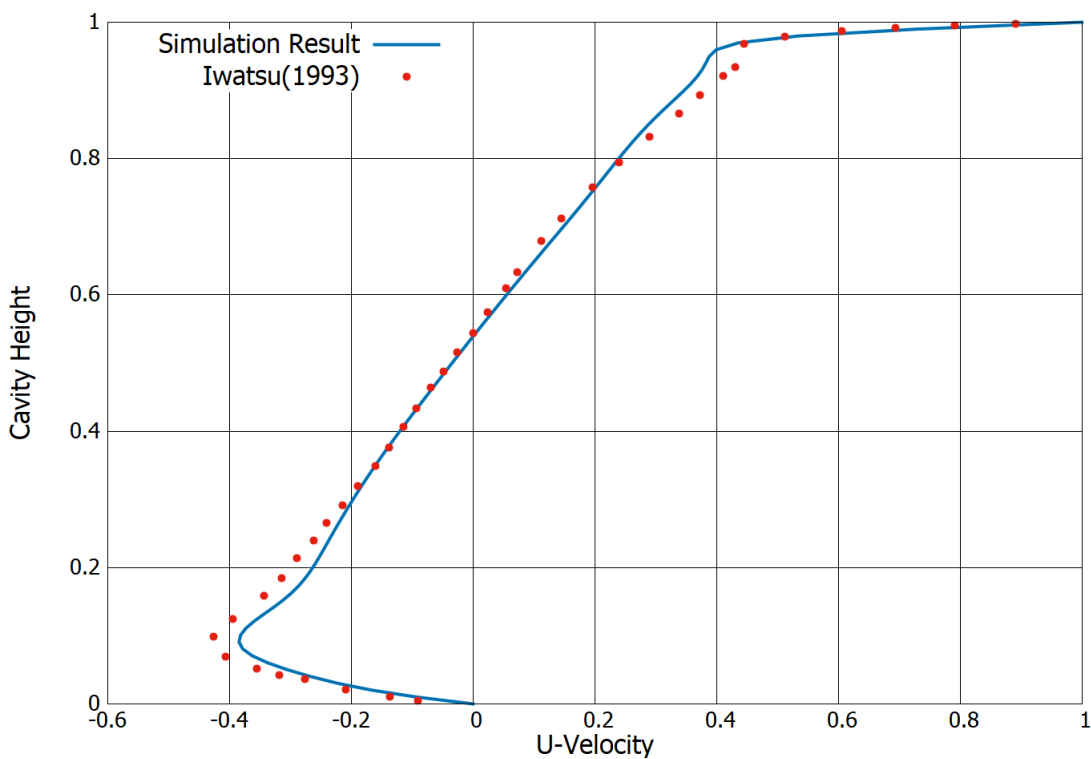


Figure 3.21: Reynolds Number =3000

CHAPTER 4

Turbulence modelling for Magnetohydrodynamics and Mixed convection flow

4.1 Introduction

The study has been extended to include the high Reynolds number flows of both magnetohydrodynamics and mixed convection. For the high Reynolds numbers, turbulence models are utilized to account for the turbulent behaviour of the fluid. The study is conducted by creating a new OpenFOAM solver which combines both Lorentz force and buoyancy force (modelled using the Boussinesq approximation) in the Navier-Stokes equation. The K-Epsilon turbulence model is used which is a standard OpenFOAM turbulence model for the Reynolds-Averaged Navier-Stokes equation (RAS). The solver is tested in three stages of validation - the first is for pure turbulent fluid flow with Prasad and Koseff(1989)[16], next turbulent natural convection with Markatos[12] and pure MHD with Kefayati(2014) [10].

4.1.1 K-Epsilon turbulence model

The Reynolds approach to modelling turbulence is to split the three velocity components into a steady term and a fluctuating term(Eq. 4.1). The steady component is the time-averaged component and the time averaging of the fluctuating component is assumed to be equal to zero.

$$U = \bar{U} + U' \quad (4.1)$$

This results in the Reynolds-Averaged Navier Stokes equation (RAS) (written in compressible form) in Eqn 4.2

$$\frac{\partial(\rho U)}{\partial t} + \nabla \cdot (\rho U U) = -\nabla p + \nabla \cdot [\mu(\nabla U + (\nabla U)^T)] + \rho g - \nabla \left(\frac{2}{3} \mu (\nabla \cdot U) \right) - \nabla \cdot (\rho \bar{U'U'}) \quad (4.2)$$

The final term is the Reynolds Stress which is the divergence of the product of the two fluctuation velocity components which have been averaged. The K-Epsilon model computes the mean velocity components and in order to do so the Reynolds stress term needs to be modelled.

The Boussinesq hypothesis calculates the Reynolds stress using the gradients of the mean velocity components and turbulent viscosity(μ_t). Therefore the K-Epsilon model is one approach to calculate the turbulent viscosity to close the equations. The turbulent viscosity is calculated algebraically (Eqs .4.3 and 4.5) using the turbulent kinetic energy (k) and turbulent dissipation rate (ϵ). Therefore a transport equation (Eq. 4.4) is solved to compute the two quantities.

$$\mu_t = C_\mu \frac{\rho k^2}{\epsilon} \quad (4.3)$$

$$\frac{\partial(\rho k)}{\partial t} + \nabla \cdot (\rho U k) = \nabla \cdot [(\mu + \frac{\mu_t}{\sigma_k}) \nabla k] + Sources + Sinks \quad (4.4)$$

$$\frac{\partial(\rho \epsilon)}{\partial t} + \nabla \cdot (\rho U \epsilon) = \nabla \cdot [(\mu + \frac{\mu_t}{\sigma_\epsilon}) \nabla \epsilon] + Sources + Sinks \quad (4.5)$$

Five model coefficients are used for the $k - \epsilon$ model. The values used in standard OpenFOAM solver are:

Constant	Value
C_μ	0.09
C1	1.44
C2	1.92
C3	0.0
σ_k	1.0
σ_ϵ	1.3

Figure 4.1: Turbulence model constants

4.1.2 Turbulent Heat Transfer

The thermal diffusivity for turbulent flow is computed by adding a second component to the laminar thermal diffusivity (Eq .4.6). This component is the ratio of the turbulent viscosity and the turbulent Prandtl number.

$$\alpha_{effective} = \alpha_{Laminar} + \frac{\mu_t}{Pr_t} \quad (4.6)$$

where ,

μ_t - Turbulent Viscosity

Pr_t - Turbulent Prandtl number (0.9 for air).

The non-dimensional heat transfer coefficient “Nusselt Number” is also included in the validation and analysis.

4.1.3 Solver

A steady state solver is created which computes the mean velocity components along with the magnetic field and temperature field. Two extra forces - Lorentz force and Buoyancy force are added to the momentum equations. The Boussinesq hypothesis is further utilized for computing the buoyancy force. A separate post-processing code was used for computing the Nusselt number and wall heat flux.

4.2 Case Setup

The $k - \epsilon$ model in OpenFOAM requires the values of k, ϵ and μ_t to be supplied as boundary conditions. These values are computed using the constants using the following equations based on initial velocity.

$$k = \frac{3}{2}(U_{ref} * I)^2 \quad (4.7)$$

$$\epsilon = \frac{C_\mu^{0.75} * k^{1.5}}{l} \quad (4.8)$$

$$\mu_t = C_\mu \frac{k^2}{\epsilon} \quad (4.9)$$

where ,

I :- turbulence intensity

U_{ref} :- Lid Velocity

l :- length of lid * turbulence intensity

4.3 Validation

4.3.1 Fluid Flow

The turbulent fluid flow with no external magnetic field and buoyancy force is analysed for a cubic cavity with a 30x30x30 grid. Results for Reynolds number of 3200 and 10000 are compared with Prasad and Koseff(1989)[16]. The lid velocity has been taken as 1 m/s and the standard wall functions are used for k , ϵ and μ_t .

Boundary Conditions :

1. Top Wall : $U = (1 \ 0 \ 0)$, $T =$

2. Bottom Wall : $U = \text{noSlip}$

3. Left Wall : $U = \text{noSlip}$

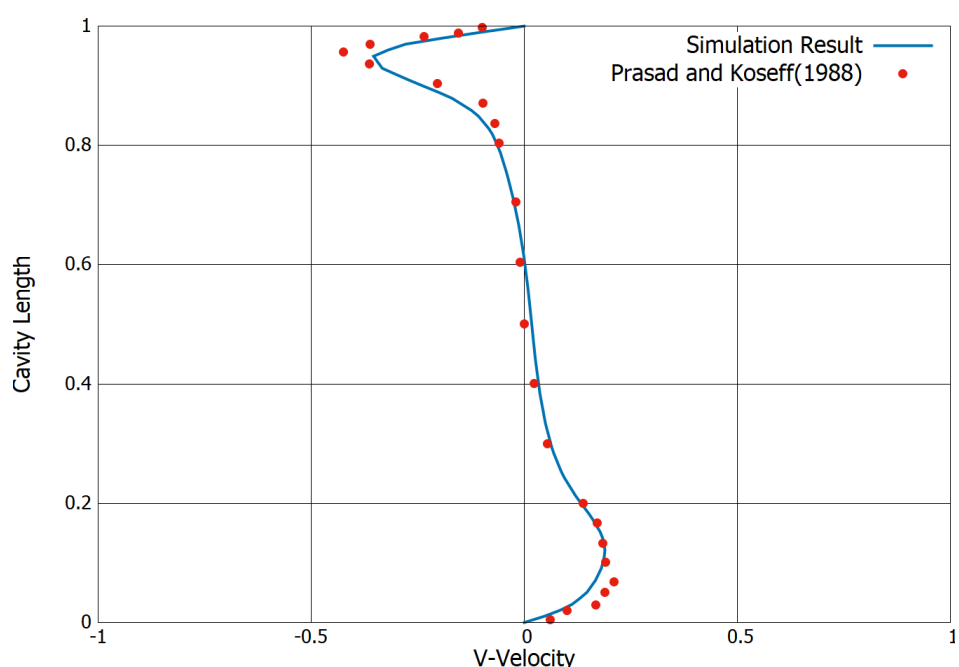
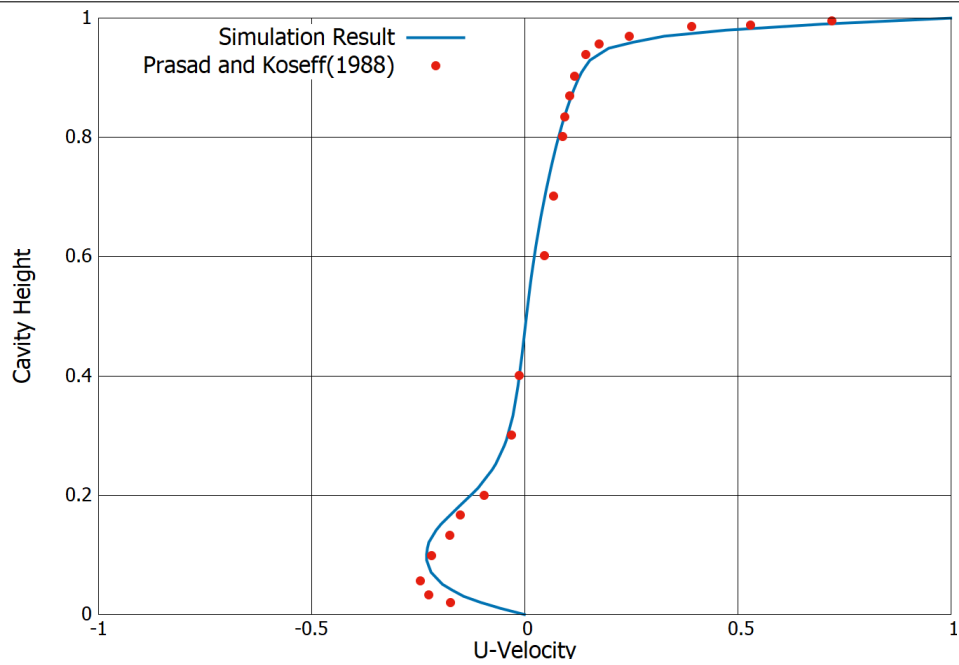
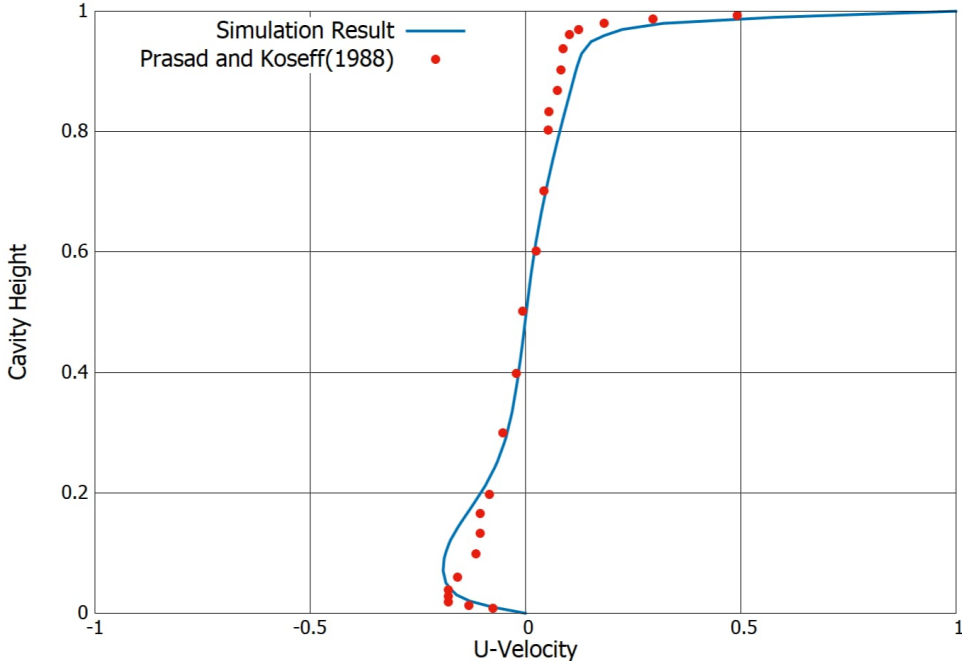
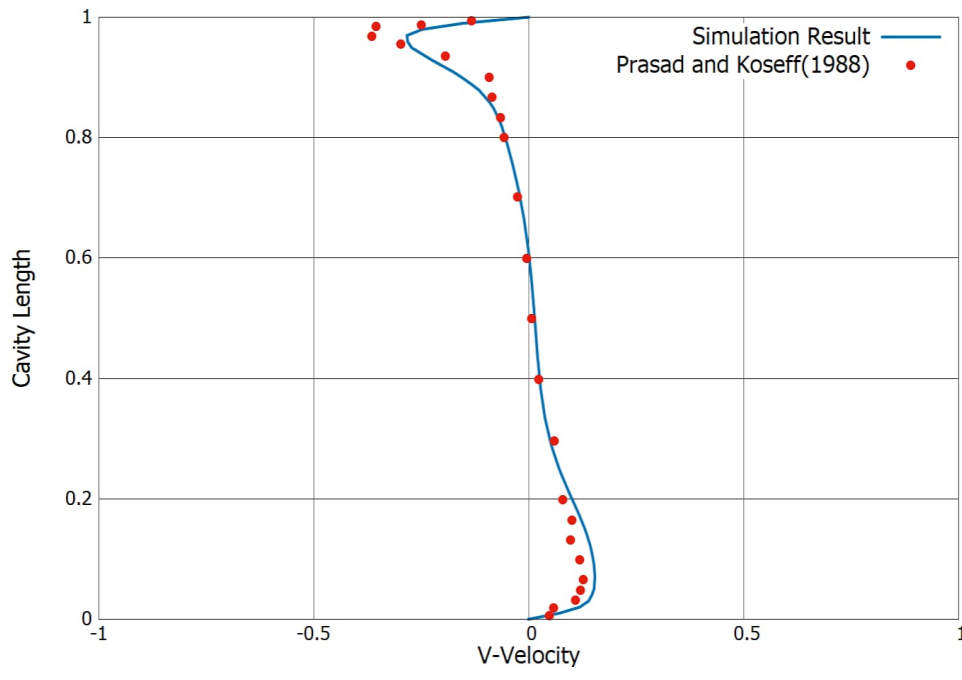


Figure 4.2: Reynolds Number =3200



(a) Comparison of U-Velocity along the vertical mid of the XY Plane



(b) Comparison of V-Velocity along the vertical mid of the XY Plane

Figure 4.3: Reynolds Number =10000

4.3.2 Turbulent Heat Transfer

The validation of the natural convection flow with $k - \varepsilon$ model was done using Markatos(1984)[12]. The turbulent cases are considered for Rayleigh numbers of $1e6$ and greater. The top velocity is given as zero since the case is for natural convection, however the U_{ref} is computed as given below and is used in Eqns

4.7,4.8,4.9 to compute the initial values of the three turbulent variables.

$$U_{ref} = \sqrt{(g\beta\Delta TH)} = \sqrt{\frac{Ra * nu * nu}{Pr}} \quad (4.10)$$

The initial validation study consisted of a velocity comparison for Rayleigh number of 1e6.

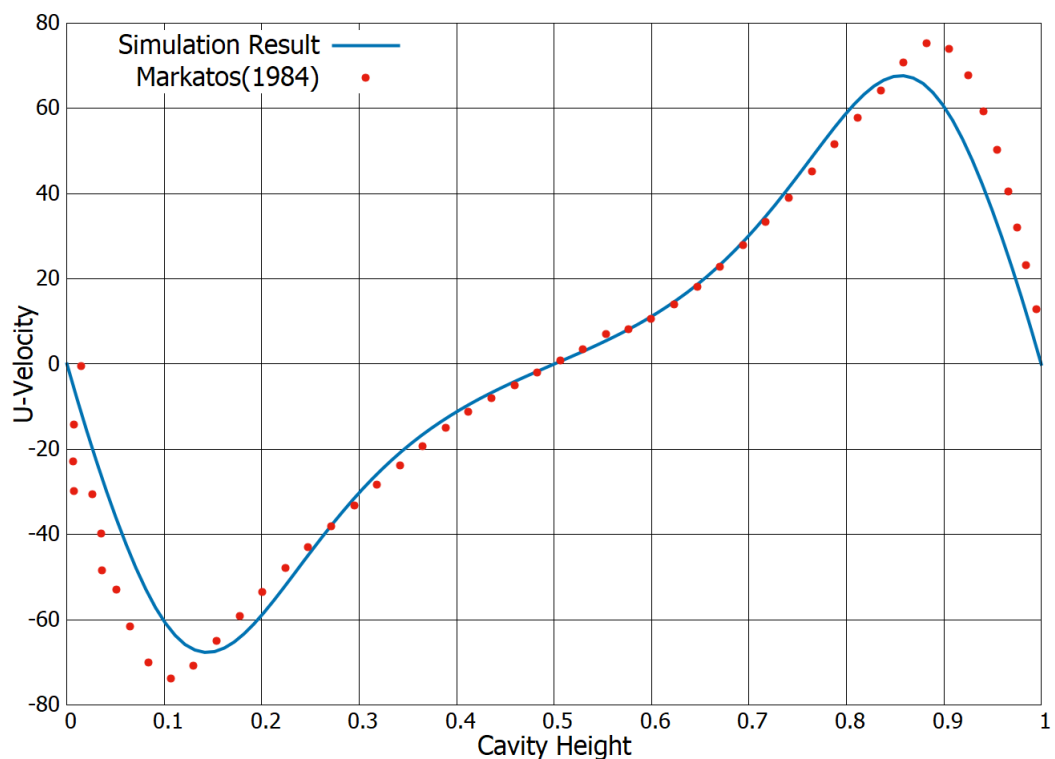


Figure 4.4: Comparison of U-Velocity along the vertical mid-line of the cavity

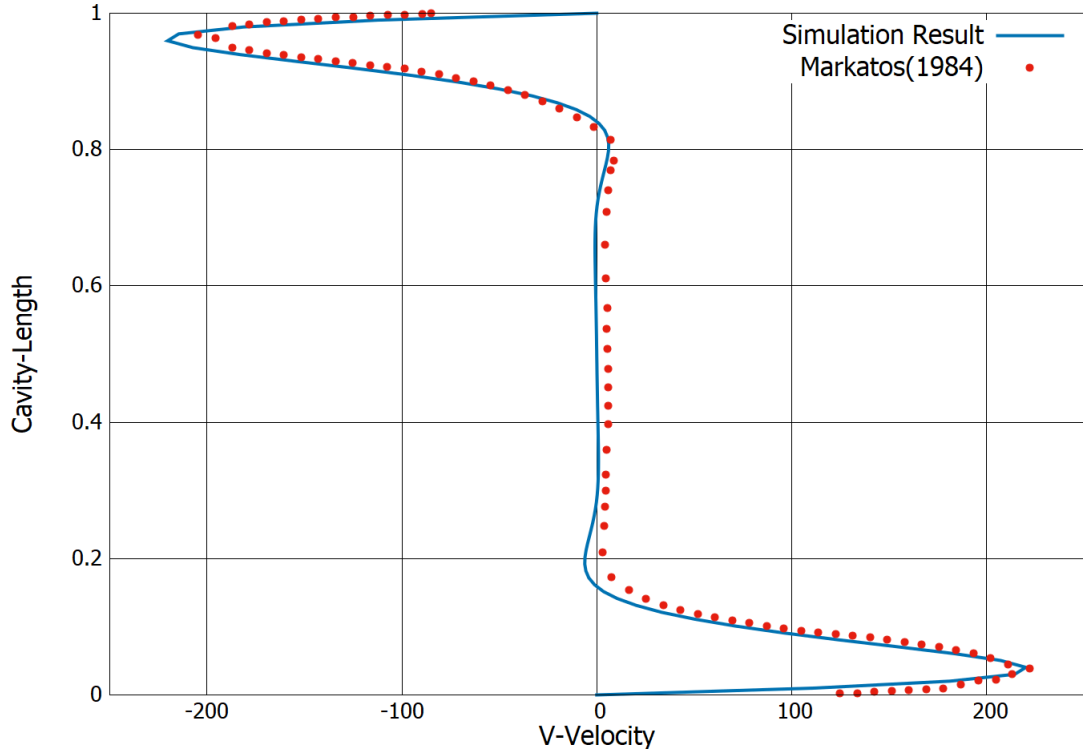


Figure 4.5: Comparison of V-Velocity along the horizontal mid-line of the cavity

The validation is extended for Rayleigh numbers of 1e6, 1e8, 1e10 and consists of the maximum of U-velocity along the vertical mid-line and the maximum value of V-velocity along the horizontal mid-line.

	Rayleigh Number	1e6	1e8	1e10
Vmax along y=0.5	Simulation	220.247	2118.08	17492.0
	Markatos(1984)	221.8	1812	16890
Umax along y=0.5	Simulation	67.673	513.359	2950.94
	Markatos(1984)	68.81	514.3	2323

Figure 4.6: Comparison with Markatos(1984)

The non-dimensional Nusselt number is computed at the left wall (hot wall) using the wall-heat flux which is in-turn computed using wall functions available in OpenFOAM. The Nusselt number is computed using the formula(Eqn.4.11)

$$Nu(y) = \left(\frac{\dot{q}_{wall}}{\alpha C_p \rho} \right) * \left(\frac{D}{T_H - T_C} \right) \quad (4.11)$$

where,

\dot{q}_{wall} - Wall Heat Flux

α - Thermal Diffusivity

C_p - Specific Heat Capacity of air (1005 J/g/K)

D - Length of the cavity

T_H, T_C - Hot and cold wall temperatures

	Rayleigh Number	1e6	1e8	1e10
Nu_{max}	Simulation Result	17.7414	85.86843	376.8212
	Markatos(1984)	17.872	61.06	361.47
Nu_{avg}	Simulation Result	8.9833	35.0473	160.1477
	Markatos(1984)	8.754	32.045	156.85
Nu_{min}	Simulation Result	1.1172	3.52825	16.7126
	Markatos(1984)	1.232	5.2246	23.462

Figure 4.7: Comparison of Nusselt Number with Markatos(1984)

4.3.3 Magnetohydrodynamics

The new steady state solver is tested for its MHD performance with published data in Kefayati(2014)[10]. Due to the unavailability of turbulent MHD data, the turbulence in the solver was turned off. This section of validation is to test the working of the steady state MHD solver . The Hartmann number is considered in this case are two extreme values of 10 and 100 are used in conjunction with Reynolds numbers of 100 and 1000.

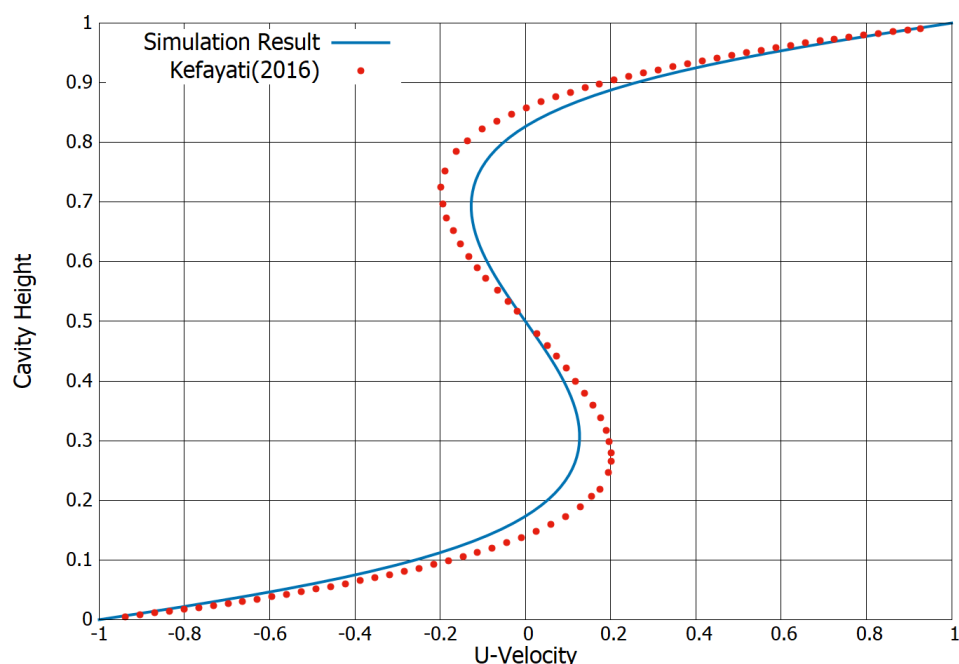


Figure 4.8: Reynolds Number=100, Hartmann Number =10

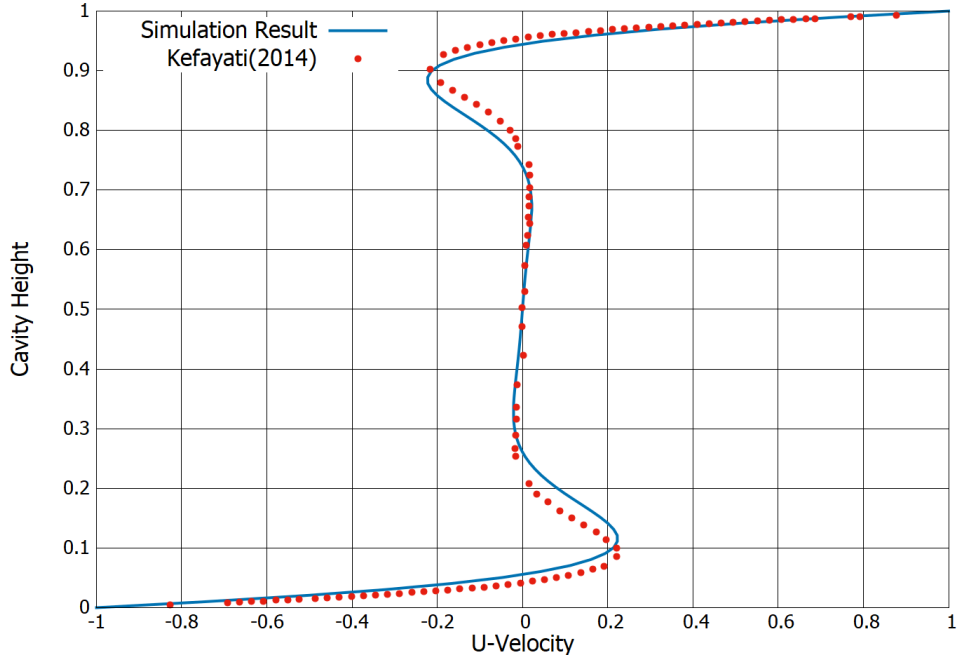


Figure 4.9: Reynolds Number=1000, Hartmann Number =100

4.4 Mathematical Formulation

4.4.1 Governing Equations

The standard incompressible Navier-Stokes equation with added Lorentz force and buoyancy force is solved in this study to compute the velocity.

$$\nabla \cdot V = 0 \quad (4.12)$$

$$\frac{\partial u}{\partial t} + V \cdot \nabla u = -\nabla p + Pr \nabla^2 u + ((\vec{B} \cdot \nabla) \vec{B} / \mu_o) - (\nabla B^2 / (2 * \mu_o)) \quad (4.13)$$

$$\frac{\partial v}{\partial t} + V \cdot \nabla v = -\nabla p + Pr \nabla^2 v + Ra Pr T + ((\vec{B} \cdot \nabla) \vec{B} / \mu_o) - (\nabla B^2 / (2 * \mu_o)) \quad (4.14)$$

The two additional terms in 4.13,4.14 are the magnetic pressure and magnetic tension. In eqn 4.14 the additional term is for the buoyancy force which acts in the vertical direction. These three equations are presented in the laminar form , however they are modified for the turbulent behavior according to the $K - \epsilon$ model (Eqn 4.2)

Three additional equations are solved for the two additional variables , namely Magnetic Field (B) and Temperature (T).

The first two are the magnetic induction equation (transport equation) and the magnetic continuity equation (Gauss's law of Magnetism).

The linear transport equation for temperature is the fourth governing equation.

$$\frac{\partial T}{\partial t} + V \cdot \nabla T = \nabla^2 T \quad (4.15)$$

It must be noted that for turbulent fluid flow $\alpha_{effective}$ is used in the place of the laminar analogue.(Eqn. 4.16)

$$\alpha_{effective} = \alpha_{Laminar} + \frac{\mu_t}{Pr_t} \quad (4.16)$$

where ,

μ_t - Turbulent Viscosity

Pr_t - Turbulent Prandtl number (0.9 for air).

Since the study is focused on a square cavity with constant wall-temperature and a RANS formulation is used the Jischa and Rieke model is used for computing Pr_t [11]. The Jischa and Rieke model described in [6] calculates the turbulent Prandtl number based on laminar Prandtl number and Reynolds number (Eqn.4.17).

$$Pr_t = 0.9 + \frac{182.4}{PrRe^{0.888}} \quad (4.17)$$

4.4.2 Boundary Conditions and Cases

	Velocity	Temperature	Magnetic Field
Top Wall	(V,0,0)	zeroGradient	zeroGradient
Right Wall	noSlip	0.0	zeroGradient
Left Wall	noSlip	1.0	zeroGradient
Bottom Wall	(-V,0,0)	zeroGradient	zeroGradient

Figure 4.10: Boundary Conditions for Velocity , Temperature and Magnetic Field

The domain is the 2D square cavity with the top wall given a positive x-direction velocity and the bottom given the same magnitude velocity in the negative x-direction. The top and bottom walls are assumed to be adiabatic and the left and right are given constant temperatures. All walls are perfectly conducting the domain in given an initial magnetic field to the positive x-direction (no vertical component).

The three variations examined in this study include the variation due to Prandtl number , Reynolds number and Hartmann number. The fluid used is the human blood. The Prandtl number used are 0.71 , 3 , 7 these three values cover the range of Prandtl number observed for human blood and water. Further, in order to understand the effect of magnetic field and inertial forces on heat transfer the Hartmann numbers used are 0 , 25 and 50, and the Reynolds numbers used are 1000 , 5000 and 10000 (laminar and turbulent). The main parameter used to judge the heat transfer characteristics is the Nusselt number (averaged over the wall) which is computed for the left or the warm wall based on the heat flux. (Eqn.4.11).

4.5 Results

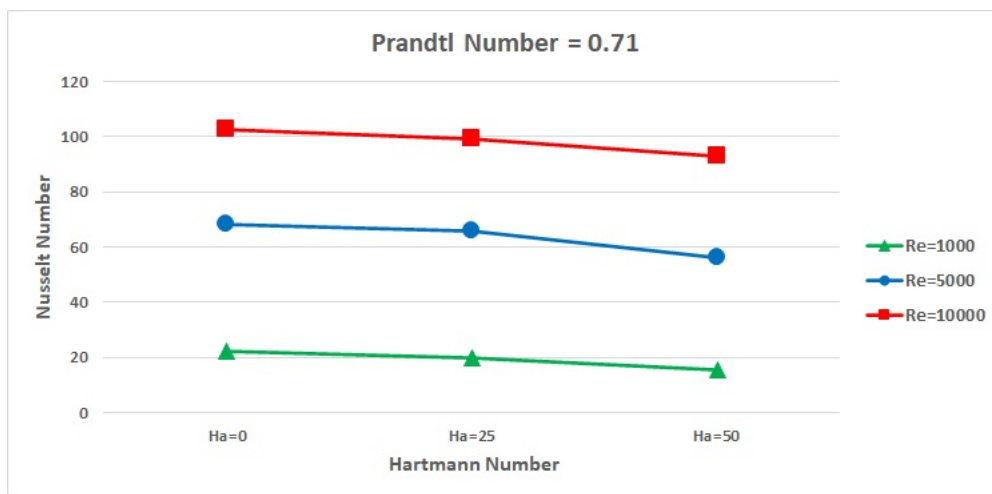


Figure 4.11: Variation of average Nusselt Number for Prandtl Number of 0.71

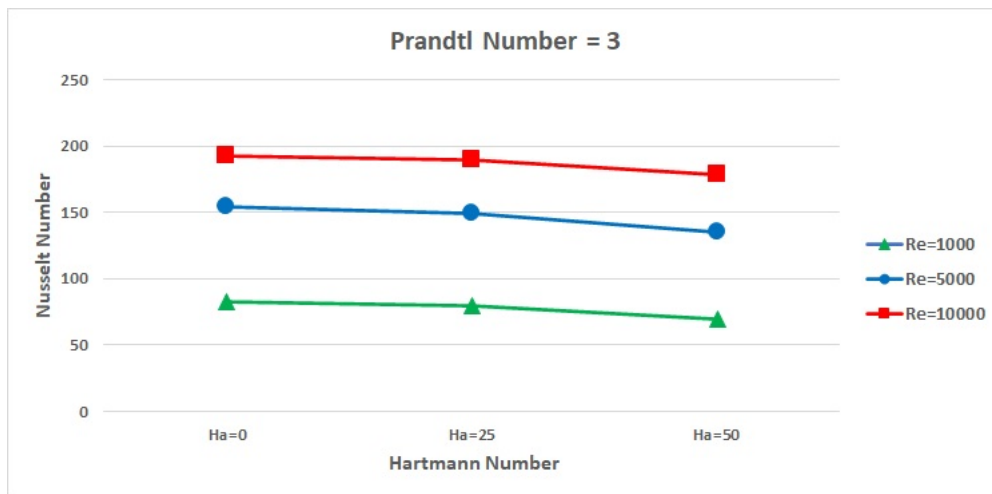


Figure 4.12: Variation of average Nusselt Number for Prandtl Number of 3

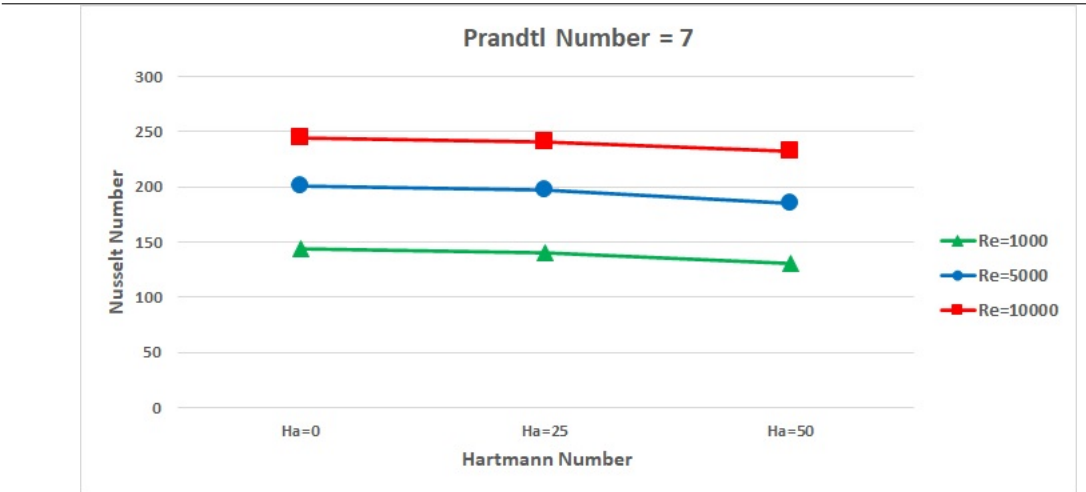


Figure 4.13: Variation of average Nusselt Number for Prandtl Number of 7

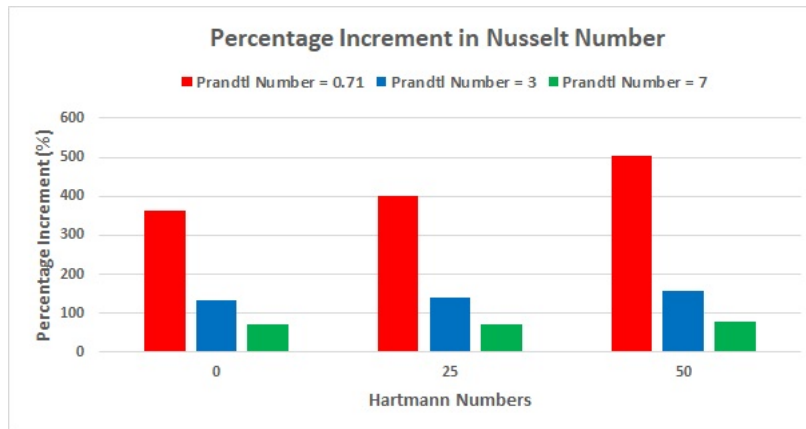


Figure 4.14: Increment in Nusselt number with increasing Reynolds number

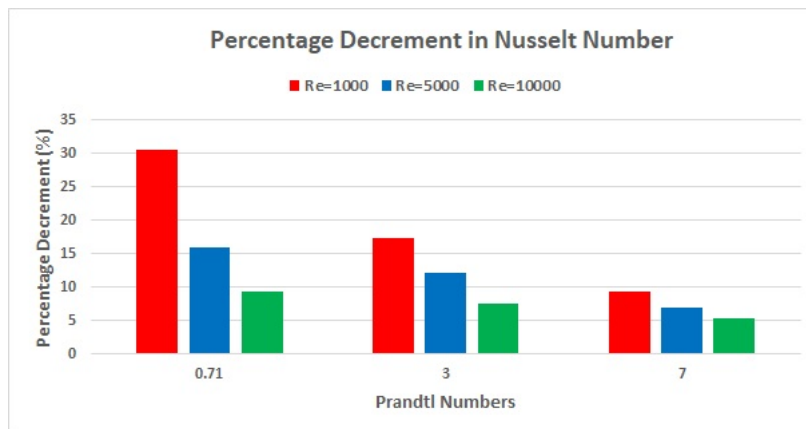


Figure 4.15: Decrement in Nusselt number with increasing Hartmann number

4.5.1 Prandtl Number = 0.71

4.5.1.1 Reynolds Number = 1000

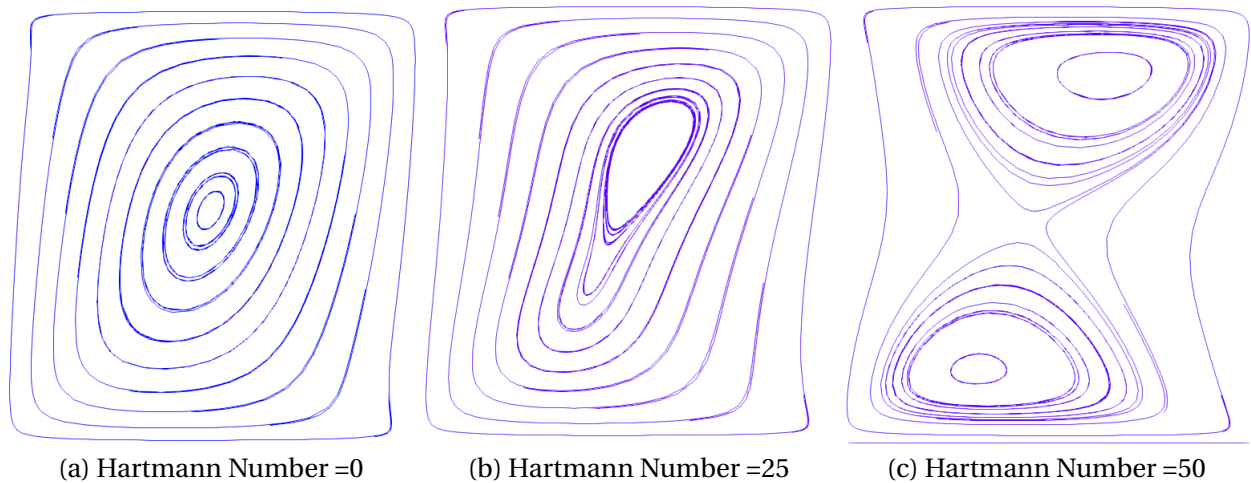


Figure 4.16: Streamlines

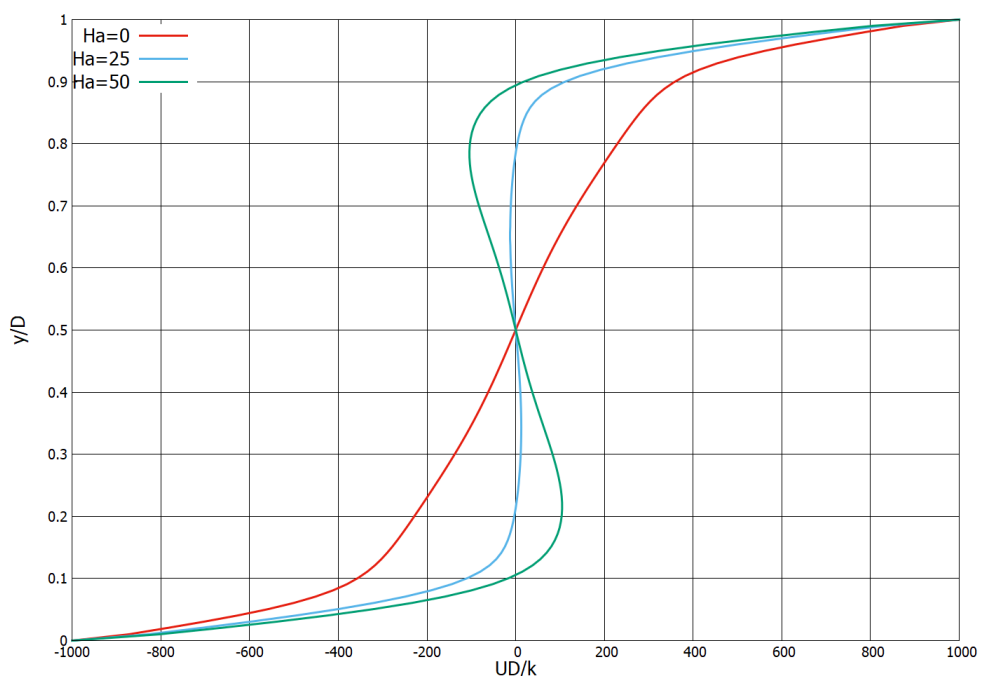


Figure 4.17: U-Velocity along cavity height

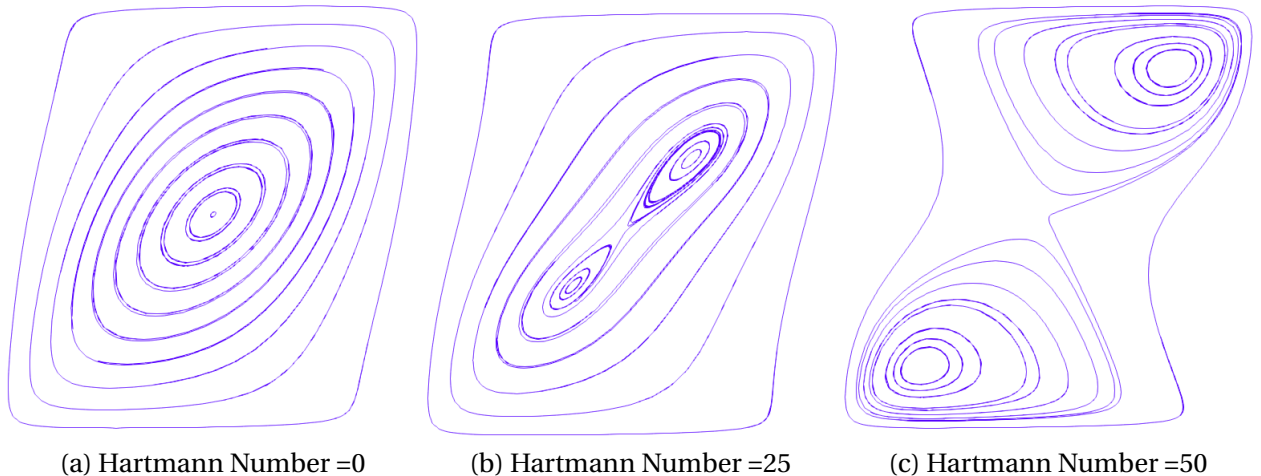
4.5.1.2 Reynolds Number = 5000

Figure 4.18: Streamlines

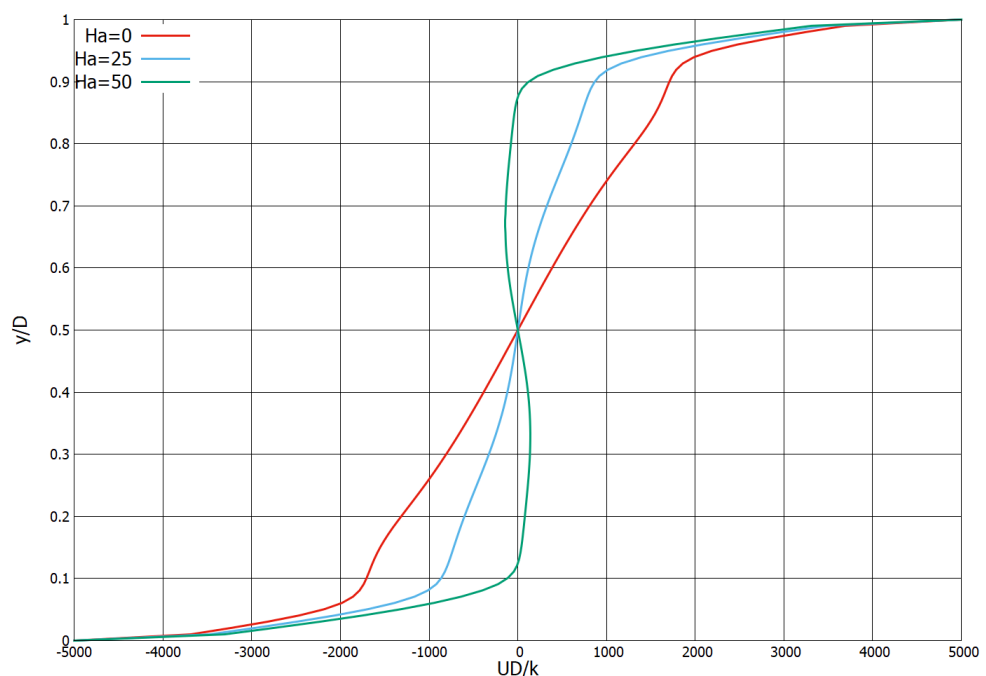


Figure 4.19: U-Velocity along cavity height

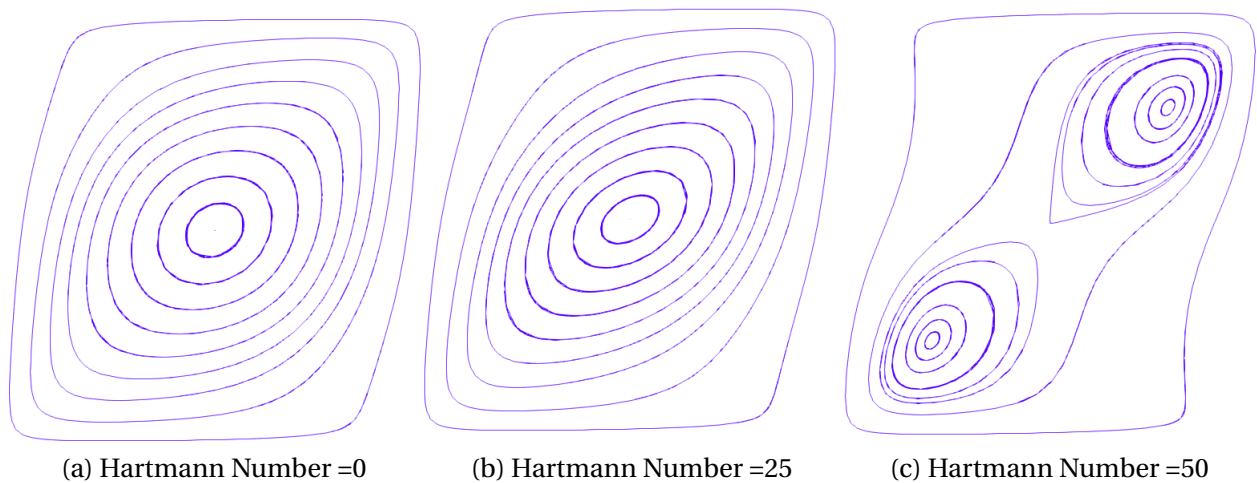
4.5.1.3 Reynolds Number = 10000

Figure 4.20: Streamlines

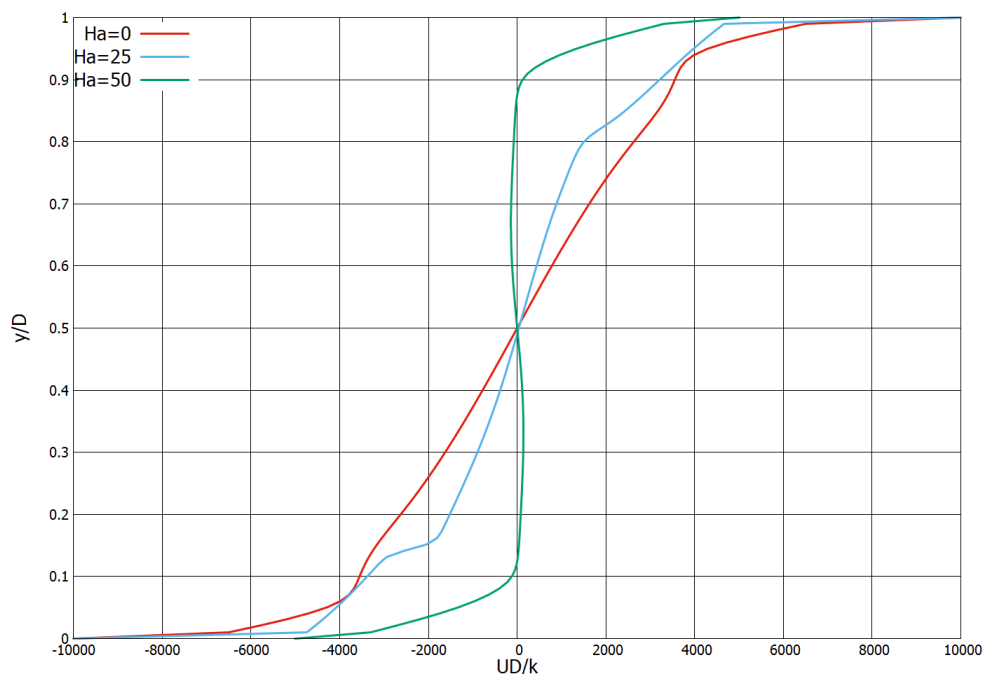


Figure 4.21: U-Velocity along cavity height

4.5.2 Prandtl Number = 3

4.5.2.1 Reynolds Number = 1000

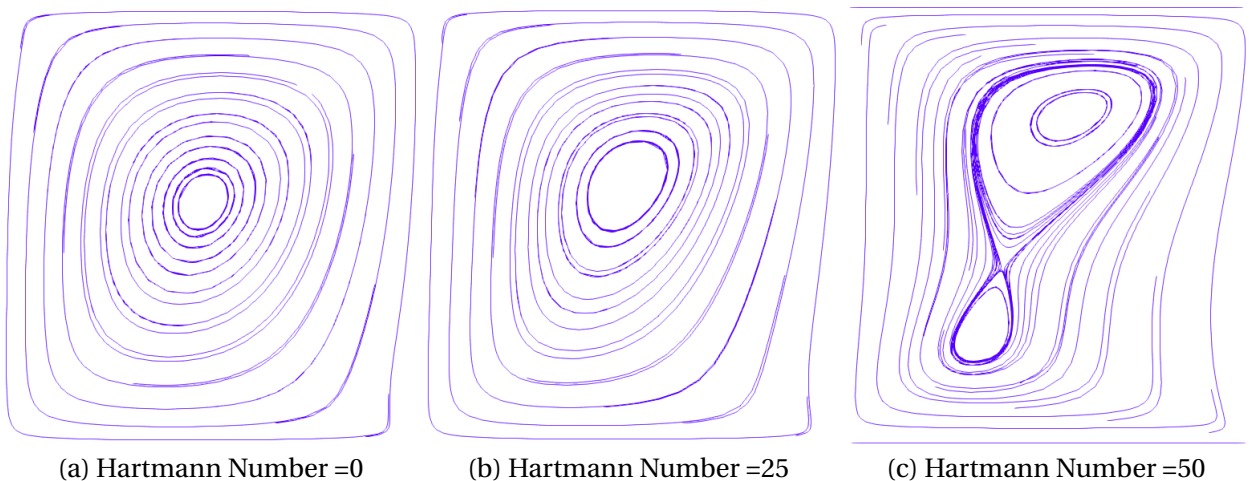


Figure 4.22: Streamlines

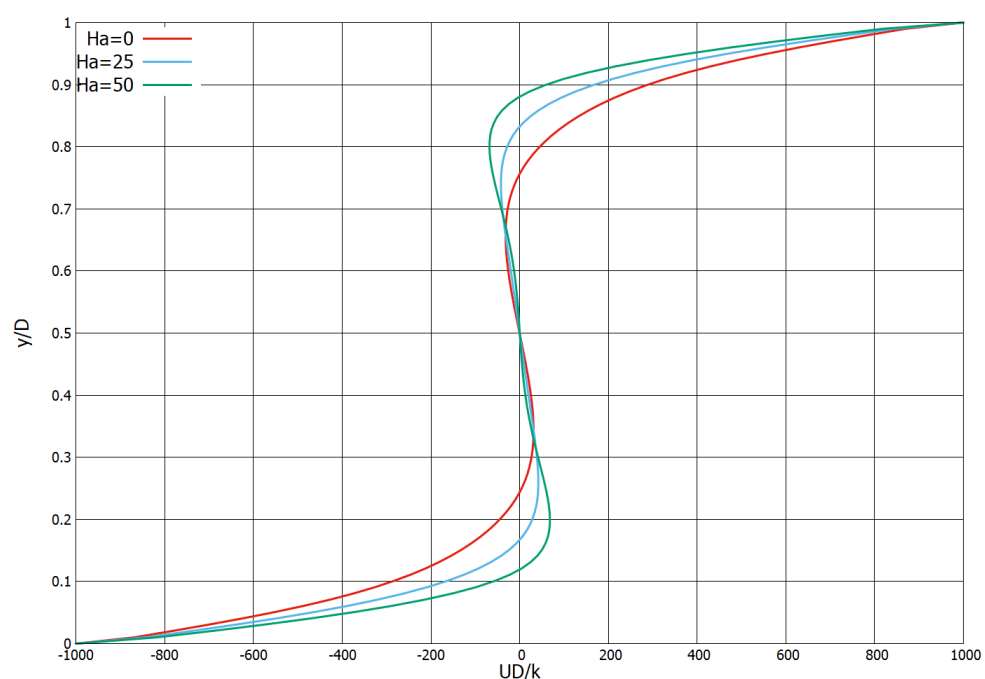


Figure 4.23: U-Velocity along cavity height

4.5.2.2 Reynolds Number = 5000

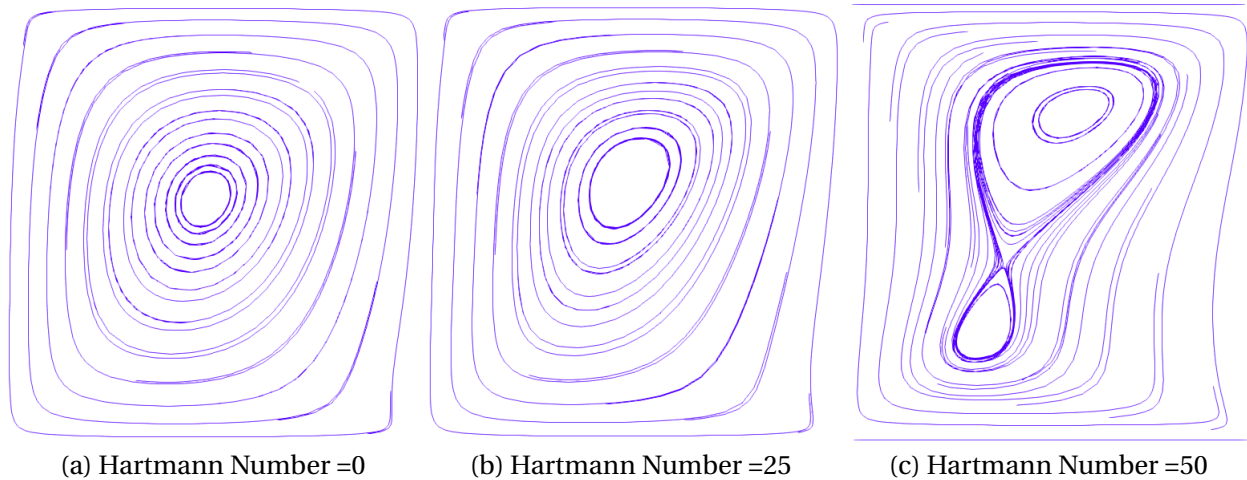


Figure 4.24: Streamlines

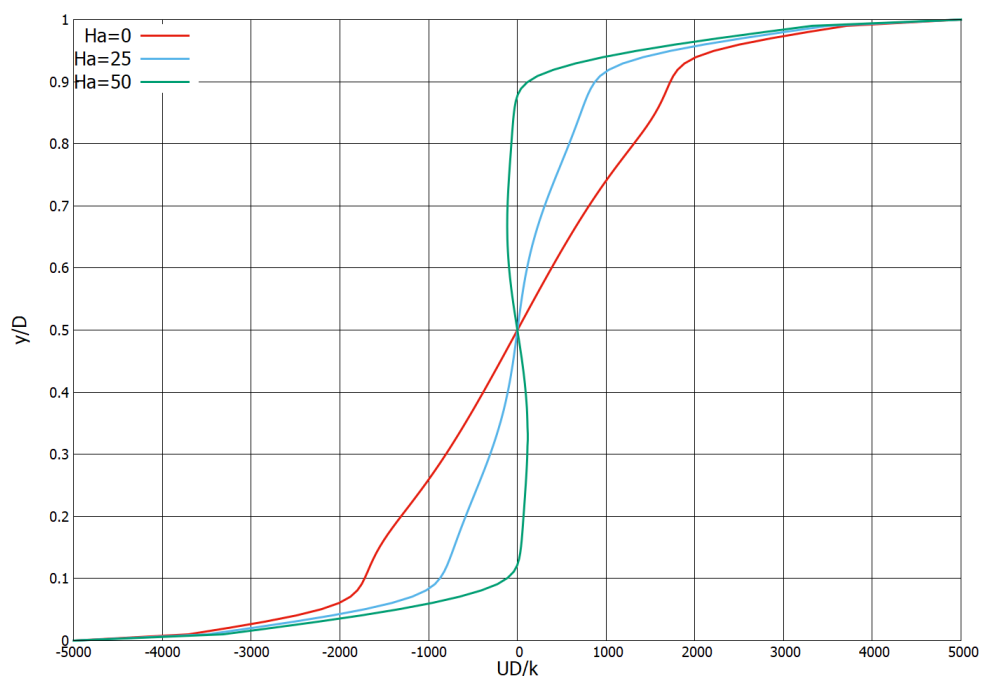


Figure 4.25: U-Velocity along cavity height

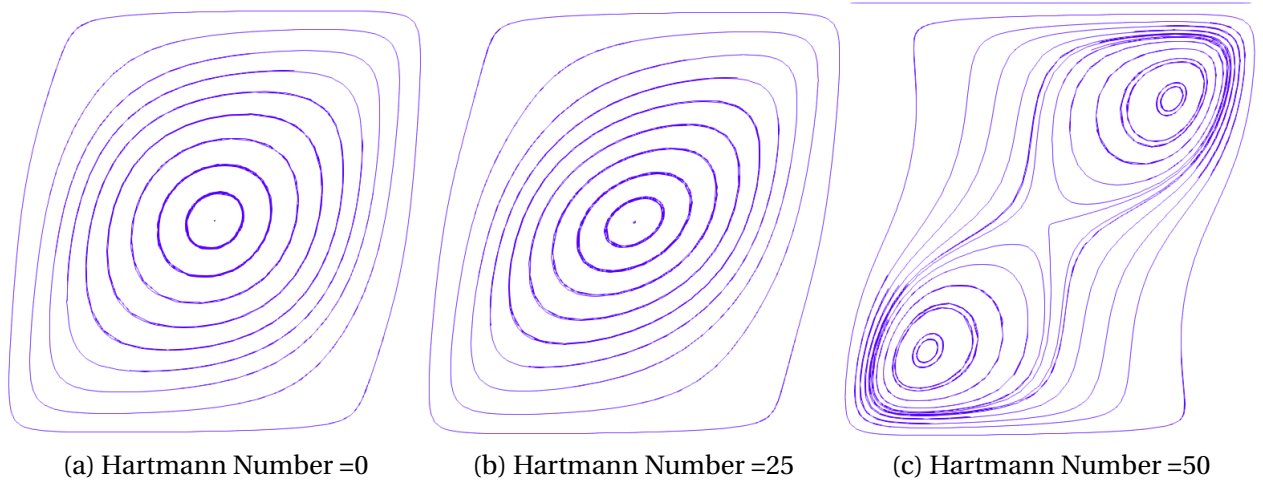
4.5.2.3 Reynolds Number = 10000

Figure 4.26: Streamlines

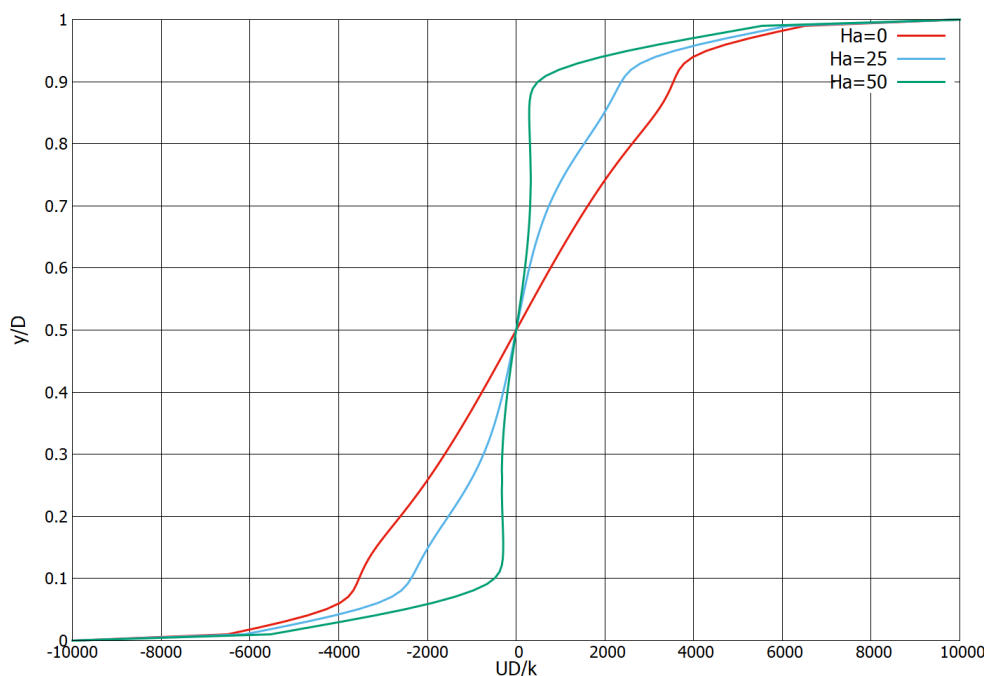


Figure 4.27: U-Velocity along cavity height

4.5.3 Prandtl Number = 7

4.5.3.1 Reynolds Number = 1000

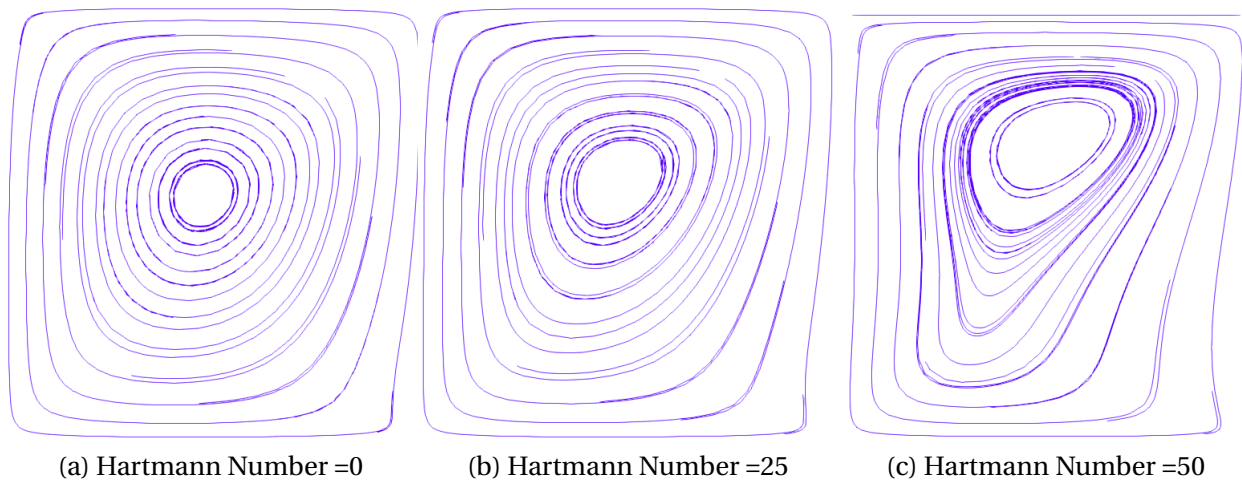


Figure 4.28: Streamlines

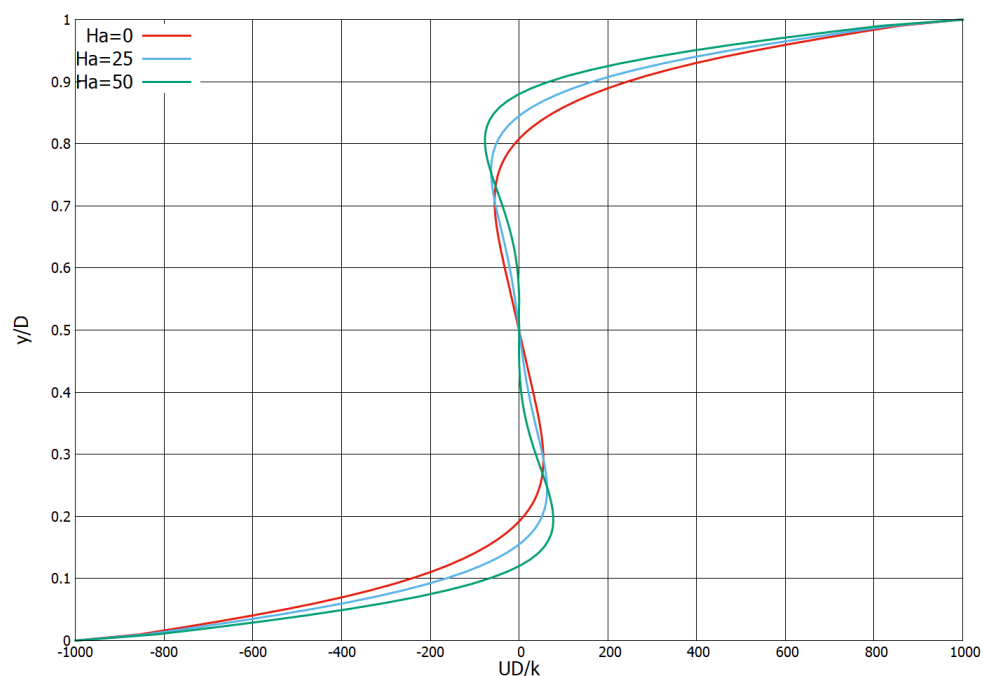


Figure 4.29: U-Velocity along cavity height

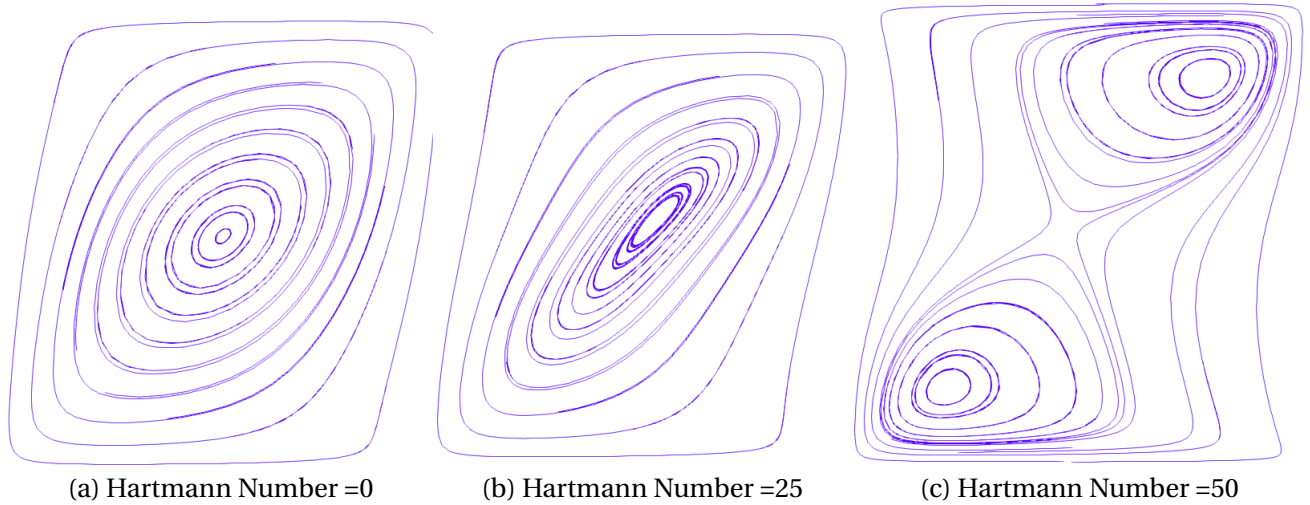
4.5.3.2 Reynolds Number = 5000

Figure 4.30: Streamlines

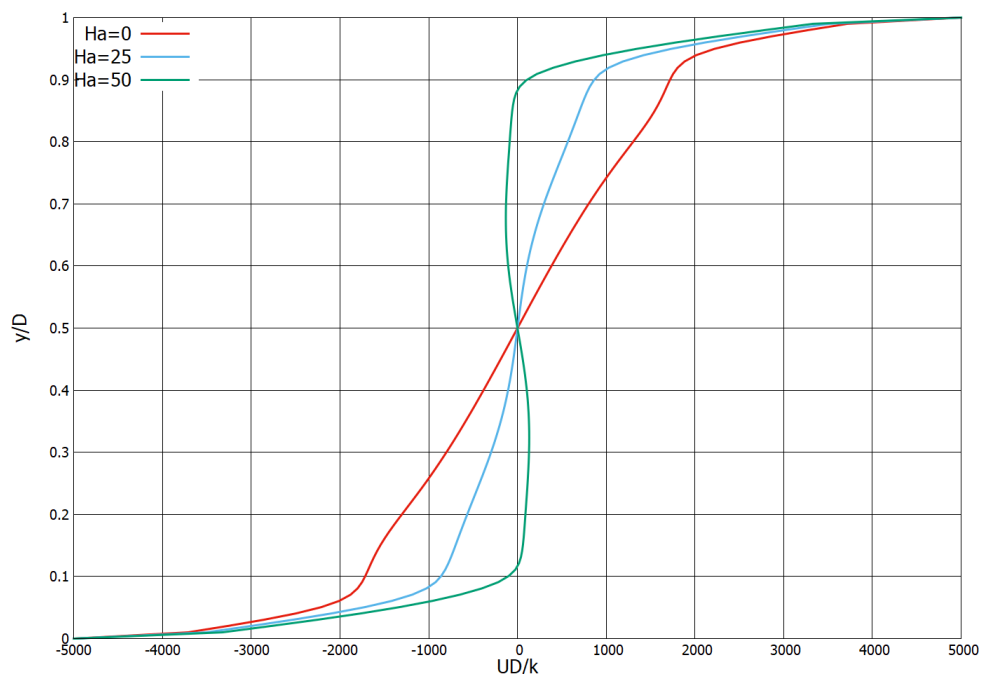


Figure 4.31: U-Velocity along cavity height

4.5.3.3 Reynolds Number = 10000

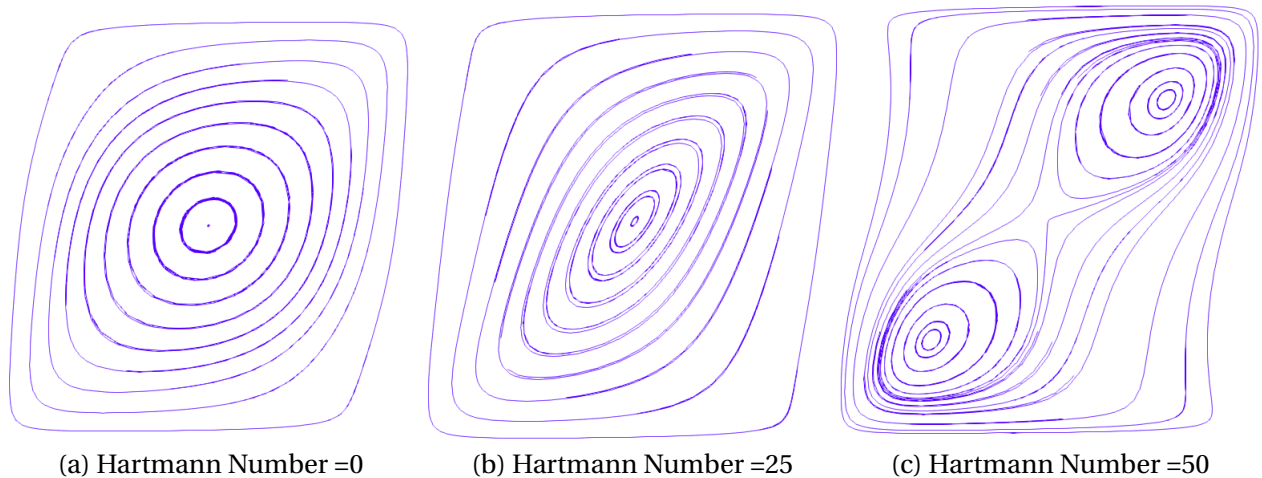


Figure 4.32: Streamlines

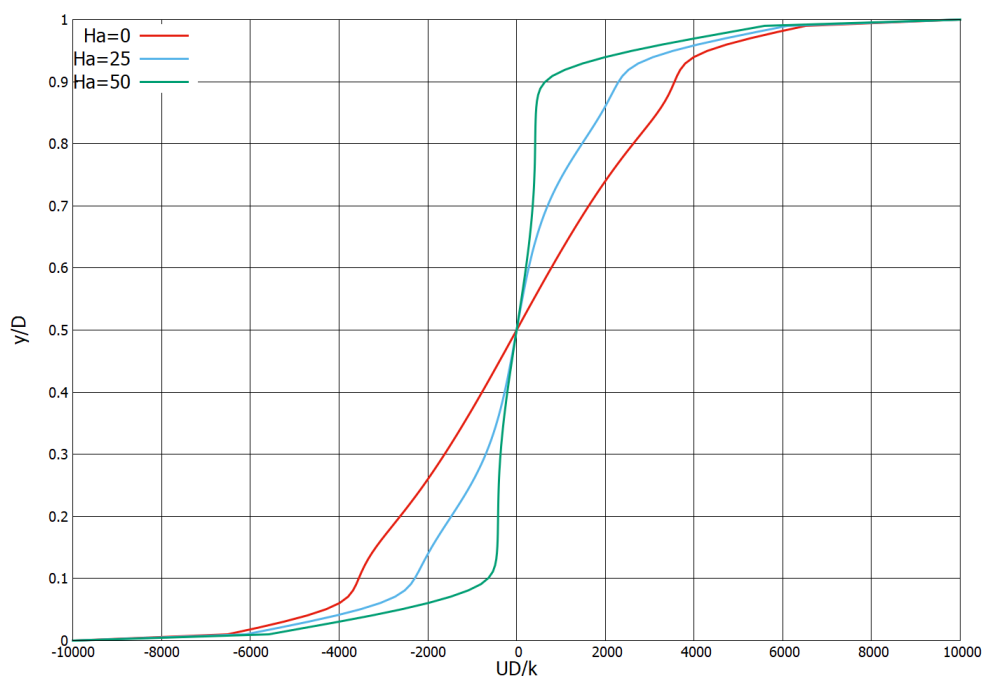


Figure 4.33: U-Velocity along cavity height

4.6 Discussion

The results indicate that the Nusselt number decreases with an increase in Hartmann number (or increasing magnetic field intensity) (Figures 4.11,4.12,4.13) for a fixed Reynolds number and Prandtl number. From analysis of the streamlines (Figure 4.16) it is evident that the effect of increasing magnetic field is to split the core clockwise vortex into two vortices. This results in loss of the strength of the core vortex. This is further substantiated by the U-Velocity graph (Figure 4.17) which shows that higher Hartmann number plots move closer to the zero line and go beyond it. With the hot wall being to the left, the heated fluid would rise near the left side and fall near the right side (cold wall) setting up a clockwise vortex which is further supported by the motion of the top and bottom walls. The decrease in Nusselt number can therefore be directly linked to the strength of core vortex which is lower for higher Hartmann numbers.

Figure 4.15 shows that the decrease in Nusselt number is substantially higher for lower Reynolds and Prandtl numbers - this result was expected given that the U-Velocity graphs (Figures 4.17,4.19,4.21,4.23,4.25,4.27,4.29,4.31,4.33) show that the difference between the 0 Hartmann number and 50 Hartmann number plots are lower for higher Reynolds numbers. Figure 4.17 shows a large difference for the lowest Prandtl number (0.71) and lowest Reynolds number (1000) which results in the largest decrease in Nusselt number (Figure 4.15) for this case.

Figure 4.14 further shows that the Nusselt number increases with increase in Reynolds number, the reason behind this is that with a higher top and bottom wall velocity the core clockwise vortex increases in strength aiding the heat transfer. Furthermore, this increase is higher for low Prandtl numbers. This result is due to the interplay of the buoyancy and inertial forces. With a lower Prandtl number the buoyancy force is reduced which causes a higher effect of the increment of the inertial forces. In addition, by comparing the green line representing Hartmann number=50 in Figures(4.17,4.21) for $Pr=0.71$, Figures(4.23,4.27) for $Pr=3$ and Figures(4.29,4.33) for $Pr=7$, it can be seen that the difference in the position for the green line for each set of figures is highest for $Pr=0.71$ followed by 3 and 7.

Bibliography

- [1] T. Cheng. Characteristics of mixed convection heat transfer in a lid-driven square cavity with various richardson and prandtl numbers. *International Journal of Thermal Sciences*, 50(2):197–205, 2011.
- [2] T. Chiang and T. W. H. Sheu. A numerical revisit of backward-facing step flow problem. *Physics of Fluids*, 11(4):862–874, 1999.
- [3] A. Cortes and J. Miller. Numerical experiments with the lid driven cavity flow problem. *Computers & Fluids*, 23(8):1005–1027, 1994.
- [4] I. Demirdžić, Ž. Lilek, and M. Perić. Fluid flow and heat transfer test problems for non-orthogonal grids: bench-mark solutions. *International Journal for Numerical Methods in Fluids*, 15(3):329–354, 1992.
- [5] E. D. dos Santos, A. P. P. an L. A. O. Rocha, and F. H. R. Franca. Numerical study of forced convection lid-driven cavity flows using LES (Large Eddy Simulation). *Journal of Energy and Power Engineering*, 7:1669–1680, 2013.
- [6] C. Fei. *Numerical Study on the Flow and Heat Transfer Characteristics between Liquid Lead Bismuth Eutectic and Helium*. PhD thesis, Beijing: University of Chinese Academy of Sciences, 2014.(in Chinese)(éé£ âŠ, 2014).
- [7] L. Fuchs and N. Tillmark. Numerical and experimental study of driven flow in a polar cavity. *International Journal for numerical Methods in Fluids*, 5(4):311–329, 1985.
- [8] U. Ghia, K. N. Ghia, and C. T. Shin. High-Re solutions for incompressible flow using the Navier-Stokes equations and a multigrid method. 48:387–411, 1982.

- [9] R. Iwatsu, J. M. Hyun, and K. Kuwahara. Mixed convection in a driven cavity with a stable vertical temperature gradient. *International Journal of Heat and Mass Transfer*, 36(6):1601–1608, 1993.
- [10] G. R. Kefayati. FDLBM simulation of magnetic field effect on non-Newtonian blood flow in a cavity driven by the motion of two facing lids. *Powder Technology*, 253:325 – 337, 2014.
- [11] X. Lei, Z. Guo, Y. Wang, and H. Li. Assessment and improvement on the applicability of turbulent-prandtl-number models in rans for liquid metals. *International Journal of Thermal Sciences*, 171:107260, 2022.
- [12] N. C. Markatos and K. Pericleous. Laminar and turbulent natural convection in an enclosed cavity. *International journal of heat and mass transfer*, 27(5):755–772, 1984.
- [13] V. Martin, A. Drochon, O. Fokapu, and J.-F. Gerbeau. MagnetoHemoDynamics in the aorta and electrocardiograms. *Physics in Medicine and Biology*, 57(10):3177–3195, may 2012.
- [14] M. Moallemi and K. Jang. Prandtl number effects on laminar mixed convection heat transfer in a lid-driven cavity. *International Journal of Heat and Mass Transfer*, 35(8):1881–1892, 1992.
- [15] N. Ouertatani, N. B. Cheikh, B. B. Beya, T. Lili, and A. Campo. Mixed convection in a double lid-driven cubic cavity. *International Journal of Thermal Sciences*, 48(7):1265–1272, 2009.
- [16] A. K. Prasad and J. R. Koseff. Reynolds number and end-wall effects on a lid-driven cavity flow. *Physics of Fluids A: Fluid Dynamics*, 1(2):208–218, 1989.
- [17] F. Selimefendigil and A. J. Chamkha. Magnetohydrodynamics mixed convection in a lid-driven cavity having a corrugated bottom wall and filled with a non-newtonian power-law fluid under the influence of an inclined magnetic field. *Journal of Thermal Science and Engineering Applications*, 8(2), 2016.
- [18] M. Taher, H. Kim, and Y. Lee. High prandtl number mixed convection cavity flow using lattice boltzmann method. *European Scientific Journal*, 9(33), 2013.
- [19] F. Talebi, A. H. Mahmoudi, and M. Shahi. Numerical study of mixed convection flows in a square lid-driven cavity utilizing nanofluid. *International Communications in Heat and Mass Transfer*, 37(1):79–90, 2010.

- [20] S. Thohura, M. M. Molla, M. A. Sarker, and M. C. Paul. Study of mixed convection flow of power-law fluids in a skewed lid-driven cavity. *Heat Transfer*, 2021.
- [21] D. C. Wan, B. S. V. Patnaik, and G. W. Wei. A new benchmark quality solution for the buoyancy-driven cavity by discrete singular convolution. *Numerical Heat Transfer, Part B: Fundamentals*, 40(3):199–228, 2001.